DISS. ETH NO. 24451

Time-lapse tomography of mass fluxes and microstructural changes in snow

A thesis submitted to attain the degree of

DOCTOR OF SCIENCES of ETH ZURICH

Dr. sc. ETH Zurich

presented by

MAREIKE WIESE

MSc., Universität Hamburg

born on 09.04.1986

citizen of Germany

accepted on the recommendation of

Prof. Dr. Dani Or
Dr. Martin Schneebeli
Prof. Dr. Florent Dominé

2017

Abstract

The structure and physical and mechanical properties of a snowpack are affected by the complex interplay of various mass fluxes. While the effect of mass fluxes at the microscale is difficult to measure in the field, such measurements are possible through time-lapse micro-computed tomography in the laboratory. A special device, the Snowbreeder, imposes a temperature gradient on a snow sample while this is scanned periodically to obtain 3D images of the evolving microstructure indicating the occurrence of mass fluxes. This thesis focuses on the effect of mass fluxes within the snowpack and across the ground-snow interface on the snow microstructure. Water-vapour fluxes in the snow are caused by vapour-concentration differences in the pore space induced by temperature and curvature differences. The resulting recrystallization process leads to snow metamorphism. Temperature differences at the ground-snow interface initiate an additional vapour flux between the ground and the snowpack. Simultaneously, settlement leads to snow densification.

Temperature conditions are complex in a snowpack, for example temperature gradients often change direction in surface snow. In a series of experiments the effect of such alternating temperature gradients on the structural snow evolution was investigated. In the Snowbreeder, samples of rounded snow were exposed to symmetrical and asymmetrical alternating temperature gradients with an amplitude of up to $100\,\mathrm{K\,m^{-1}}$ and periods of up to 72 h. The SSA remained nearly constant and a vertical anisotropy developed. The changing direction of the mass flux within the snow led to a structure consisting of a young shell and an old core, with more aging resulting from a symmetric than from an asymmetric alternating temperature gradient.

In a natural snowpack, snow metamorphism occurs simultaneously with settlement. With previously developed Snowbreeders, temperature-gradient metamorphism has been

investigated without taking settlement into account. To extend these previous measurements, a new Snowbreeder was developed, with which a unidirectional temperature gradient can be imposed on a snow sample and simultaneously settlement can be induced by placing a passive load on top of the sample. The weight of the load can be varied, simulating various snow heights on top of the snow sample. The temperature control on both ends of the sample was designed such that continuous micro-CT measurements are not restricted and the passive load on top of the snow sample can move freely. First experiments showed less settlement when a temperature gradient was applied to a snow sample compared to isothermal conditions.

With this new Snowbreeder past isothermal snow deformation experiments were complemented with experiments of settlement in the first days after onset of temperature-gradient metamorphism. Temperature gradients of up to 95 $\mathrm{K\,m^{-1}}$ were imposed on samples of rounded snow with a density of around 230 $\mathrm{kg\,m^{-3}}$. Settlement was simultaneously induced by applying a 1.7 kPa stress with the passive load of the Snowbreeder on the samples. Snow settled about half as fast when a temperature gradient was present, compared to isothermal conditions. The change in specific surface area after four days caused by temperature-gradient metamorphism was only a few percent. The viscosity evolution correlated with the amplitude of the temperature gradient. Finite element simulations of the stress distribution in the snow samples revealed that stress-bearing chains had developed in the snow structure, causing the large increase in viscosity. A small change in microstructure caused a large change in the mechanical properties.

Snow metamorphism has rarely been investigated at the snow-soil interface, even though the snowpack structure close to the ground strongly influences heat and mass fluxes across the interface, and Arctic wildlife. Few field observations report low-density snow layers close to the ground. In a third series of Snowbreeder experiments a temperature gradient of up to 100 $\mathrm{K\,m^{-1}}$ was imposed on a sample composed of rounded snow and a soil-analogue made of an ice-saturated layer of glass beads. After four days a 2 to 3 mm layer of low-density snow formed above the soil. Simultaneously, the soil dried due to a constant vapour flux from the soil to the snow. A very similar snow-density decrease occurred also at the interface of an ice lens and snow. This showed that the primary reason for the density decrease was a smaller available surface area for sublimation than for deposition. The drying of the soil had probably an additional small contribution to the density decrease in the snow above the soil. Temperature simulations show the development of a strong temperature gradient above the ice lens towards the end of the experiment due to the formation of the low-density snow layer.

Zusammenfassung

Die Struktur und die physikalischen und mechanischen Eigenschaften einer Schneedecke werden durch das komplexe Zusammenspiel verschiedener Massenflüsse beeinflusst. Während der Effekt von mikroskaligen Massenflüssen im Feld kaum messbar ist, ermöglichen Zeitrafferaufnahmen mit Mikro-Computertomografie solche Messungen im Labor. In einem speziellen Gerät, dem Snowbreeder, wird eine Schneeprobe einem Temperaturgradienten ausgesetzt, während diese gescannt wird, um 3D-Bilder der sich entwickelnden Mikrostruktur zu erhalten, die auf das Auftreten von Massenflüssen hinweist. Der Schwerpunkt dieser Arbeit liegt auf dem Einfluss von Massenflüssen innerhalb der Schneedecke und an der Boden-Schnee-Grenzfläche auf die Schneemikrostruktur. Durch Temperatur- und Krümmungsunterschiede entstehen Dampfkonzentrationsunterschiede im Porenraum des Schnees, die zu Wasserdampfflüssen im Schnee führen. Der daraus resultierende Rekristallisationsprozess führt zur Schneemetamorphose. Durch Temperaturunterschiede an der Boden-Schnee-Grenzfläche entsteht ein zusätzlicher Dampffluss zwischen dem Boden und der Schneedecke. Gleichzeitig führt die Setzung zur Schneeverdichtung.

Die Temperaturbedingungen in einer Schneedecke sind komplex, zum Beispiel wechseln Temperaturgradienten häufig im oberen Bereich einer Schneedecke ihre Richtung. In einer Reihe von Experimenten wurde die Wirkung solcher wechselnder Temperaturgradienten auf die Entwicklung der Schneestruktur untersucht. Im Snowbreeder wurden Proben von rundem Schnee symmetrisch und asymmetrisch wechselnden Temperaturgradienten mit einer Amplitude von bis zu $100\,\mathrm{K\,m^{-1}}$ und Perioden von bis zu 72 h ausgesetzt. Die SSA blieb nahezu konstant und der Schnee wurde vertikal anisotrop. Die wechselnde Richtung des Massenflusses im Schnee führte zu einer Struktur, die aus einer jungen Hülle und einem alten Kern bestand, wobei der Schnee unter dem Ein-

fluss eines symmetrisch wechselnden Temperaturgradienten älter wurde als unter einem asymmetrisch wechselnden Temperaturgradienten.

In der Natur treten Schneemetamorphose und Setzung gleichzeitig auf. Mit zuvor entwickelten Snowbreedern wurde bis jetzt die Schneemetamorphose unter dem Einfluss eines Temperaturgradienten ohne Berücksichtigung der Setzung untersucht. Um diese bisherigen Messungen zu erweitern, wurde ein neuer Snowbreeder entwickelt, in dem eine Schneeprobe einem konstanten Temperaturgradienten ausgesetzt werden kann und gleichzeitig Setzung durch ein passives Gewicht auf der Probe ausgelöst werden kann. Das Gewicht der Last kann variiert werden, um verschiedene Schneehöhen über der Schneeprobe zu simulieren. Die Temperaturregelung an beiden Enden der Probe wurde so konstruiert, dass eine ungehinderte Bewegung des Snowbreeders während der Mikro-CT-Messungen und eine ungehinderte Bewegung des Gewichts auf der Schneeprobe gewährleistet ist. Erste Experimente zeigten eine geringere Schneesetzung unter dem Einfluss eines Temperaturgradienten im Vergleich zu isothermen Bedingungen.

Mit diesem neuen Snowbreeder wurden frühere isotherme Schneedeformationsexperimente mit Setzungsexperimenten während der ersten Tage nach Beginn der Temperaturgradientmetamorphose ergänzt. Proben von rundem Schnee mit einer Dichte von $230\,\mathrm{kg\,m^{-3}}$ wurden Temperaturgradienten von bis zu $95\,\mathrm{K\,m^{-1}}$ ausgesetzt. Gleichzeitig führte das passive Gewicht auf der Schneeprobe durch einen Druck von 1.7 kPa zur Setzung. Der Schnee setzte sich halb so schnell unter dem Einfluss eines Temperaturgradienten im Vergleich zu isothermen Bedingungen. Innerhalb von vier Tagen änderte sich die spezifische Oberfläche durch Temperaturgradientmetamorphose nur um ein paar Prozent. Die Entwicklung der Viskosität korrelierte mit der Amplitude des Temperaturgradienten. Finite-Elemente-Simulationen der Druckverteilung in den Schneeproben zeigten, dass sich tragende Strukturen innerhalb der Schneestruktur gebildet hatten, die zu einer starken Zunahme der Viskosität führten. Eine kleine Änderung der Mikrostruktur führte zu einer großen Änderung der mechanischen Schneeeigenschaften.

Schneemetamorphose wurde bis jetzt kaum an der Schnee-Boden-Grenzfläche untersucht, obwohl die Struktur der Schneedecke am Boden Wärme- und Massenflüsse zwischen Schnee und Boden und das Leben arktischer Tiere stark beeinflusst. Im Feld wurden manchmal Schneeschichten mit niedriger Dichte nahe am Boden beobachtet. In einer dritten Reihe von Snowbreeder-Experimenten wurde eine Probe aus rundem Schnee auf einem nachgebildeten Boden bestehend aus einer eisgesättigten Schicht aus Glassperlem einem Temperaturgradienten von bis zu $100\,\mathrm{K\,m^{-1}}$ ausgesetzt. Nach vier Tagen bildete sich über dem Boden eine 2 bis 3 mm hohe Schneeschicht mit niedriger

Dichte. Gleichzeitig nahm der Eisgehalt des Bodens durch den kostanten Dampffluss vom Boden in die Schneedecke ab. Auch über einer Eislinse nahm die Schneedichte ähnlich wie über dem Boden ab. Dies zeigt, dass der Hauptgrund für die Dichteabnahme die im Vergleich zur Resublimationsoberfläche kleinere Sublimationsoberfläche ist. Die Abnahme des Eisgehalts des Bodens trug zusätzlich etwas zur Dichteabnahme im Schnee über dem Boden bei. Temperatursimulationen zeigen die Entwicklung eines starken Temperaturgradienten oberhalb der Eislinse gegen Ende des Experiments aufgrund der Dichteabnahme im Schnee.

Contents

List of Figures

List of Tables

Chapter 1

Introduction

1.1 Snow: an active material

As the largest part of the cryosphere, snow covers large parts of the Earth's surface and thereby snow strongly affects the climate and life on Earth. On average, 46 Mio km^2 of the Earth's surface are snow-covered each year, which makes up 9% of the Earth's surface [National Snow and Ice Data Center, 2017]. The snow-cover extent shows high variability between years, seasons and the hemispheres. For example, around 98% of the snow cover lies on the Northern Hemisphere and the largest snow-cover extent is reached during winter on the Northern Hemisphere (Fig. 1.1). The snow cover is distinguished between a seasonal snow cover, i.e. present only during winter, like in the Alps, and a perennial snow cover, i.e. persisting over the whole year, like in most of Antarctica and the Greenland ice sheet.

Snow affects the Earth's energy balance by its high albedo and low heat conductivity [Domine et al., 2007a, and references therein]. Due to the high albedo of around 0.9 in the visible range most of the incoming solar radiation is reflected by snow. This feature leads to the well-known snow-albedo-feedback, which enhances for example the warming of the Arctic due to a decrease in surface albedo as snow-free surfaces increase. Due

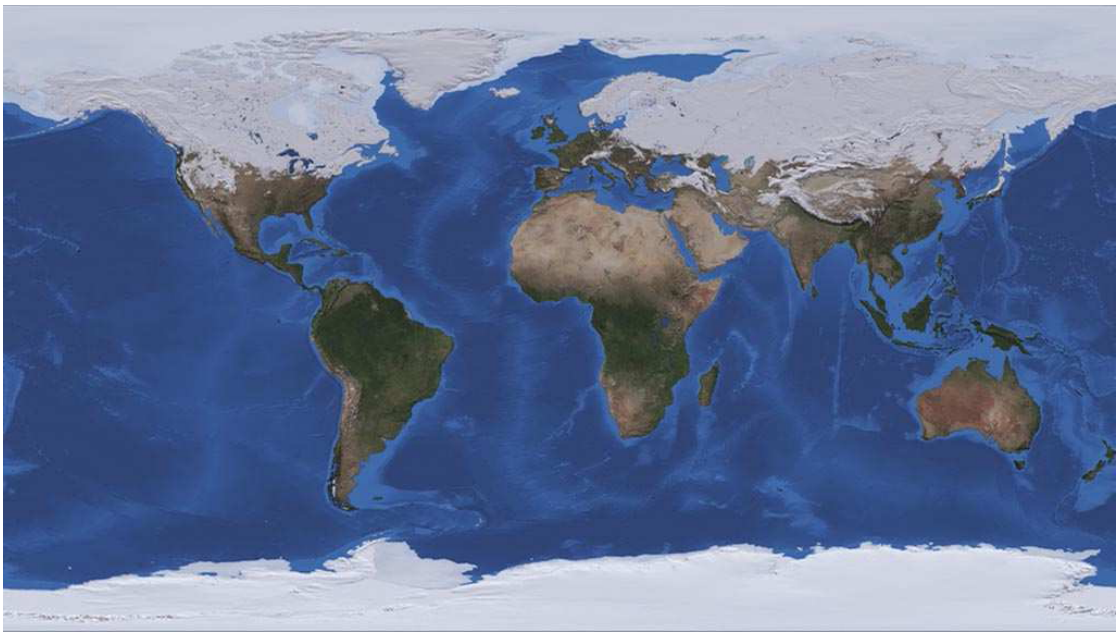

Figure 1.1: *Snow cover during winter on the Northern Hemisphere (From: http://svs.gsfc.nasa.gov/10850).*

to its low heat conductivity snow insulates the ground below from low air temperatures, which affects also other components of the cryosphere, such as permafrost, glaciers and sea ice.

Snow has also a strong impact on life on Earth [Callaghan et al., 2011, and references therein], both positively and negatively. Snow is an important water reservoir. Additionally, people spend their winter holidays frequently in snow-covered areas, such as the Alps, for doing winter sports. However, snow in the form of an avalanche also poses a natural hazard. Avalanches can kill people and cause damage in buildings, roads and train tracks. The insulating effect of snow protects plants and animals below the snow cover from very low temperatures. The structure of a snowpack determines food availability for Arctic animals, such as reindeers, lemmings and their predators [Berteaux et al., 2016].

Snow is not just a white blanket covering the Earth's surface, but it has a complex interior, which evolves continuously. A snowpack is a porous medium consisting of an ice matrix with an air-filled pore space. A closer look into this porous medium reveals a composition of many different layers (Fig. 1.2), which form due to different consecutive snow falls and changing environmental conditions affecting the snowpack. Each layer has a different microstructure, e.g. a different density, different snow-grain shape and

size (Fig. 1.3), and different connectivity between grains. This microstructure changes continuously due to snow metamorphism. Sublimation of the ice structure supplies the pore space of the snowpack with water vapour, which is transported by diffusion within the pore space and condenses again on the ice structure. This process occurs due to the high equilibrium vapour pressure and the high homologous temperature of ice. The homologous temperature, defined as the ratio of the temperature T of a material to its melting temperature T_m, has a value of $T/Tm \geq 0.9$ for ice at temperatures down to -30°C. Hence, snow on Earth is a high-temperature material.

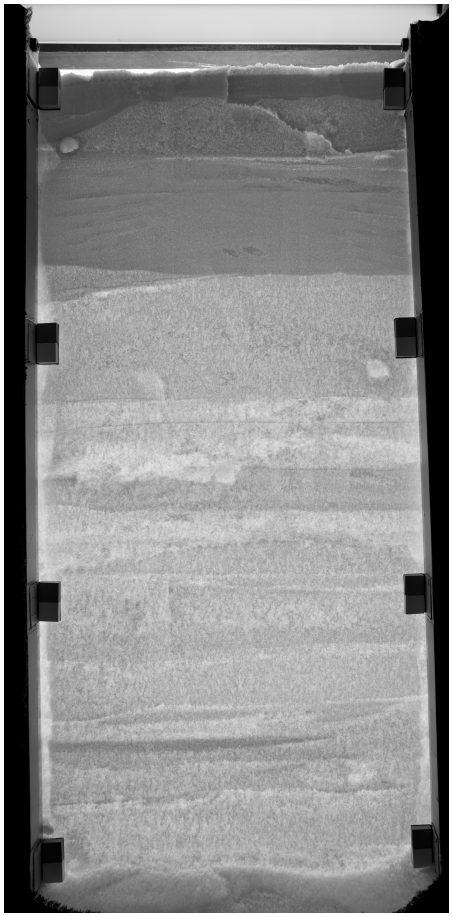

Figure 1.2: *Transmitted-light picture of a snowpack showing several different layers at Point Barnola in Antarctica (From: Martin Schneebeli). The size of the image is 110 x 55 cm^2.*

In addition to vapour diffusion, various other mass fluxes within the snowpack and at the atmosphere-snow and ground-snow interface influence the snowpack structure (Fig. 1.4). Water vapour can also be transported by convection due to vertical temperature differences within the snowpack [Sturm and Johnson, 1991]. Additionally, settlement

occurs due to the overburden pressure imposed by the snow's own weight. Eventually, infiltrating rain and melt water can refreeze and form ice lenses within the snowpack [Fierz et al., 2009]. Simultaneous to the internal mass fluxes, water in all aggregation states can enter or leave the snowpack across the interfaces. The weather greatly influences the atmosphere-snow mass fluxes by variations in temperature, humidity, precipitation and wind. Water vapour from the atmosphere enters the snowpack through the pore space by diffusion or wind pumping [Colbeck, 1989a], or condenses on the snowpack surface forming surface hoar [Fierz et al., 2009]. Snow accumulates on the snowpack surface by further snow falls and at higher temperatures water enters the snowpack as rain. Conversely, water vapour leaves the snowpack into the atmosphere due to sublimation under low relative humidity. Additionally, wind redistributes snow by different types of aeolian snow transport, i.e. creep, saltation and suspension [Nemoto and Nishimura, 2004], leading to snow erosion, snow accumulation and snow-dune formation at the snowpack surface [Birnbaum et al., 1998]. The ground below a snowpack can consist of various soil types, glacier ice or sea ice. Water vapour diffuses from the ground into the snowpack or vice versa [Domine et al., 2016]. Snow-melt water runs off at the ground surface or infiltrates the soil and sea ice, possibly refreezing and forming freshwater-ice lenses. On sea ice brine can enter the snowpack by brine expulsion from the sea ice [Sturm and Massom, 2009]. Additionally, a thick snow cover can push the sea ice into the ocean water, causing flooding of the snowpack.

The complex interplay of all these mass fluxes influences the structure of a snowpack. The macroscopic physical properties of snow, such as the albedo and heat conductivity, depend again on the complex snow microstructure [Domine et al., 2007a]. Since the microstructure varies both spatially and temporally, also the physical snow properties vary [Calonne et al., 2014; Domine et al., 2007a]. Therefore, a good knowledge of the snow microstructure, snow metamorphism and mass fluxes influencing the snowpack is necessary to understand their influence on the physical snow properties in detail and to understand the effect of snow on the Earth's climate and on life on Earth. The observa-

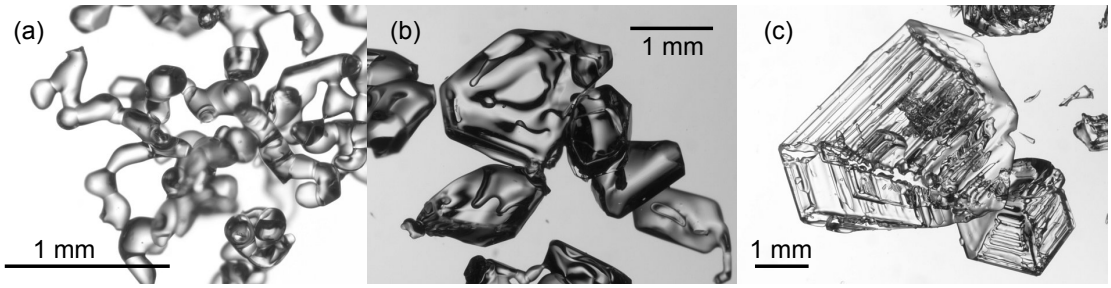

Figure 1.3: *Isothermal rounded snow grains (a), and faceted snow grains (b) and cup crystals (c) caused by temperature-gradient metamorphism (From: archive SLF).*

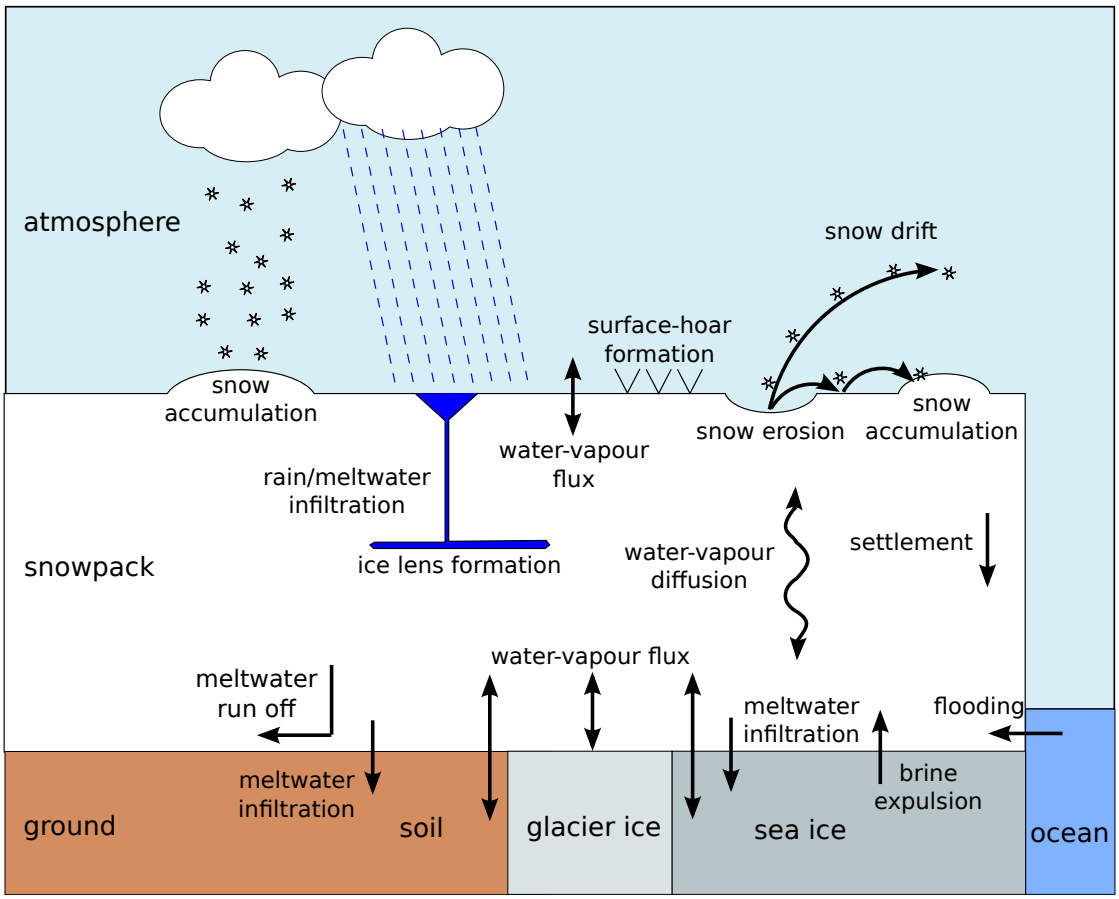

Figure 1.4: *Sketch of mass fluxes at the snow-atmosphere and snow-ground interface, and within a snowpack.*

tion and measurement of the full snow microstructure and mass fluxes at the microscale is difficult in the field. A tool, which makes such measurements possible in the laboratory is time-lapse micro-computed tomography, which is presented in the following section.

1.2 Time-lapse micro-computed tomography

In field measurements the snowpack structure is often investigated with a traditional snow profile. Such a profile is only a snapshot of the actual state of the snowpack. Additionally, only single snow grains broken out of the sintered snow structure are observed [Fierz et al., 2009] (Fig. 1.3), i.e. snow is considered as a granular material. A

first step to investigate the full snow microstructure, i.e. including the bonds between single grains, was serial sectioning of casted snow samples [Schneebeli, 2000]. With this technique 3D images of the microstructure could be created, which could be analysed with stereology [Good, 1987]. This technique is very time consuming, which is disadvantageous.

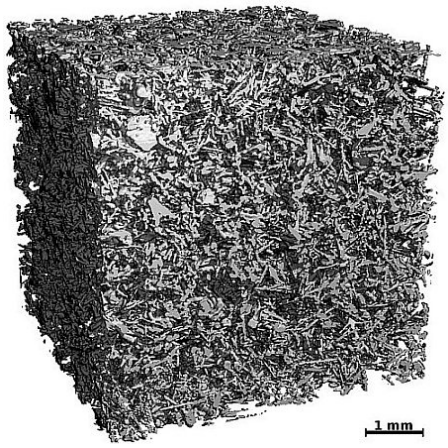

Figure 1.5: *Micro-computed tomography image of the microstructure of new snow (From: http://www.slf.ch/ueber/organisation/schnee_permafrost/schneephysik/Bildergalerie/index_EN).*

Since more than one decade micro-computed tomography (micro-CT) measurements allow to measure the full snow microstructure non-destructively and faster than with serial sectioning [Brzoska et al., 1999; Coléou et al., 2001]. With this technique snow samples with a diameter of a few centimetres are scanned with X-rays to obtain 3D images of the snow microstructure with a resolution in the micrometer scale (Fig. 1.5). This can be done either at synchrotron beam lines or with desktop devices. While synchrotrons provide very high-resolution measurements with short scanning times, desktop devices enable measurements at stable temperature conditions in cold rooms. From the 3D images microstructural parameters and physical and mechanical properties of snow samples can be calculated [Brzoska et al., 2001; Schneebeli, 2004]. The three most important microstructural snow properties are density, specific surface area SSA and anisotropy. The SSA is defined as the ratio of the ice surface area to the ice mass, and the anisotropy is defined as the ratio of the mean vertical snow-structure size to the mean horizontal snow-structure size. The density and SSA for example influence the climate-relevant properties heat conductivity and albedo such that the heat conductivity of snow increases with density [Calonne et al., 2011] and the albedo increases with SSA [Flanner and Zender, 2006]. Micro-CT measurements show that the snow microstructure is often anisotropic, which causes also an anisotropy in the physical and mechanical snow properties [Calonne et al., 2014, 2011; Riche and Schneebeli, 2013].

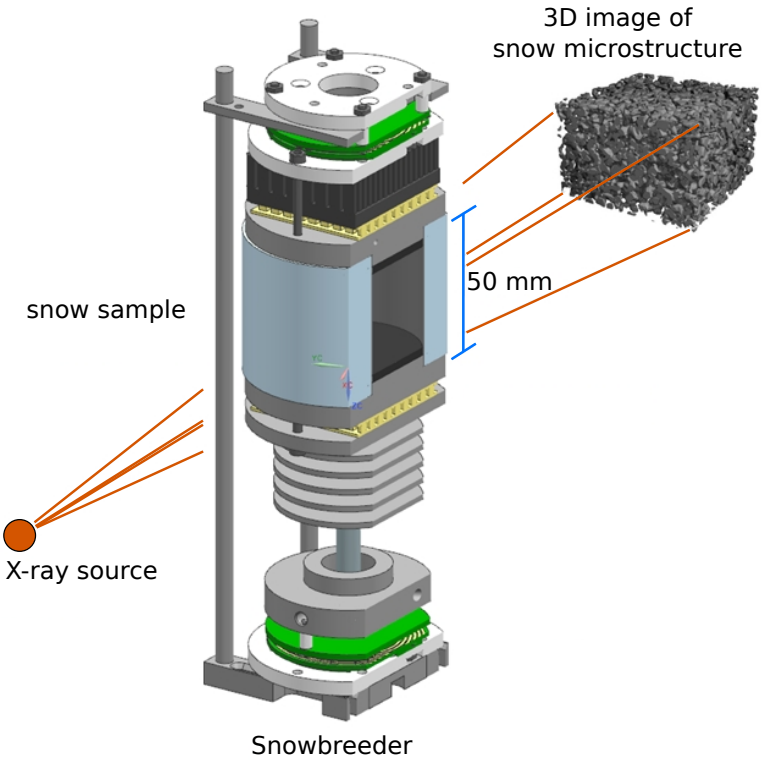

Figure 1.6: *Sketch of time-lapse micro-CT measurements with a Snowbreeder (From: http://www.slf.ch/ueber/organisation/schnee_permafrost/schneephysik/hinter_kulissen/index_EN).*

In addition to measuring the microstructure of single snow samples, the microstructural evolution of snow can be observed with time-lapse micro-CT measurements [Calonne et al., 2014; Kaempfer and Schneebeli, 2007; Pinzer et al., 2012; Schneebeli and Sokratov, 2004]. During these measurements several subsequent images are taken from one sample, as it evolves with time. Such measurements are possible only with desktop computer tomographs, because of the long duration of up to several months of such experiments. A special sample holder, the so-called Snowbreeder, was developed for time-lapse micro-CT experiments [Ebner et al., 2014; Pinzer and Schneebeli, 2009a; Schneebeli and Sokratov, 2004]. With such a Snowbreeder a temperature gradient, unidirectional or alternating, can be imposed on a snow sample, while the snow sample is scanned periodically to obtain the 3D images (Fig. 1.6). With this technique Pinzer et al. [2012] could for example show that individual snow grains do not change their shape, but a complete relocation of the ice mass occurs within days. Consequently, the age of single grains is only a few days. Calonne et al. [2014] and Riche and Schneebeli [2013] found that the anisotropy evolves during temperature-gradient metamor-

phism such that also the physical snow properties evolve an anisotropy during snow metamorphism. Such informations cannot be retrieved from single snow-grain observations.

1.3 Processes investigated in this thesis

This thesis focuses on internal mass fluxes within a snowpack, i.e. settlement and vapour diffusion with the accompanying snow metamorphism.

1.3.1 Mass fluxes in snow metamorphism

Snow metamorphism is a recrystallization process. Differences in the equilibrium water-vapour pressure above ice surfaces with different curvature and temperature lead to differences in water-vapour concentration in the pore space of the snow. This causes vapour diffusion within the pore space, which again leads to deviations of the local vapour pressure from the equilibrium vapour pressure, causing sublimation of ice and deposition of water vapour. Traditionally, dry snow metamorphism is divided into isothermal and temperature-gradient metamorphism, in which curvature and temperature differences drive the vapour diffusion, respectively (Fig. 1.7). The equilibrium vapour pressure is higher above convex, small or warm ice surfaces than above concave, large or cold ice surfaces. However, temperature and curvature differences in the snow structure affect snow metamorphism simultaneously. Depending on the snow type, i.e. curvature, and the strength of the temperature gradient, one effect can prevail.

Temperature conditions are complex in a snowpack. Most often there is rather a temperature gradient in a snowpack than pure isothermal conditions. Temperature gradients occurring in a snowpack do not necessarily have to be unidirectional. For example, close to the surface of a seasonal snowpack, the diurnal cycle of the solar insolation can cause alternating temperature gradients with a diurnal period (Fig. 1.8) [Birkeland et al., 1998; Fierz, 1998, 2011]. A temperature gradient across the snow-ground interface can lead to an additional vapour flux into the snowpack (Fig. 1.4), which contributes to the metamorphism occurring in the snowpack.

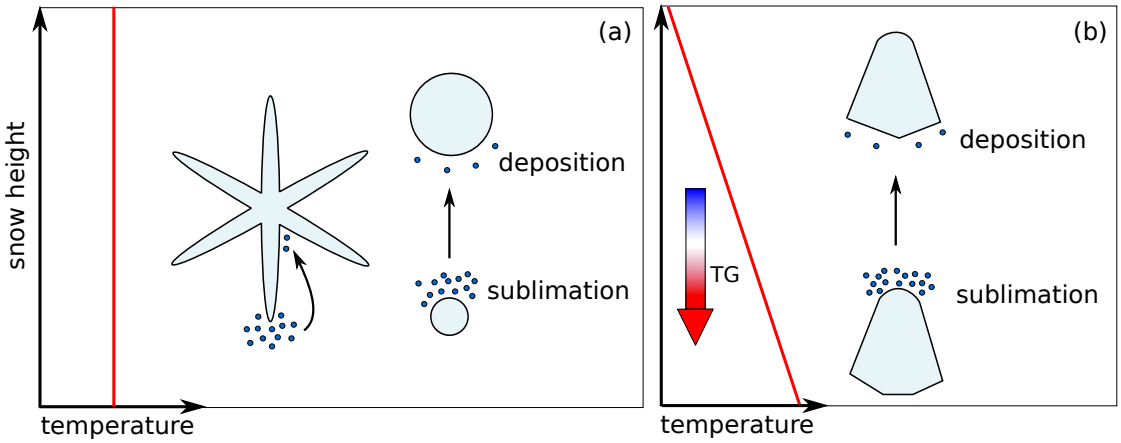

Figure 1.7: *Sketch of isothermal (a) and unidirectional temperature-gradient metamorphism (b) in a snowpack. The red lines indicate two different temperature profiles in the snowpack (TG = temperature gradient). The small dark blue circles represent water-vapour molecules and their amount indicates the equilibrium water-vapour pressure above snow grains (light blue shapes) according to their curvature (a) and temperature (b). The black arrows show the water-vapour flux according to the differences in water-vapour concentration above the different snow grains.*

1.3.2 Snow settlement as a mass flux

Snow settlement is the slow plastic compression of a snowpack due to the overburden pressure resulting from its own weight under the influence of gravity. This causes densification and a decrease in snowpack height (Fig. 1.9). Thus, settlement can be considered as another type of mass displacement. During this compression, processes at the microscale occur. Theile et al. [2011] found that not grain rearrangements, i.e. intercrystalline deformation, but intracrystalline deformation occurs during settlement. The settlement velocity decreases with decreasing temperature and increasing density. Snow settlement influences processes such as avalanche formation [Schweizer et al., 2003] and firn formation on ice sheets [Fujita et al., 2016].

1.3.3 Outline of the thesis

For this thesis mass fluxes in snow metamorphism under conditions representative for three different parts of the snowpack (Fig. 1.9) were analysed with time-lapse micro-CT measurements. The goal of this thesis was gaining a better understanding of how unidirectional and alternating temperature gradients affect structural and mechanical

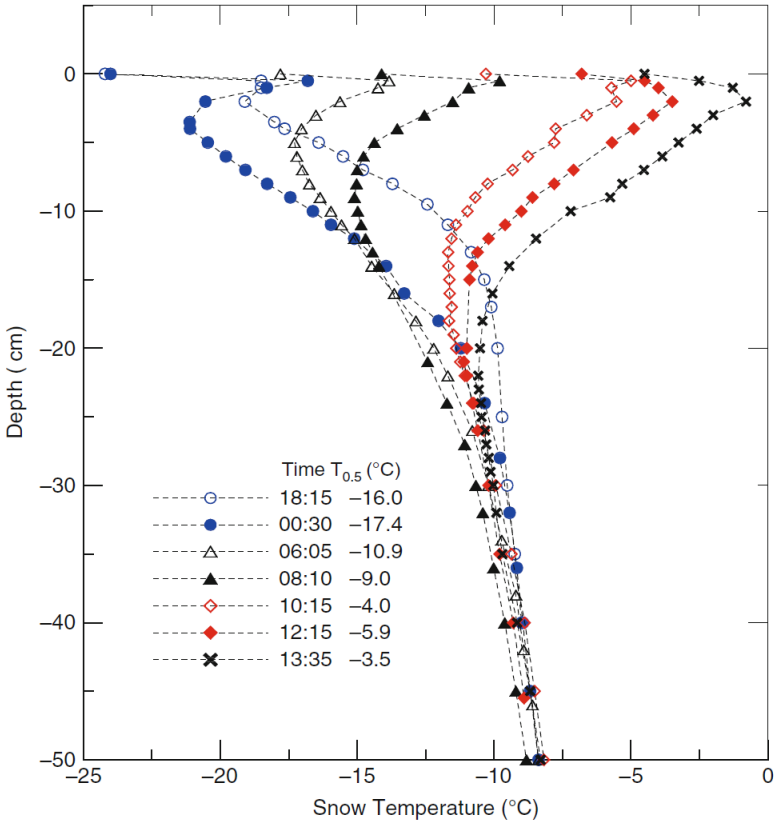

Figure 1.8: *Snow temperature profiles measured 23–24 February 2000, on the study plot of the WSL Institute for Snow and Avalanche Research SLF, Weissfluhjoch, 2540 ma.s.l., Davos, Switzerland. The temperature probe was inserted vertically down from the surface (From: Fierz [2011]).*

properties of snow. The chapters of this thesis consist of papers, as listed in detail on page 119.

Starting in surface snow, the effect of sign-alternating temperature gradients on the microstructural snow evolution was analysed. Such alternating gradients were regularly observed [Birkeland, 1998; Birkeland et al., 1998; Fierz, 1998, 2011; Weller and Schwerdtfeger, 1977] and thought to form faceted snow in a seasonal snowpack [Birkeland et al., 1998]. However, in laboratory experiments Pinzer and Schneebeli [2009b] showed that symmetrical diurnal sign-alternating temperature gradients formed rounded snow. Their study was so far the only one in which alternating temperature gradient metamorphism was investigated in detail. The measurements presented in Chapter 2 of this thesis complement the study of Pinzer and Schneebeli [2009b] to gain further insights into the microstructural snow evolution under the influence of alternating temperature

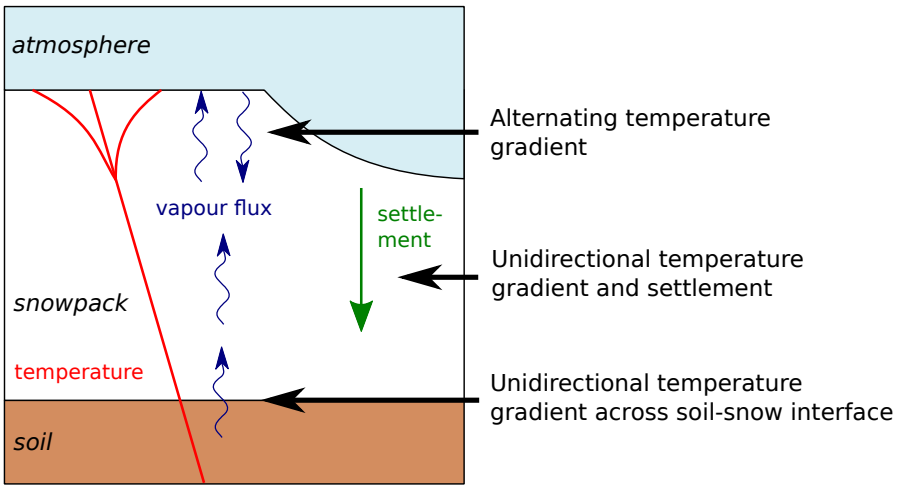

Figure 1.9: *Sketch of the different conditions under which snow metamorphism was investigated experimentally for this thesis.*

gradients. Experiments with symmetric and asymmetric alternating temperature gradients with other periods than a 24 h period were conducted. The focus was particularly on the evolution of the snow age, the specific surface area, the anisotropy and the mass turnover. The results shed new light on how the anisotropy of the snow microstructure influences the mass turnover.

For the second series of experiments a new Snowbreeder was developed, the Snowbreeder 5. This Snowbreeder was designed for investigations of snow metamorphism together with settlement. In the previous Snowbreeders only temperature-gradient metamorphism, either unidirectional or alternating, could be investigated [Pinzer and Schneebeli, 2009a; Schneebeli and Sokratov, 2004]. With the new Snowbreeder settlement can be induced with a passive load on top of a snow sample in addition to imposing a unidirectional temperature gradient. This Snowbreeder is presented in Chapter 3.

Below the surface snow settlement due to the weight of overlying snow becomes increasingly pronounced. In this part of the snowpack the temperature conditions are either isothermal or unidirectional temperature gradients occur, leading to snow metamorphism simultaneous to settlement. Field observations show that settlement differs greatly between different snow types formed under different temperature conditions, even though the density was similar, e.g. rounded well-sintered snow was observed to settle faster than depth hoar [Armstrong, 1980; Kojima, 1967; Shapiro et al., 1997; Sturm and Benson, 1997; Sturm and Holmgren, 1998]. However, detailed laboratory investigations of snow settlement were so far only done under isothermal conditions

[Scapozza and Bartelt, 2003a,b; Schleef and Löwe, 2013; Schleef et al., 2014b,c; Theile et al., 2011], even though often temperature gradients exist in a snowpack. Therefore, a series of settlement experiments under temperature-gradient conditions was conducted with the Snowbreeder 5, as presented in Chapter 4, to extend the previous isothermal experiments. The goal was to gain a better understanding of the influence of the snow microstructure and snow metamorphism on settlement.

Temperature gradients occur not only within the snowpack, but also across the interfaces of the snowpack, leading to snow metamorphism and thus influencing the snowpack structure. So far, snow metamorphism at the soil-snow interface was barely investigated. In few field observations low-density snow and even gaps in the snowpack were found close to the ground [Bader et al., 1939; Domine et al., 2016]. Domine et al. [2016] hypothesized that the low-density layer formed due to a strong upward vapour flux from the soil due to strong temperature gradients across the soil-snow interface. This hypothesis was further investigated in a third series of laboratory experiments in this thesis, as presented in Chapter 5. The aim was to analyse how a strong unidirectional temperature gradient affects the snowpack close to the soil-snow interface.

Chapter 2

Structural evolution and mass fluxes of snow under controlled alternating temperature gradients with a periodicity between one and three days

Abstract

Temperature gradients often change direction in surface snow. This condition has been observed for a very long time, but its importance was not realized. In laboratory experiments we investigated the structural change of rounded snow caused by alternating temperature gradients by means of time-lapse micro-computed tomography. We imposed symmetric sinusoidal temperature gradients with an amplitude of up to 100 K m^{-1} and periods of 24, 48 and 72 h on snow samples. The age of the snow structure shows that the changing direction of the mass flux within the snow led to a structure consisting of a young shell and an old core, for the longest period this core was up to three weeks old. The SSA remained nearly constant due to the alternating direction of the mass flux and a vertical anisotropy developed. We also applied an asymmetric alternating temperature

gradient, which resulted in less ageing, while the SSA stayed also nearly constant and the snow structure became also anisotropic. We conclude that the effect of an inversion of the temperature gradient is a necessary extension to current snowpack models, especially concerning the SSA evolution, but also with respect to understanding the diffusion and redistribution of snow isotopes and impurities.

2.1 Introduction

Snow is a porous material that changes its microstructure by densification and metamorphism. The microstructural change caused by dry snow metamorphism occurs through water vapor transport within the snow. Snow metamorphism is a process occurring within seconds to days due to the very high homologous temperature of snow and high water vapor pressure. Traditionally, dry snow metamorphism is divided into isothermal metamorphism and temperature-gradient metamorphism. Isothermal metamorphism is driven by curvature differences on the snow grains, which cause the formation of mostly rounded snow grains. Temperature-gradient metamorphism is driven by temperature differences within the snowpack. The resulting water vapor diffusion leads to the growth of faceted grains and depth hoar (Pinzer et al. [2012], Calonne et al. [2014]). Observations show that the pore space gets larger and the snow microstructure gets coarser both during isothermal and temperature-gradient metamorphism (Pinzer et al. [2012], Kaempfer and Schneebeli [2007]).

Temperature gradients prevail in both the seasonal and the perennial polar snowpack. Alternating temperature gradients, i.e. temperature gradients with a temporally changing sign as defined by Pinzer and Schneebeli [2009a] and Pinzer and Schneebeli [2009b], occur close to the surface in seasonal snowpacks (i.e. in the upper centimeters to decimeters) (Fierz [2011], Fierz [1998], Birkeland et al. [1998]) and occur regularly in the upper meters in the perennial polar snowpack [Weller and Schwerdtfeger, 1977]. Alternating temperature gradients occur in the seasonal snowpack for example due to the diurnal cycle of the solar insolation [Birkeland, 1998] and in the perennial snowpack due to the seasonal temperature variations. In a perennial snowpack, for example in Antarctica, snow metamorphism due to alternating temperature gradients is the main metamorphic process. Isothermal conditions and unidirectional temperature gradients can be found deeper in the snowpack below the characteristic depth of alternating temperature-gradient occurrence defined by weather phenomena such as the diurnal cycle of solar insolation.

Birkeland [1998] proposed that possibly non-symmetric alternating temperature gra-

dients are one of the predominant reasons for the formation of near-surface faceted crystals within a few days in the field, whereas Pinzer and Schneebeli [2009b] found the formation of rounded grains with symmetric temperature gradients in the laboratory. Probably, in a natural snow cover density gradients also favor the growth of near-surface faceted crystals due to the associated differences in heat conductivity. Pinzer and Schneebeli [2009b] investigated the influence of alternating temperature gradients on the snow microstructure in laboratory experiments. In these experiments, a snow sample was exposed to a symmetrical sinusoidal temperature gradient with an amplitude of maximum $100\,\mathrm{K\,m^{-1}}$ and a period of 24 h, corresponding to the diurnal cycle of the solar insolation. Despite the large amplitude of the imposed temperature gradient, no facets or depth hoar formed in both directions of the temperature gradient. Pinzer and Schneebeli [2009b] concluded that the temporal stability of the vapor diffusion field is important for the facet formation. Similarly, Yosida [1955] discussed that the inversion of the heat flow leads to a rounded snow structure similar to isothermal conditions. Hence, Pinzer and Schneebeli [2009b] suggested that dry snow metamorphism should not only be divided into isothermal metamorphism and temperature-gradient metamorphism, but also alternating temperature-gradient metamorphism should be taken into account as a third characteristic process of dry snow metamorphism.

Although alternating temperature gradients in snowpacks have already been reported in the literature (Fierz [2011], Fierz [1998], Birkeland et al. [1998], Weller and Schwerdtfeger [1977]), little is known about the resulting snow microstructure, besides the study of Pinzer and Schneebeli [2009b]. Their study is so far the only one in which alternating temperature gradient metamorphism was investigated in detail. Pinzer and Schneebeli [2009b] did only three experiments, in which no other periods than the diurnal cycle were considered. According to the little information on the snow evolution under alternating temperature gradients, parameterizations for microstructural snow parameters for this type of snow metamorphism are not included in current snowpack models, such as SNOWPACK [Wever et al., 2015] and Crocus [Vionnet et al., 2012]. These models are parameterized for isothermal and unidirectional temperature-gradient snow metamorphism.

With this study, we extended the study of Pinzer and Schneebeli [2009b] to gain better insights into the microstructural evolution of snow under the influence of alternating temperature gradients. We conducted time-lapse micro-computed tomography experiments in a cold laboratory. In these experiments we imposed sinusoidal temperature gradients with different periods on snow samples. We focus particularly on the evolution of the specific surface area, the anisotropy and the mass turnover. The results shed new light on the effect of a sign-alternating temperature gradient and on how anisotropy influences the mass turnover.

2.2 Theory

The depth to which a snowpack is influenced by alternating temperature gradients can be calculated from the heat diffusion equation for a homogeneous dry snow pack with constant density ρ_s and constant thermal conductivity k_s, as described in Carslaw and Jaeger [1959]:

$$\rho_s c_{p,s} \frac{\partial}{\partial t} T = k_s \frac{d^2}{dz^2} T \tag{2.1}$$

$c_{p,s}$ is the specific heat of snow and T corresponds to the snow temperature. Equation 2.1 comprises the temperature variations in the snowpack due to heat diffusion in the snow, but not the internal heating of the snowpack caused by penetrating solar radiation. The snow temperature changes due to alternating atmospheric temperatures, which are included as an oscillating thermal boundary condition at the snow surface $z = 0$, while the snow temperature at the bottom $z = H$ stays constant at T_H:

$$T(H, t) = T_H \tag{2.2}$$

$$T(0, t) = \overline{T_0} + \delta T \sin(\omega t) \tag{2.3}$$

H is the snow depth and $\overline{T_0}$ is the mean snow surface temperature, which has fluctuations with a frequency ω and an amplitude δT. The temperature gradient within the snowpack can be separated into a mean linear temperature gradient $\overline{T_0} + \frac{z}{H}(T_H - \overline{T_0})$ and fluctuations $\tilde{T}(z, t)$:

$$T(z, t) = \overline{T_0} + \frac{z}{H}(T_H - \overline{T_0}) + \tilde{T}(z, t) \tag{2.4}$$

A simplified solution for depth and temporal dependence of the snow temperature can be found by assuming a deep snowpack with large H and approximating the temperature fluctuations $\tilde{T}(z, t)$ with the solution for a semi-infinite snowpack [Carslaw and Jaeger, 1959]:

$$T(z, t) = \overline{T_0} + \frac{z}{H}(T_H - \overline{T_0}) + \delta T \exp(-z/\xi) \sin(\omega t - z/\xi) \tag{2.5}$$

$\kappa_s = k_s/\rho_s c_{p,s}$ corresponds to the thermal diffusivity, which has values between $5 \cdot 10^{-8}\,\mathrm{m^2\,s^{-1}}$ and $5 \cdot 10^{-7}\,\mathrm{m^2\,s^{-1}}$ for snow. $\xi = \sqrt{2\kappa_s/\omega}$ is the characteristic length scale, from which the depth to which an alternating temperature signal penetrates into the snowpack can be calculated. For example, for diurnal temperature variations the frequency is $\omega = 24\,\mathrm{h^{-1}}$, which gives values for ξ between 0.09 m and 0.29 m. Thus, diurnal temperature variations penetrate into the first tens of centimeters of a snowpack. For temperature variations according to the annual temperature variations, for example in a polar snowpack, the frequency is $\omega = 1\,\mathrm{a^{-1}}$, which results in values for ξ between 1.78 m and 5.62 m. Equation 2.5 shows that temperature fluctuations are exponentially damped

and delayed with depth, as also observed by Fierz [2011]. The damping of the temperature signal is stronger for higher frequencies. This is also visible in the comparison of the penetration depths of diurnal and annual temperature variations, which are in the order of centimeters and meters, respectively. The temperature distribution and fluctuations in a snowpack get more complex when internal heating of the snowpack occurs close to the surface due to penetrating solar radiation. This additional heating affects the shape of the temperature gradient, as the evolution of the temperature gradient is less symmetric than in the case without the additional heating by solar radiation [Colbeck, 1989b]. For example, internal heating plays an important role in Greenland (Kuipers Munneke et al. [2009], Dadic et al. [2008]). Note that in theory the alternating temperature gradients can be symmetrical, however, in nature this is rarely the case and complicated asymmetric alternating temperature gradients dominate.

2.3 Experimental setup and methods

To investigate the microstructural evolution of snow under the influence of alternating temperature gradients, we conducted time-lapse micro-computed tomography (micro-CT) experiments in a cold laboratory. In total, we did seven experiments with various settings similar to the experiments of Pinzer and Schneebeli [2009b]. The duration of the experiments was between two and three weeks. The 4D data sets were analyzed with various image processing tools, which are described in greater detail below. Table 2.1 gives an overview of the experimental settings and snow properties.

We chose to take rounded snow to be able to observe possible faceting in the course of the experiments. This snow represented polar and wind-affected snow as starting conditions for the experiments. New snow would have better reflected natural conditions in a seasonal alpine snowpack, but was not used to prevent simultaneous settlement of the snow during the experiments. Additionally, Pinzer and Schneebeli [2009b] already investigated new snow under the influence of an alternating temperature gradient. For Experiment 1 and Experiment 8 we collected freshly fallen new snow in front of the cold laboratory. For all other experiments we took snow samples from blocks of nature-identical snow produced in the cold laboratory with a snowmaker. The snowmaker is a machine, in which snow grows out of water vapor similar as in the atmosphere [Schleef et al., 2014a]. Both the fresh snow and the nature-identical snow were sieved into styrofoam boxes to achieve homogeneous snow blocks. The mesh size of the sieve was 0.5 cm. Before sampling, the styrofoam boxes filled with snow were stored for several weeks to months at -5°C to -20°C to become rounded and well sintered through

Table 2.1: *Overview of the experiments. Exp.: Experiment, τ: period of the sinusoidal temperature gradient, A: minimum and maximum amplitude of the sinusoidal temperature gradient, t: duration of the experiment, VOI: volume of interest, $\rho_{s,i}$: initial snow density, SSA_i: initial specific surface area, l_v: voxel size, f_a: acquisition frequency. Due to broken cables on the Snowbreeder, the snow surface temperatures could not be measured during Experiment 6 and hence the amplitude of the temperature gradient could not be calculated.*

Exp.	τ (h)	A (min./max.) (K m^{-1})	t (d)	VOI (mm^3)	$\rho_{s,i}$ (kg m^{-3})	SSA_i (m^2 kg^{-3})	l_v (μm)	f_a (h^{-1})
1	48	66/75	13.5	157.5	230	25.0	36	0.083
2	72	88/93	19.5	142.2	282	13.1	36	0.055
3	48	93/104	20.5	124.6	223	17.4	36	0.083
4	24	86/95	19.5	92.2	255	17.1	36	0.166
5	48	107/116	17	113.8	256	13.6	36	0.083
6	72	-/-	22	142.2	193	16.3	36	0.055
7	72	83/87	21.5	78.4	249	16.2	36	0.111
8	71*	73/73	26.5	142.2	180	15.0	18	0.125

*asymmetric: positive temperature gradient: 36 h, negative temperature gradient: 35 h.

isothermal metamorphism. The cylindrical snow samples had a diameter of 3.4 cm in Experiment 8 and 5.24 cm in all other experiments. The height of the snow samples was between 1 and 1.4 cm. The snow density was between 180 and 282 kg m^{-3}. The initial specific surface area was between 13.1 and 25 m^2 kg^{-1}.

For the micro-CT measurements the snow samples were placed in a special sample holder, the so-called Snowbreeder [Pinzer and Schneebeli, 2009a]. This device can impose a temperature gradient on a snow sample while performing time-lapse measurements in the Micro-CT. The temperatures on the top and bottom of the snow sample are controlled with Peltier elements. Hence, by controlling the snow surface temperatures directly, we apply a Dirichlet boundary condition to the snow samples in our laboratory experiments. In contrast, in nature the snow surface temperature results from heat fluxes, i.e. a Neumann boundary condition. To reach a homogeneous temperature distribution within the snow sample, the sample holder consists of a thin aluminum cylinder, surrounded by a cylinder of microporous foam. The foam thermally insulates the snow sample from the surrounding air and the aluminum cylinder imposes a uniform vertical temperature gradient. Details of the Snowbreeder are given in Pinzer and Schneebeli [2009a]. For Experiment 8 we used a Snowbreeder built by Scanco Medical, which has a smaller diameter and measures more stable than the older model due to a more robust construction leading to less defects during the measurements (Scanco Medical, personal

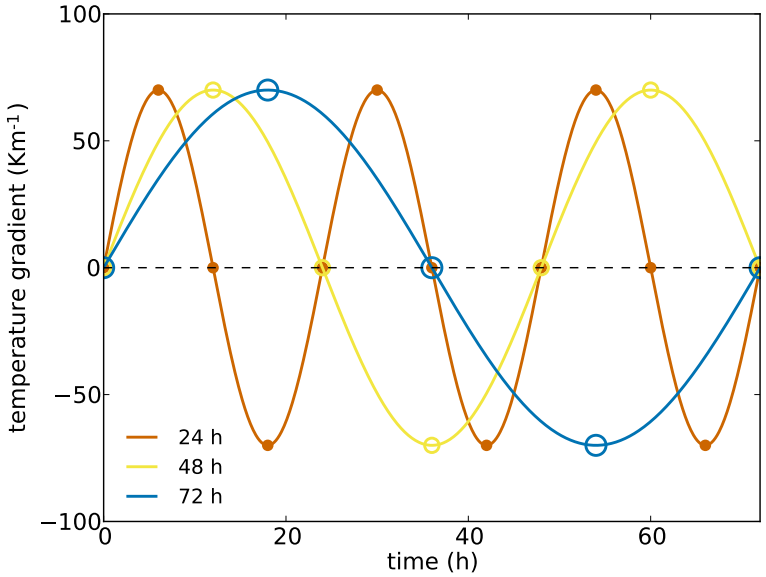

Figure 2.1: *Sketch of the applied symmetric sinusoidal temperature gradients with different periods. The circles mark the time of micro-CT measurements.*

communication, 2015). The setup and the measuring principle of the two Snowbreeders is the same. We inserted ice lenses on the top and bottom of the Snowbreeder to avoid the formation of air gaps between the device and the snow sample due to sublimation. In the Experiments 1 to 7 we applied a symmetric sinusoidal temperature gradient with an amplitude of up to 100 K m^{-1} on the snow samples. The period was set to 24 h, 48 h or 72 h (Fig. 2.1). We chose a maximum period of 72 h, because this is the life time of a snow structure under the influence of a unidirectional temperature gradient of the same amplitude as in our experiments [Pinzer et al., 2012]. Hence, we switched the temperature gradient at the limit where unidirectional temperature gradient metamorphism is fully developed. In Experiment 8 we applied an asymmetric sinusoidal temperature gradient with an amplitude of 73 K m^{-1} and a period of 71 h on the snow sample. The duration of the negative part of the sinusoidal temperature gradient was 35 h, 1 h less than the duration of the positive part. In all experiments the mean temperature of the snow sample was -5.2°C and the air temperature inside the computer tomograph was -5.7°C.

The snow samples were scanned periodically in the Micro-CT to follow the mircostructural evolution. In the Experiments 1 to 7, we did four micro-CT measurements per sine cycle, i.e. two at 0 K m^{-1} and one at each peak of the sinusoidal temperature gradient (Fig. 2.1). In Experiment 8 we did additional intermediate measurements between 0 K m^{-1} and the peaks, resulting in eight micro-CT measurements per sine cycle. The

peak energy and the current of the X-ray tube were set to 45 kVp and 88 μA, respectively. We chose a voxel size of 36 μm, which resulted in a good signal-to-noise ratio in the images and a reduced measurement time. A height of 7.49 mm was scanned in the middle of the sample, which took 65 minutes per measurement.

Due to the weight of the Snowbreeder the z-position counter of the Micro-CT occasionally loses steps, which leads to changes in the height position of the sample holder. However, a constant height position of the Snowbreeder is required for time-lapse studies, in which several measurements of one snow sample are compared. To account for the height position variations in the following analysis of the 3D images the height position of the Snowbreeder was measured continuously using an additional linear encoder ($\pm$1 nm). In addition to the vertical movement the Snowbreeder rotates during a micro-CT measurement. In the Experiments 3, 5, 6 and 7 the Snowbreeder did not fully return to the starting position after a full rotation. For these experiments, this error prevented a detailed analysis of the micro-CT images based on the comparison of subsequent images, because the measured snow structure is not exactly at the same horizontal position in different images.

The 4D data were analyzed with image processing scripts written in Python, IDL and IPL (Image Processing Language, developed by Scanco Medical AG). First, we selected a cubic volume of interest (VOI) in the 3D images, according to the representative volume of snow. The length and width of the VOI was always 5.2 mm. The height of the VOI varied between experiments due to the height position variations of the Snowbreeder. To take these variations into account, we selected the part of the 3D image which was always measured and we cut off the remaining top and bottom parts of the 3D image. Hence, the height of the VOI was between 2.9 and 5.2 mm, with smaller values in experiments with large height position variations of the Snowbreeder. A Gauss-filter with a sigma of 2.4 and a support of 3 voxels was applied to the VOI. After filtering the image was segmented into ice and air voxels. We selected the threshold for segmentation from the histogram of greyscale values in the VOI. The threshold was optimized by fitting the ice fraction according to the measured snow density. The chosen threshold was used for the segmentation of all images of one experiment.

To characterize the snow, we calculated structural parameters by triangulation of the ice surface with IPL. The same algorithm was used by Kerbrat et al. [2008] and Matzl and Schneebeli [2010]. One of the most important structural parameters is the specific surface area SSA, which is defined as the ratio of the ice surface area to the ice mass:

$$SSA = \frac{\text{ice surface area}}{\text{ice mass}} \tag{2.6}$$

We calculated the anisotropy a of the snow structure from the normalized chord lengths of the snow structure. Chords are lengths between intersections of lines with the interface between air and ice in the segmented 3D images of the snow structure. Hence, the chord lengths are a measure of the snow-structure size. The mean normalized horizontal and vertical chord lengths $l_{x/y}$ and l_z are given as follows:

$$l_{x/y} = \frac{\sum_{i=1}^{N} i p_{x/y}(i)}{\sum_{j=1}^{N} p_{x/y}(j)} \tag{2.7}$$

$$l_z = \frac{\sum_{i=1}^{N} i p_z(i)}{\sum_{j=1}^{N} p_z(j)} \tag{2.8}$$

$p_{x/y}(i)$ and $p_z(i)$ are the frequencies of horizontal and vertical chords of length i and N corresponds to the side length of the 3D image in mm. The normalized mean chord length l is a measure for the mean snow-structure size in all dimensions and is calculated with the following equation:

$$l = \frac{\sum_{i=1}^{N} i(p_x(i) + p_y(i) + p_z(i))}{\sum_{j=1}^{N} p_z(j)} \tag{2.9}$$

The anisotropy a of the snow structure is the ratio of the mean normalized vertical chord length l_z and the mean of the two mean normalized horizontal chord lengths l_x and l_y:

$$a = \frac{l_z}{(l_x + l_y)/2} \tag{2.10}$$

To see how the ice mass is relocated in the snow sample in the course of the metamorphism experiments we calculated the residence time of the ice voxels from the 3D images. The residence time is defined as the time between deposition and sublimation of ice voxels, i.e. the residence time is the age of ice voxels. We calculated the residence time by taking the difference of consecutive images, as described by Pinzer et al. [2012]. Additional to the residence time we calculated the mass turnover R, which is defined as the ratio of the relocated ice mass Δm_i between consecutive images to the total ice mass m_i:

$$R = \frac{\Delta m_i}{m_i} \tag{2.11}$$

We also estimated the water vapor mass flux with two different methods: the continuum model and particle image velocimetry PIV. In the continuum model, the snow sample is simplified as two ice plates with air in between. The distance between the ice plates is the same as the height of the snow samples and the temperature of the ice plates is the same as the top and bottom snow surface temperature measured in the experiments. The vertical vapor flux j_z between the two ice plates is calculated with Fick's law [Pinzer et al., 2012]:

$$j_z = -m_{H_2O} D_0 \frac{\partial c_e}{\partial z} \tag{2.12}$$

m_{H_2O} is the mass of a water molecule, D_0 is the water vapor diffusion coefficient in air and $\partial c_e/\partial z$ is the vertical water vapor concentration gradient. We calculated D_0 based on the mean temperature of the snow samples T_{mean} = -5°C and the mean air pressure at 1500 m a.s.l. (height of the cold laboratory in Davos) p_{mean} = 840 hPa [Massman, 1998]:

$$D_0 = 2.178 \cdot 10^{-5} \frac{1013\text{hPa}}{p_{mean}} \left(\frac{T_{mean} + 273.15}{273.15} \right)^{1.81} \tag{2.13}$$

This resulted in a value of $D_0 = 2.54 \cdot 10^{-5}$ m^2 s^{-1}. The vertical water vapor concentration gradient results from differences in water vapor pressure according to temperature differences between the ice plates. We calculated $\partial c_e/\partial z$ by calculating the equilibrium water vapour concentration above ice c_e both for the top and the bottom of the snow sample according to the ideal gas law:

$$c_e = \frac{e_i}{k_b T} \tag{2.14}$$

T is the snow temperature in K, e_i is the saturation water vapor pressure above ice and $k_b = 1.38 \cdot 10^{-23}$ J K^{-1} is the Boltzmann constant. We calculated e_i with the empirical Magnus formula [World Meteorological Organization (WMO), 2008]:

$$e_i = 6.112 \exp \left(\frac{22.46T}{272.62 + T} \right) \tag{2.15}$$

t corresponds to the snow temperature in °C.

The mass flux within the snow leads to sublimation and deposition of water vapor on snow grains, which causes an apparent displacement of the ice structure [Pinzer et al., 2012]. In the PIV method this apparent displacement of the ice structure is calculated from consecutive 3D images with an IDL program. The vertical mass flux j_z is calculated from the apparent vertical displacement d as follows:

$$j_z = \epsilon \rho_{ice} \frac{d}{\Delta t} \tag{2.16}$$

ϵ is the ice fraction, ρ_{ice} is the ice density and Δt is the time difference between two consecutive images. A more detailed description of the PIV method is given in Pinzer et al. [2012].

We used a IDL program to calculate the flat-area fraction of the snow, which is defined as the ratio of flat surface areas to the total surface area of snow. This program first determines the surface curvature of the ice in the VOI. Since small curvatures are seeds for flat surfaces, the ice surface is segmented according to a chosen curvature threshold of 1.2 mm^{-1}. Starting from these seeds, surfaces with a similar normal vector are combined as a flat area. For this the allowed angular difference of the normal vectors in one flat area was 15° and the area had to be larger than a defined minimum area of 0.06 mm^2 to be considered as a flat area (T. Theile, personal communication, 2015). We chose the values for the curvature threshold, the allowed angular difference and the minimum area such that they were comparable to a former experiment. In this experiment a unidirectional temperature gradient was applied to a snow sample and the flat-area fraction was calculated with the same program and the same threshold values [Pinzer, 2009]. Due to the chosen image resolution only flat areas larger than 36 μm x 36 μm were taken into account for the calculation of the flat-area fraction. Since this program did not analyze edges of the flat areas, we could not detect facets in the snow structure directly. Similar to this program, Calonne et al. [2014] computed mean curvature histograms of the snow structure to estimate the faceting degree of the snow structure.

In addition to the evaluation of the 3D images we took close-up images of snow grains before and after an experiment. Snow grains are single particles broken out of the sintered snow structure. In contrast, the snow structure includes also the bonds between single snow grains. Therefore we distinguish between snow grains and snow structure. The latter one can only be fully observed with the Micro-CT.

2.4 Results

2.4.1 Morphology, ice residence time, mass turnover

The microscopy and 3D images show a distinct evolution of the snow morphology (Fig. 2.2). The snow consisted initially of large rounded grains. After the experiments clusters of even larger snow grains had formed. When the alternating temperature gradient was symmetric, the snow structure was still rounded after three weeks. Small whisker-like structures grew on the surface of the grains. In contrast, the slightly asymmetric

alternating temperature gradient formed faceted grains.

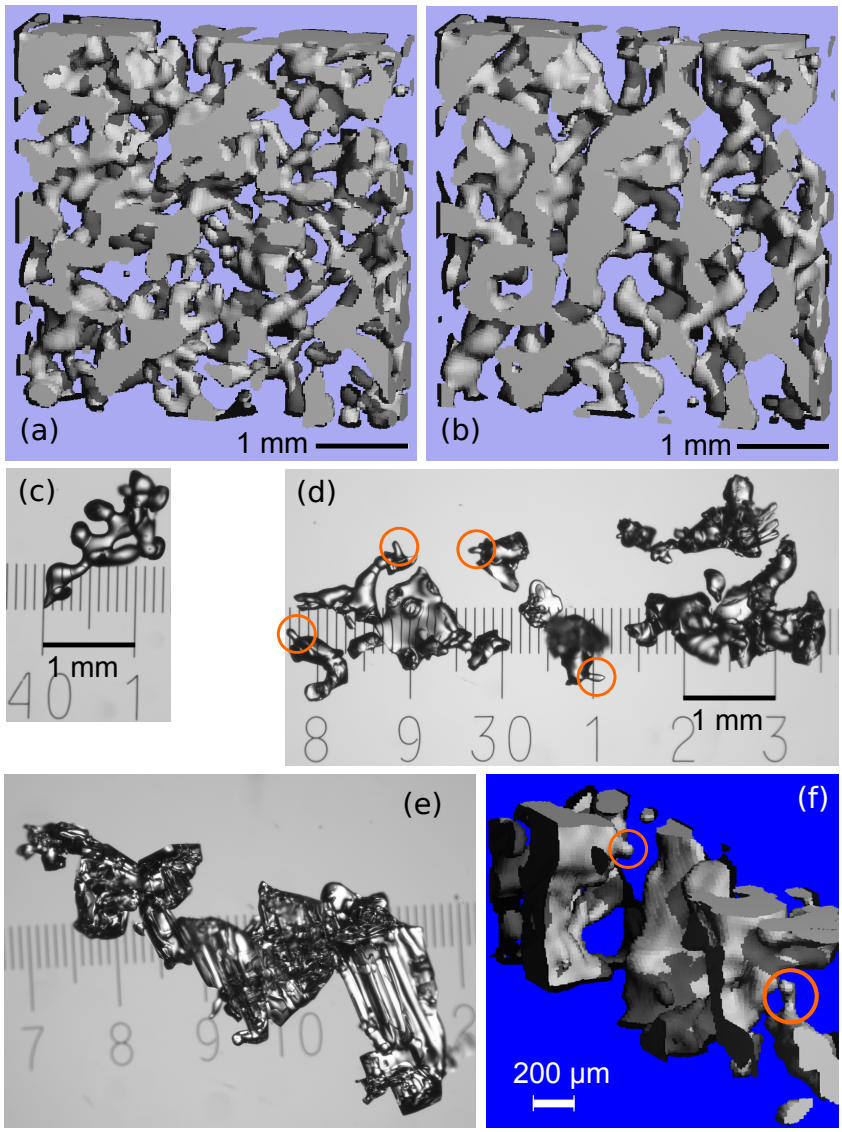

Figure 2.2: *Vertical sections of 3D images of the snow microstructure at the start (a) and at the end (b) of Experiment 2 in Tab. 2.1 (period of the sinusoidal alternating temperature gradient: 72 h, duration of the experiment: 19.5 days). Close-up image of the initially rounded snow in the beginning of the experiment (c), and close-up image and a section of a 3D image of the snow at the end of the experiment ((d) and (f)). Close-up image of snow at the end of Experiment 8 in Tab. 2.1 (e) (period of the asymmetric sinusoidal alternating temperature gradient: 71 h, duration of the experiment: 26.5 days). The circles in (d) and (f) mark the grown whisker-like structures. The scale in (c), (d) and (e) is labeled in millimeters.*

The coarsening of the snow structure is also visible in the distributions of the snow-structure size before and after an experiment (Fig. 2.3). The coarsening is least pronounced in the case of a symmetric alternating temperature gradient. In comparison, the asymmetric alternating temperature gradient led to a stronger coarsening, but less than in the case of a unidirectional temperature gradient. The size distributions do not show the evolution of the whisker-like structures observed in the microscopy images at the end of an experiment with a symmetric alternating temperature gradient. The mean, median and mode of the distributions are given in Tab. 2.2. Due to coarsening the mean and median increased, strongest for the unidirectional temperature gradient and least for the symmetric alternating temperature gradient. The median was always smaller than the mean, reflecting the right skewness of the distributions. This difference increased towards the end of the experiments.

Table 2.2: *The mean, median and mode of the snow-structure size distributions show in Fig. 2.3. Details about Experiments 2 and 8 are given in Tab. 2.1.*

Exp.	2 (72 h, symmetric)		8 (71 h, asymmetric)		unidirectional TGM	
	start	end	start	end	start	end
mean (mm)	0.47	0.53	0.41	0.59	0.25	0.48
median (mm)	0.43	0.47	0.4	0.54	0.23	0.43
mode (mm)	0.29	0.32	0.29	0.29	0.18	0.23

In addition to the coarsening, the snow structure developed a vertical orientation under the influence of alternating temperature gradients (Fig. 2.2 (a) and (b)). Accordingly, the anisotropy increased with time, independent of an asymmetry of the alternating temperature gradient (Fig. 2.4). Both the horizontal and the vertical snow-structure size increased with time (Fig. 2.5), according to the coarsening visible in the snow-grain images and the mean snow-structure size distributions. However, the vertical size increase was larger than the horizontal size increase, reflecting the increase in anisotropy.

The residence time of the snow structure gives more detail about the internal composition of the snow structure. The snow structure consisted of an old core (days to weeks old) and a young shell (few hours old) (Fig. 2.6). Figure 2.6 (a) is the last image of a movie of the residence time evolution, which is included in the online supplementary material (Movie S2), together with a movie of the evolution of the 3D microstructure of the same experiment (Movie S1). Both movies show the deposition and sublimation of ice voxels on the snow structure, which led to up and downward mass flux ("movement") of the snow microstructure according to the alternating temperature gradient and the resulting direction of the mass flux. When the alternating temperature gradient was asymmetric also the mass flux was asymmetric and only few parts of the snow structure

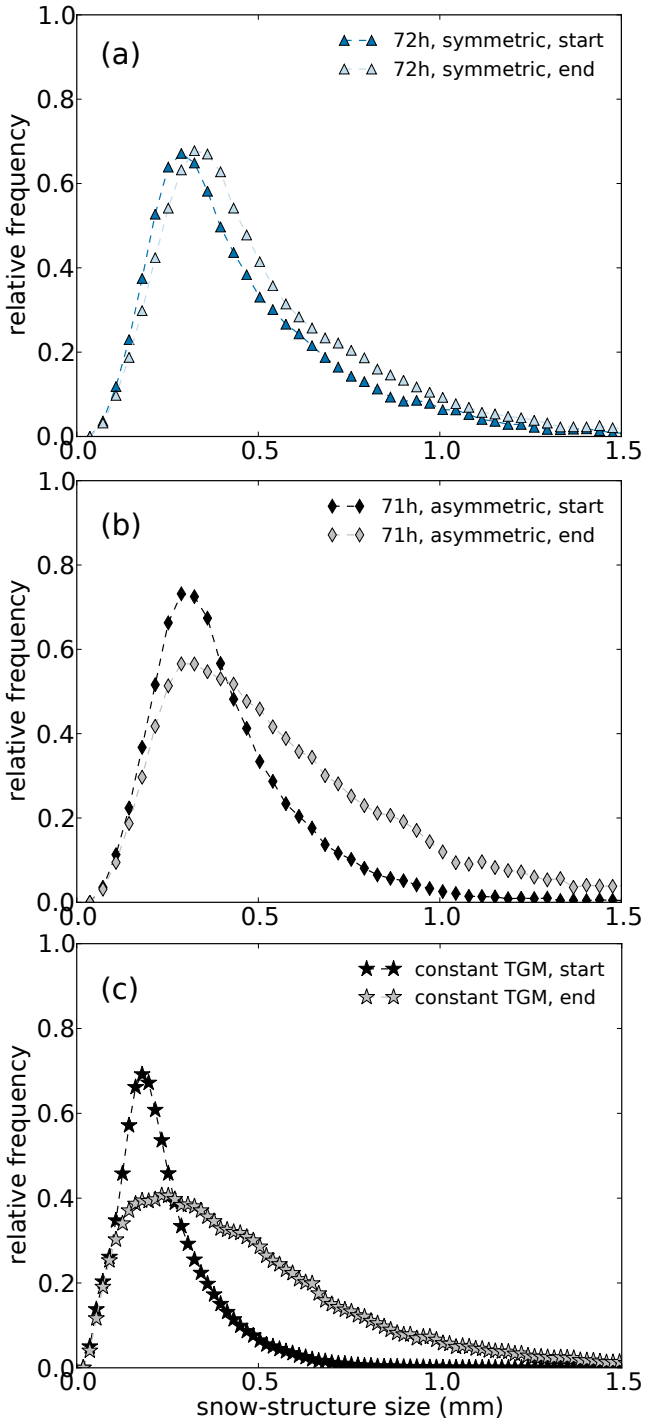

Figure 2.3: *Distribution of the snow-structure size at the start and at the end of Experiments 2 (a) and 8 (b) in Tab. 2.1 and an experiment with a unidirectional temperature gradient (c). The data for the unidirectional temperature gradient are taken from Pinzer [2009]. The mean, median and mode of the distributions are given in Tab. 2.2.*

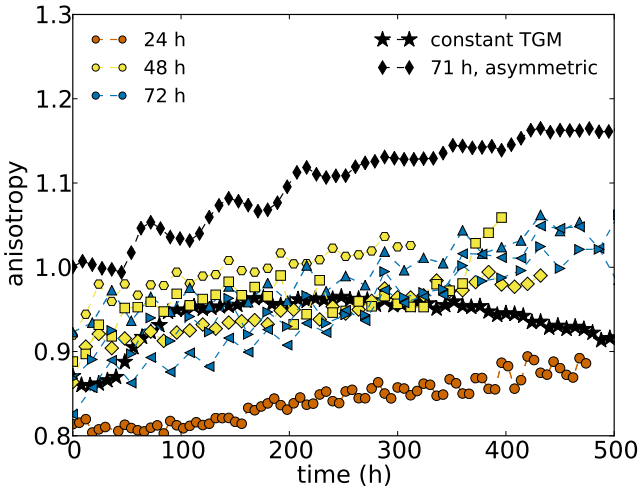

Figure 2.4: *Temporal evolution of the anisotropy for symmetric alternating temperature gradients with different periods, an asymmetric alternating temperature gradient and for a unidirectional temperature gradient (TGM) of 55 K m^{-1}. Hexagons: Experiment 1, triangles facing upward: Experiment 2, broad diamonds: Experiment 3, circles: Experiment 4, squares: Experiment 5, triangles facing left: Experiment 6, triangles facing right: Experiment 7 and narrow diamonds: Experiment 8 in Tab. 2.1. The data for the unidirectional temperature gradient are taken from Pinzer [2009].*

stayed to form an old core (Fig. 2.6 (b)). Fig. 2.7 and Fig. 2.8 show the distribution of the residence time within the VOI of two experiments with different periods of the symmetric sinusoidal temperature gradient for two different time steps. The old ice voxels form the core of the snow structure, while the young ice voxels form the shell of the snow structure with an equal distribution of ice voxels with a residence time in between. For a longer period of the alternating temperature gradient the old core was smaller than for a shorter period. After two sine cycles 65% of the ice voxels in the VOI formed the core in the experiment with a period of 24 h. In the case of a period of 72 h the core consisted only of 28% of the ice voxels in the VOI after two sine cycles. In both experiments the old core is still visible after 6 sine cycles, even though it decreased with time to 29% and 22% of the ice voxels, respectively. When the alternating temperature gradient was asymmetric, the old core decreased even more, to 0.07% (Fig. 2.9). In between the young shell and the small old core built up from the initial snow structure there are additional peaks in the histogram after each cycle. The size of the peaks decreased exponentially with time. From the histograms shown in Fig. 2.7, 2.8 and 2.9 we fitted the temporal evolution of the relative frequency of the shell and the core volume (Fig. 2.10). The shell is defined as all voxels having the youngest age, i.e. the measuring period. The core is defined by all voxels having the highest age, i.e. the actual duration

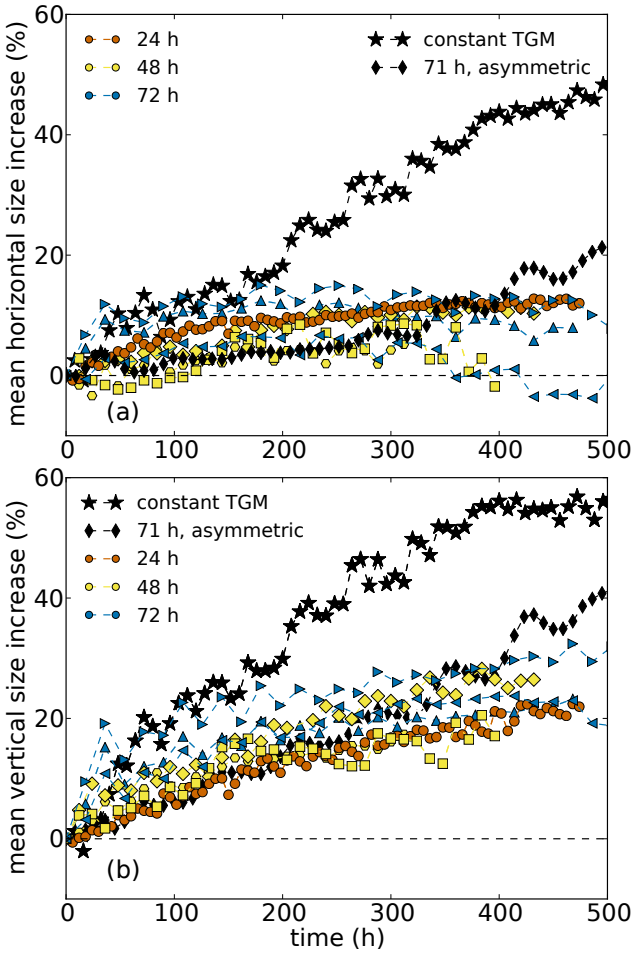

Figure 2.5: *Temporal evolution of the mean horizontal (a) and the mean vertical length increase (b) of the snow structure for symmetric alternating temperature gradients with different periods, an asymmetric alternating temperature gradient and for a unidirectional temperature gradient (TGM) of 55 K m^{-1}. Hexagons: Experiment 1, triangles facing upward: Experiment 2, broad diamonds: Experiment 3, circles: Experiment 4, squares: Experiment 5, triangles facing left: Experiment 6, triangles facing right: Experiment 7 and narrow diamonds: Experiment 8 in Tab. 2.1. The data for the unidirectional temperature gradient are taken from Pinzer [2009].*

of the experiment. For the shell evolution we calculated the linear fits $f_{s,24}$, $f_{s,72}$ and $f_{s,71}$ for the experiments with a symmetric alternating temperature gradient with a 24 h and a 72 h period and for the experiment with the asymmetric alternating temperature gradient with a 71 h period, respectively:

$$f_{s,24} = -1.2 \cdot 10^{-4} t + 0.19 \tag{2.17}$$

$$f_{s,72} = -3.6 \cdot 10^{-4} t + 0.34 \tag{2.18}$$

$$f_{s,71} = -9.2 \cdot 10^{-5} t + 0.16 \tag{2.19}$$

t corresponds to the time in hours. The correlation coefficients are $r_{s,24} = -0.19$, $r_{s,72} = -0.73$ and $r_{s,71} = -0.28$ and the p-values are $p_{s,24} = 0.09$, $p_{s,72} = 3.6 \cdot 10^{-5}$ and $p_{s,71} = 0.02$. In all three cases the shell decreased slowly with time. The core volumes of the snow structure decreased exponentially according to the two-term exponential fits $f_{c,24}$, $f_{c,72}$ and $f_{c,71}$:

$$f_{c,24} = 0.12 \exp(-2.8 \cdot 10^{-4} t) + 0.8 \exp(0.01 t) \tag{2.20}$$

$$f_{c,72} = 0.68 \exp(-0.03 t) + 0.32 \exp(-9.1 \cdot 10^{-4} t) \tag{2.21}$$

$$f_{c,71} = 0.65 \exp(-0.01 t) + 0.35 \exp(-0.34 t) \tag{2.22}$$

This results in half-life times of $t_{1/2,24} = 76$ h, $t_{1/2,72} = 43$ h and $t_{1/2,71} = 27$ h, respectively. The e-folding times are $t_{e,24} = 114$ h, $t_{e,72} = 78$ h and $t_{e,71} = 58$ h, respectively. In the experiments with a symmetric alternating temperature gradient the core volume approached the shell volume, whereas the asymmetric alternating temperature gradient led to a faster core-volume decrease even below the shell volume. In the symmetric case, the volume of the core decreased faster for a period of 72 h with time than for a period of 24 h.

We found a high mass turnover in the snow samples (Fig. 2.11). For a period of 72 h the mass turnover decreased linearly with time t according to the following linear fit:

$$R_{72} = -0.05 t + 59.85 \tag{2.23}$$

The correlation coefficient is $r_{72} = -0.9$ and the p-value is $p_{72} = 7.9 \cdot 10^{-5}$. For a period of 24 h the mass turnover was smaller than for the 72 h period. In the beginning the mass turnover was roughly one third of the mass turnover for a 72 h period. The mass turnover shows a statistically insignificant increase with time. The linear fit gives:

$$R_{24} = 0.02 t + 16.15 \tag{2.24}$$

The correlation coefficient $r_{24} = 0.26$ is much smaller than r_{72} and the p-value $p_{24} = 0.11$ is higher than p_{72}. The mean mass turnover for the asymmetric alternating temperature gradient was almost as high as the mass turnover for the 72 h period,

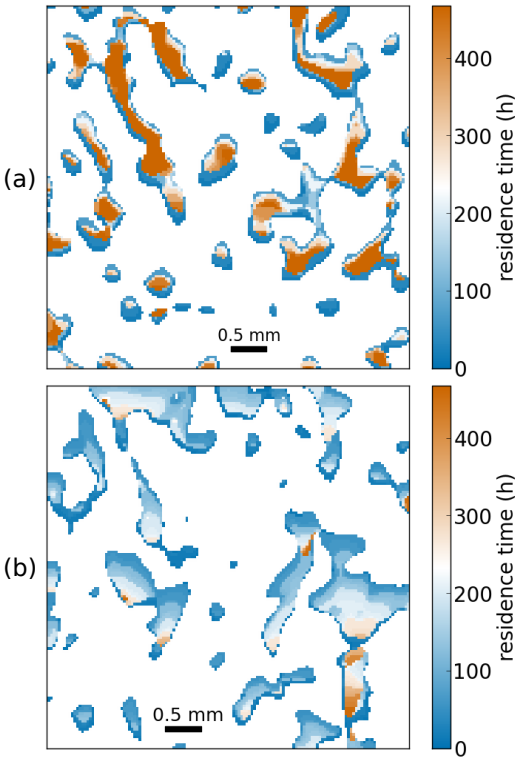

Figure 2.6: *Residence time of ice voxels after 468 h (≈ 20 days) in a 2D vertical slice of a 3D image of an experiment with a symmetric alternating temperature gradient (a) and an asymmetric temperature gradient (b). Period of the sinusoidal alternating temperature gradient: 72 h and 71 h, respectively (Experiment 2 and 8 in Tab. 2.1). The top and bottom of the volume of interest correspond to the top and bottom of the figure.*

according to the similar period. However, the mass turnover for the asymmetric alternating temperature gradient showed stronger variations. The mass turnover was higher when the temperature gradient was positive, reflecting the longer duration of the positive phase of the alternating temperature gradient. Like the mass turnover for the 72 h period the mass turnover for the asymmetric 71 h period decreased with time according to the following linear fit:

$$R_{71} = -0.06t + 55.29 \tag{2.25}$$

The correlation coefficient is $r_{71} = -0.53$ and the p-value is $p_{71} = 0.03$. To account for the large mass-turnover variations the values can be divided into values from the positive and the negative phase of the alternating temperature gradient, which results in the following linear fits:

$$R_{71,positive} = -0.04t + 62.44 \tag{2.26}$$

$$R_{71,negative} = -0.03t + 27.11 \tag{2.27}$$

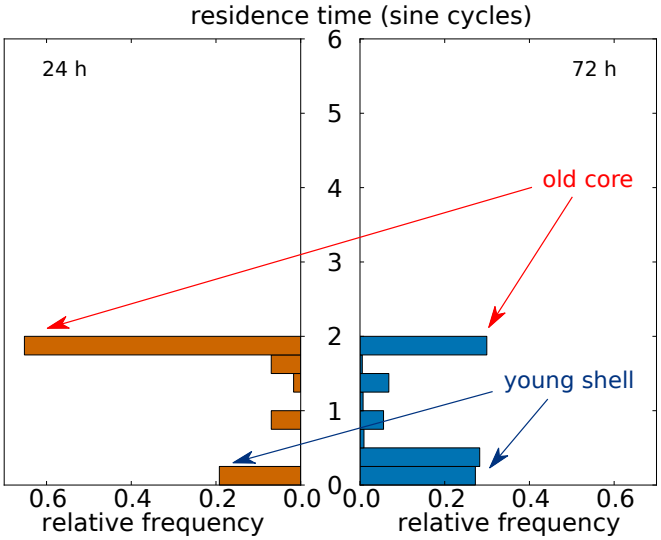

Figure 2.7: *Histograms of the residence time of ice voxels in a single 3D image after 2 sine cycles, for an experiment with a 24 h period (left, Experiment 4 in Tab. 2.1) and a 72 h period (right, Experiment 2 in Tab. 2.1), depicted as age pyramid. Mean amplitude of the alternating temperature gradient: 90 K m^{-1}.*

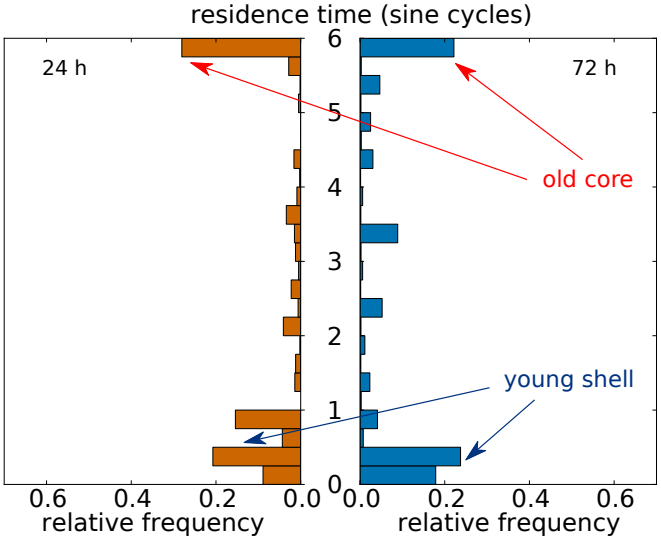

Figure 2.8: *Histograms of the residence time of ice voxels in a single 3D image after 6 sine cycles, for an experiment with a 24 h period (left, Experiment 4 in Tab. 2.1) and a 72 h period (right, Experiment 2 in Tab. 2.1), depicted as age pyramid. Mean amplitude of the alternating temperature gradient: 90 K m^{-1}.*

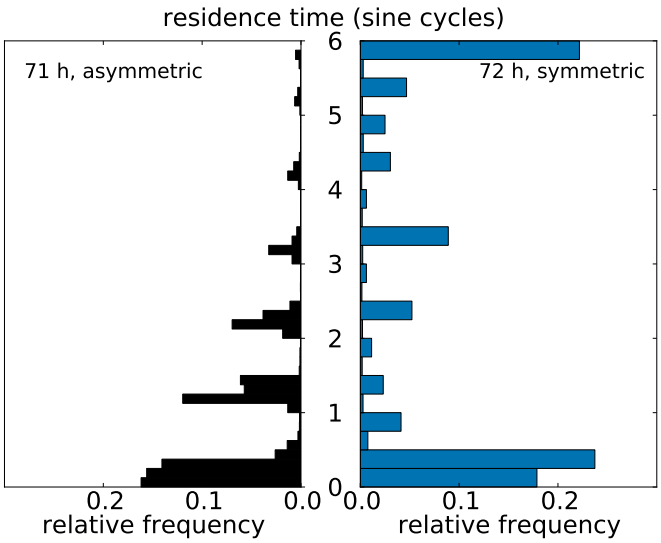

Figure 2.9: *Histograms of the residence time of ice voxels in a single 3D image after 6 sine cycles, for an experiment with an asymmetric alternating temperature gradient (left, Experiment 8 in Tab. 2.1), and a symmetric alternating temperature gradient (right, Experiment 2 in Tab. 2.1) depicted as age pyramid.*

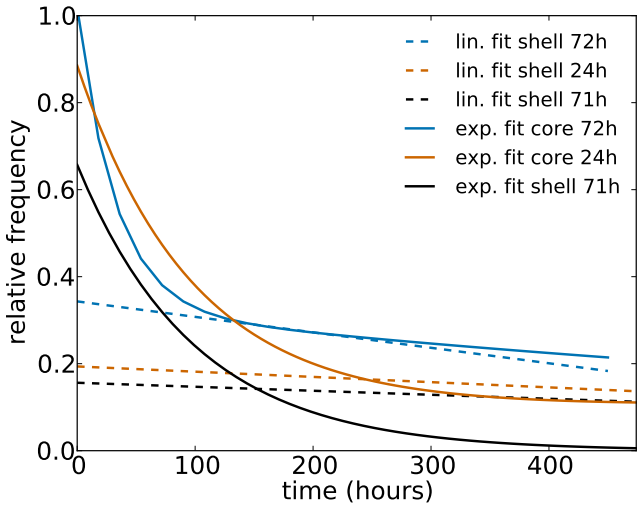

Figure 2.10: *Exponential and linear fits of the temporal evolution of the core and shell of the snow structure, for two experiments with a symmetric alternating temperature gradient (period: 24 h and 72 h, Experiment 4 and 2 in Tab. 2.1) and and an experiment with an asymmetric alternating temperature gradient (period: 71 h, Experiment 8 in Tab. 2.1). The fits and correlation coefficients are given in Eq. 2.17, 2.18, 2.19, 2.20, 2.21 and 2.22.*

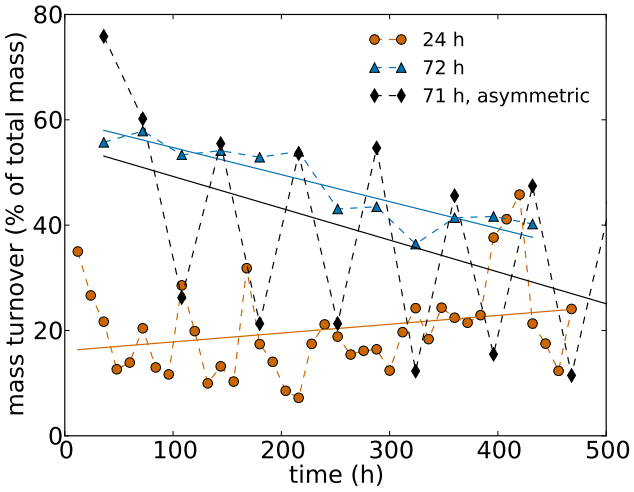

Figure 2.11: *Temporal evolution of the mass turnover, averaged over half of the sinusoidal temperature gradient. Triangles facing upward: Experiment 2, circles: Experiment 4 and narrow diamonds: Experiment 8 in Tab. 2.1. The lines are linear fits given in Eq. 2.23, 2.24 and 2.25.*

This separation of the values leads to higher r-values, i.e. $r_{71,positive} = -0.96$ and $r_{71,negative} = -0.9$. The p-values are $p_{71,positive} = 0.0001$ and $p_{71,negative} = 0.02$.

The temporal evolution of the mass flux was different compared to the mass turnover. The mass flux calculated with the continuum model clearly reflects the periodical signal of the alternating temperature gradient (Fig. 2.12). The amplitude of the mass flux was the same for both investigated periods and stayed nearly constant with time. The linear regressions are as follows:

$$j_{z,cont,24} = -2.1 \cdot 10^{-4} t - 0.001 \tag{2.28}$$

$$f_{z,cont,72} = -1.3 \cdot 10^{-4} t + 0.05 \tag{2.29}$$

t corresponds to the time in hours. The correlation coefficients are $r_{z,cont,24}$ = -0.025 and $r_{z,cont,72}$ = -0.014 and the p-values are $p_{z,cont,24} = 1.9 \cdot 10^{-17}$ and $p_{z,cont,72} = 1.5 \cdot 10^{-6}$. Both linear regressions show only a slight negative slope. The mean mass flux was $-6 \cdot 10^{-4}$ kg m^{-2} s^{-1} for both investigated periods.

Compared to the calculations with the continuum model, the calculations with PIV showed much larger variations and a less clear signal of the alternating temperature gradient (Fig. 2.13). For the 72 h period, the amplitudes were similar for the two calculations. For the 24 h period, large peaks occurred both for positive and negative mass

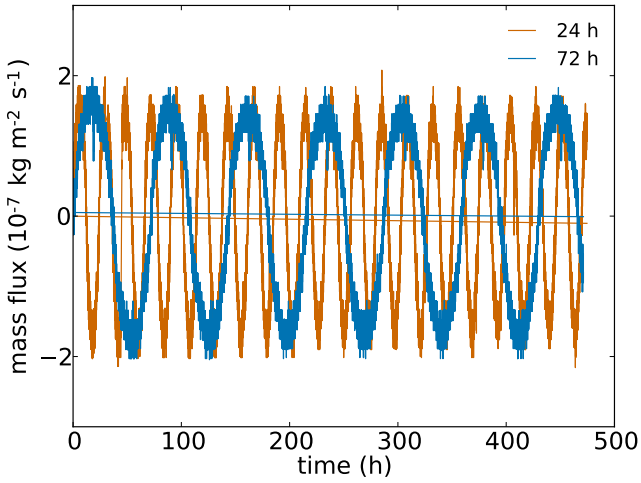

Figure 2.12: *Temporal evolution of the mass flux calculated with the continuum model (for a 72 h and 24 h period of the sinusoidal temperature gradient, Experiment 2 and 4 in Tab. 2.1, respectively). The lines are linear fits given in Eq. 2.28 and 2.29.*

fluxes calculated with PIV. For the mass fluxes calculated with the PIV method we calculated the following linear regressions:

$$j_{z,PIV,24} = -1.6 \cdot 10^{-3} t - 0.04 \tag{2.30}$$

$$f_{z,PIV,72} = -1.7 \cdot 10^{-3} t + 0.3 \tag{2.31}$$

The correlation coefficients are $r_{z,PIV,24}$ = -0.06 and $r_{z,PIV,72}$ = -0.1 and the p-values are $p_{z,PIV,72} = 0.59$ and $p_{z,PIV,24} = 0.59$. The mean mass fluxes calculated with PIV were $-2 \cdot 10^{-6}$ kg m^2 s^{-1} for the 24 h period and $-2 \cdot 10^{-7}$ kg m^2 s^{-1} for the 72 h period.

2.4.2 SSA evolution

We found that the SSA decreased less under the influence of both the symmetric and asymmetric alternating temperature gradients compared to a unidirectional temperature gradient (Fig. 2.14). This comparatively slight SSA decrease was more pronounced for the asymmetric alternating temperature gradient than for the symmetric case.

The reduced SSA decay during the alternating temperature gradient metamorphism occurred for all experiments with different periods of the sinusoidal temperature gradient. The higher initial SSA in Experiment 1 resulted from the different type of snow used

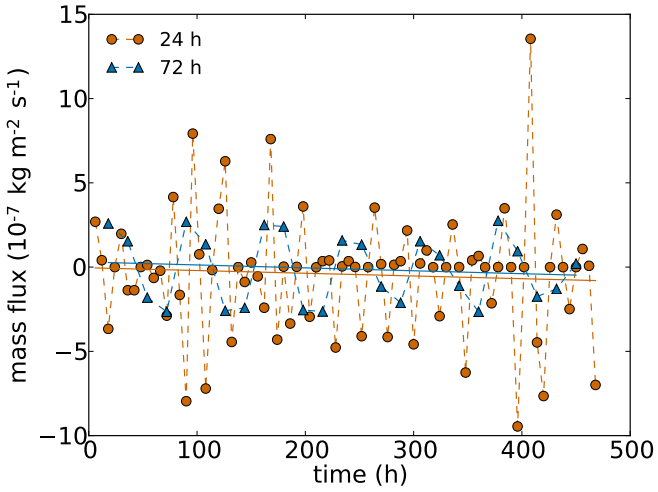

Figure 2.13: *Temporal evolution of the mass flux calculated with PIV (for a 72 h and 24 h period of the sinusoidal temperature gradient, Experiment 2 and 4 in Tab. 2.1, respectively). The lines are linear fits given in Section Eq. 2.30 and 2.31.*

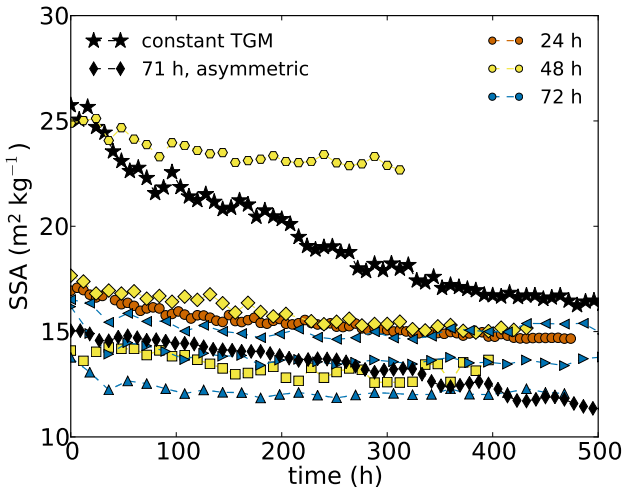

Figure 2.14: *Temporal evolution of the SSA for symmetric alternating temperature gradients with different periods, an asymmetric alternating temperature gradient and for a unidirectional temperature gradient (TGM) of 55 K m^{-1}. Hexagons: Experiment 1, triangles facing upward: Experiment 2, broad diamonds: Experiment 3, circles: Experiment 4, squares: Experiment 5, triangles facing left: Experiment 6, triangles facing right: Experiment 7 and narrow diamonds: Experiment 8 in Tab. 2.1. The data for the unidirectional temperature gradient are taken from Pinzer [2009].*

for this experiment compared to all other experiments. However, the temporal evolution was not influenced by this.

2.4.3 Dependency of the mass turnover on SSA and anisotropy

The mass turnover depends both on the SSA and the anisotropy of the snow structure. In contrast to a fine snow microstructure, a coarser structure with a lower SSA has less ice surface per volume, on which deposition and sublimation, i.e. the mass turnover, can occur. Thus, the mass turnover decreases with a coarsening of the snow microstructure and an associated decrease of the available ice surface per snow volume. In addition to the SSA, the mass turnover depends also on the anisotropy of the snow structure. To demonstrate these two dependencies we calculated the SSA and mass turnover for cuboids with different anisotropy, but with the same volume (Fig. 2.15). We reduced the SSA of the cuboids by increasing their volume in a way that the anisotropy stayed constant. For the mass turnover we assumed always the same mass flux, which resulted in the sublimation of an ice layer on top of the cuboid and the deposition of an layer of the same height on the bottom of the cuboids. Fig. 2.15 shows that the mass turnover increases with an increasing SSA and decreasing anisotropy. A structure aligned in the direction of the mass flux is sublimated on a smaller part of the surface than a structure aligned across the direction of the mass flux. Hence, the mass turnover decreases with time, when the anisotropy changes in snow such that the structure reorientates along the direction of the mass flux.

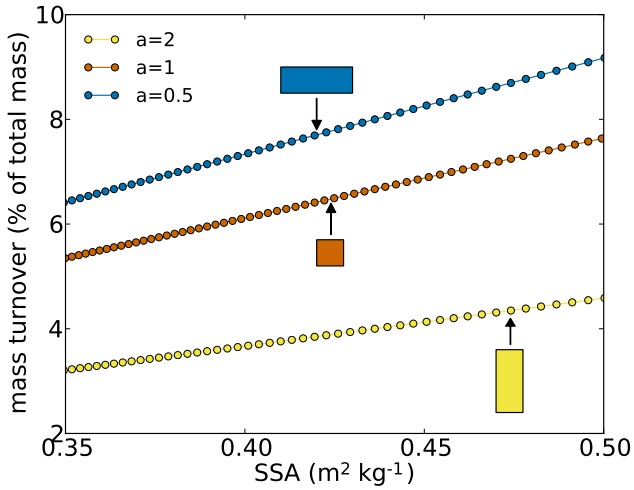

Figure 2.15: *Dependency of the mass turnover on the SSA, calculated for cuboids with different anisotropy, as indicated by the rectangles in the figure.*

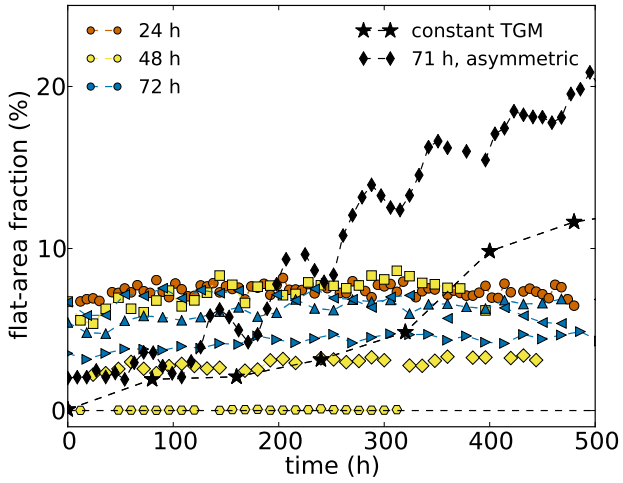

Figure 2.16: *Temporal evolution of the flat-area fraction for symmetric alternating temperature gradients with different periods, an asymmetric alternating temperature gradient and for a unidirectional temperature gradient (TGM) of 55 K m^{-1}. Hexagons: Experiment 1, triangles facing upward: Experiment 2, broad diamonds: Experiment 3, circles: Experiment 4, squares: Experiment 5, triangles facing left: Experiment 6, triangles facing right: Experiment 7 and narrow diamonds: Experiment 8 in Tab. 2.1. The data for the unidirectional temperature gradient are taken from Pinzer [2009].*

2.4.4 Flat-area fraction evolution

The flat-area fraction evolved similarly to the SSA. However, the flat-area fraction evolution was stronger affected by the symmetry of the alternating temperature gradient than the SSA evolution. For symmetric alternating temperature gradients the flat-area fraction was temporally nearly constant, independent of the investigated period. For an asymmetric alternating temperature gradient and a unidirectional temperature gradient (Fig. 2.16) the flat-area fraction increased strongly. The increase was larger in the experiment with an asymmetric alternating temperature gradient than in the experiment with a unidirectional temperature gradient. The lower flat-area fraction in Experiment 1 resulted from the different snow used for this experiment than for all other experiments. Similar to the SSA, the temporal evolution of the flat-area fraction was not influenced by the different snow.

2.4.5 Effect of settlement

To estimate a possible effect of settlement during our experiments, we calculated the settlement velocity v_s from the strain rate $\dot{\varepsilon}$:

$$v_s = \dot{\varepsilon} L = \frac{\sigma L}{\eta} = \frac{\rho_s V_s g L}{A_s \eta} \tag{2.32}$$

L is the scanned height of the snow sample, σ is the stress emerging from the overlying snow, η is the compactive viscosity of snow, ρ_s corresponds to the snow density, V_s is the volume of the overlying snow and A_s is the area of the overlying snow volume. As a representative example we calculated the settlement for Experiment 2 in Tab. 2.1, since the experimental setup in all other experiments was the same as in this experiment. In this experiment L was 11.05 mm, ρ_s was 282 kg m^{-3} and A_s was 2157 mm^2. Since the scanned volume was in the middle of the snow sample we assume the height of the overlying snow to be 1.8 mm, which results in $V_s = 3.96 \cdot 10^{-6}$ m^3. For a snow density of around 300 kg m^{-3} the compactive viscosity is between $3 \cdot 10^9$ and $5 \cdot 10^{10}$ Pa s [Shapiro et al., 1997]. With a mean of $\eta \approx 2.65 \cdot 10^{10}$ Pa s the settlement velocity was $v_s \approx 2 \cdot 10^{-12}$ m s^{-1}, which equals to 0.004 voxels between two consecutive measurements with a time difference of 18 hours.

2.5 Discussion

In this laboratory study we analyzed the microstructural evolution of rounded snow under symmetric and asymmetric alternating temperature gradients with time-lapse micro-computed tomography. We found that the snow structure became coarser and anisotropic. When the sinusoidal temperature gradient was symmetric, the snow became rounded and whisker-like structures grew on the surface of the snow structure. Faceting occurred when the alternating temperature gradient was even slightly asymmetric. This shows a very non-linear effect of alternating temperature gradients on the snow morphology. The snow structure consisted of an old core and a young shell. The SSA decreased less and the flat-area fraction increased less under the influence of a symmetric alternating temperature gradient than for a unidirectional temperature gradient, independent of the period of the symmetric alternating temperature gradient. The SSA decrease was slightly stronger and the flat-area fraction increase was much stronger for the asymmetric alternating temperature gradient than for the symmetric case.

2.5.1 Effect of sign-alternating mass fluxes

An alternating temperature gradient leads to a corresponding changing direction of the water-vapor mass flux within the snow. Hence, sublimation and deposition take turns on the snow structure, and the structure grows by vapor deposition, where it has been eroded by sublimation before. Therefore, when the alternating temperature gradient is symmetric, the snow structure has a core that is little influenced by the recrystallization process and only the outer shell of the snow structure gets continuously renewed. In contrast, Pinzer et al. [2012] found a complete recrystallization of the ice within few days during the unidirectional temperature gradient metamorphism, because the unidirectional water-vapor flux led to continuous sublimation and deposition of the ice on the same sides of the snow structure. Hence, even large crystals were completely sublimated and did not have an old core [Pinzer et al., 2012]. Since snow is a random heterogeneous material [Löwe et al., 2011], sublimation and deposition did not occur at exactly the same points of the snow structure even with an almost perfect repetition of the temperature cycle in our experiments. Therefore, the core of the snow structure decreased with time. The heterogeneity of the snow is also reflected in the distribution of residence times between the peaks for the core and the shell. In a perfectly homogeneous material only the peaks for the core and the shell would appear. For a longer period of the symmetric alternating temperature gradient the old core was smaller than for a shorter period, because the snow structure was exposed to sublimation for a longer time. Taking a closer look at Fig. 2.6 (a), the snow structure seems to be more sublimated at the bottom than at the top, since the youngest voxels are directly adjacent to the oldest voxels. This is probably just an effect of the 2D image. We cannot show the residence time in a 3D image, because this would only show the outer shell and not the core of the snow structure. We can rule out settlement and a negative mass balance for causing the apparent stronger sublimation at the bottom. The settlement velocity calculated in section 2.4.5 is too small. The calculated mass balance from the sublimated and deposited ice voxels for each time step gives a difference between sublimated and deposited ice voxels in a 3D image of only $0.12\% \pm 1.89\%$ of the ice voxels. The maximum and minimum difference was 4.75% and -5.5% of the ice voxels.

In the 71 h asymmetric alternating temperature gradient experiment the duration of the negative mass flux was longer than the duration of the positive mass flux. Hence, the resulting sublimation and deposition on the snow structure was also asymmetric. This effect eroded the old core of the snow structure much faster than under the influence of a symmetric alternating temperature gradient. At the same time, the asymmetric vapor flux led to the formation of a new core after each cycle. In one direction, the newly created shell was not completely eroded again since the mass flux causing sublimation had a shorter duration than the mass flux which led to the deposition before. The addi-

tional cores are visible as several peaks in the residence-time histogram. In a perfectly homogeneous snow structure several peaks of the same size would appear for the shell and the cores and the oldest core would disappear after a certain number of cycles. This disappearance of the oldest core depends on the snow-structure size in the direction of the mass flux and the amplitude and asymmetry of the mass flux. For a vertical mass flux, the core of a vertically orientated snow structure will stay longer than the one of a horizontally orientated structure. A stronger asymmetry, i.e. conditions closer to a unidirectional temperature gradient, and a larger amplitude would lead to a faster erosion of the oldest core. Since the snow structure is not perfectly homogeneous, the peaks of the cores decreased exponentially. Pinzer et al. [2012] found also an exponential distribution of residence times in snow for a unidirectional temperature gradient. The e-folding time of the distribution increased with time because the snow structure became larger, which requires more time to sublimate the snow structure. Similarly, we expect the oldest core to stay longer with time in the case of an asymmetric alternating temperature gradient, because of the observed coarsening and anisotropy evolution, i.e. an evolution in the direction of the mass flux.

The different mass fluxes resulting from different prevailing temperature conditions influence the redistribution of impurities and stable isotopes of snow. In contrast to unidirectional temperature gradient metamorphism, where the whole ice mass is relocated within days, only the shell of the snow structure interacts with the atmosphere when alternating temperature gradients occur [Grannas et al., 2007]. Depending on the asymmetry of the occurring alternating temperature gradient, the initial core of the snow structure might also interact with the atmosphere.

2.5.2 Morphology evolution of the snow-structure

In our laboratory experiments alternating temperature gradients resulted in similar morphologies like isothermal conditions and unidirectional temperature gradients, depending on the asymmetry of the alternating temperature gradient. So far, the formation of rounded snow was attributed to isothermal metamorphism and small temperature gradients. However, isothermal metamorphism is very slow, even at high temperatures [Kaempfer and Schneebeli, 2007]. Additionally, rather unidirectional or alternating temperature gradients occur and purely isothermal conditions are scarce in many natural dry snowpacks [Fierz, 2011]. Rounded grains observed in the field might have therefore also resulted from symmetric alternating temperature gradients.

Macroscopical observable facets result from a complex microscopic process, depending for example on local temperature gradients and vapor diffusion fields in the pore

space, which we did not analyse in detail in this study. We calculated the evolution of the flat-area fraction as an estimate for faceting in the snow structure. We expected to observe a stronger increase in the flat-area fraction for a higher period of the alternating temperature gradient due to the development of a more stable vapor diffusion field in the increasingly larger pores of the coarsening snow structure. However, we observed almost no increase in flat-area fraction in any of our experiments with a symmetric alternating temperature gradient, even though a large mass turnover occurred within the snow. This confirms the observation of rounded grains under a symmetric alternating temperature gradient by Pinzer and Schneebeli [2009b]. The changing direction of the mass flux prevented continuous ice growth in one direction and even for larger periods the time for ice growth in one direction was too short for an increase in flat areas. Certainly, a time (mass flux) threshold exists for facet growth under symmetric alternating temperature gradients, which was not reached in the case of the investigated periods. We did not observe a periodical signal in the flat-area fraction, which might have resulted from the periodically changing direction of the mass flux. The slight temporal increase of the flat-area fraction in Fig. 2.16 was probably caused by the slight temporal SSA decrease, because the flat-area fraction is calculated per total snow surface. When the snow surface decreases with time, the SSA decreases and the flat-area fraction can increase. We did not find an influence of differences in the pore size on the flat-area evolution in our experiments.

In contrast to faceting we observed whisker-like structures on the ice matrix under the influence of a symmetric alternating temperature gradient. These thin whisker-like structures are a sign of unstable crystal growth due to high local supersaturations [Kurz and Fisher, 1992]. Possibly, only parts of the snow structure with a favorable crystal orientation could grow fast enough during the short time for vapor deposition during one cycle, as also hypothesized by Adams and Miller [2003] and Adams et al. [2008]. Chen and Baker [2010] and Chen et al. [2013] observed the growth of similar structures between neighboring polycrystalline ice spheres due to vapor diffusion, though under isothermal conditions. The measured grain size of 50 to 800 μm on the ice spheres in the experiments of Chen and Baker [2010] fit to the width of around 100 μm of the whisker-like structures that we observed in our snow experiments. This preferential crystal growth is supported by the observation of Riche et al. [2013], who found a reorientation of the snow structure into the preferred crystal orientation during temperature-gradient snow metamorphism.

In contrast to the symmetric alternating temperature gradients, the asymmetric alternating temperature gradient led to an increase in the flat-area fraction. The flat-area fraction increased stronger than under unidirectional temperature gradient conditions, because the amplitude of the alternating temperature gradient was larger than the unidi-

rectional temperature gradient.

2.5.3 Geometric evolution

The rounded snow structure developing under isothermal conditions and under symmetric alternating temperature gradients differ in their geometric properties: while the snow structure is isotropic under isothermal conditions [Löwe et al., 2011], our anisotropy measurements show a vertically orientated snow structure under the influence of symmetric alternating temperature gradients. This anisotropy was even more expressed in the asymmetric case. The alternating temperature gradient can easily sublimate thin horizontal structures, while vertical structures stay and even grow. We hypothesize that this anisotropy could be an initiating factor for a less stable snowpack. A vertically orientated snow structure is already less stable than an isotropic structure. We hypothesize that when a layer of anisotropic rounded surface snow is buried under new snow layers, it will probably get subjected to a unidirectional temperature gradient at some point, depending on the height of the snowpack. The resulting metamorphism will lead to the formation of depth hoar and an additional vertical orientation of the snow structure.

Both symmetric and asymmetric alternating temperature gradients led to coarsening, typical for snow metamorphism. This is clearly visible in the close-up snow grain images (Fig. 2.2 (c)-(e)), in the 3D images of the snow structure (Fig. 2.2 (a) and (b)) and in the snow structure size distributions calculated from the chord length (Fig. 2.3). Due to the alternating direction of the mass flux this coarsening was less pronounced than the coarsening during unidirectional temperature-gradient metamorphism, when the mass flux is only directed into one direction. However, the coarsening was stronger when the alternating temperature gradient was asymmetric, i.e. when the conditions were closer to unidirectional temperature gradient conditions. The coarsening led to an increase of the snow-structure size both in the horizontal and in the vertical direction. However, the snow structure grew stronger in the vertical direction than in the horizontal direction, as already explained above. Grain coarsening due to alternating temperature gradients is also observed in geology. Mills et al. [2011] found a coarsening magma structure due to recrystallization caused by sinusoidal temperature gradients. In addition to the coarsening process, the crystals aligned in the direction of the mass flux according to the temperature gradient and joined into larger clusters of crystals [Mills et al., 2011], similar to our snow experiments.

Due to the coarsening of the snow structure, the SSA often decreases during snow metamorphism. An exponential SSA decay was often observed both for isothermal

snow metamorphism (e.g Kaempfer and Schneebeli [2007], Schleef and Löwe [2013]) and temperature-gradient snow metamorphism (e.g. Taillandier et al. [2007] and Pinzer et al. [2012]). Based on these measurements of a decreasing SSA with increasing snow age and density, Domine et al. [2007b] developed a parameterization for a logarithmic decay of the SSA with density. However, some observations show an SSA increase with time (e.g. Domine et al. [2009] and Wang and Baker [2014]). Wang and Baker [2014] measured an SSA increase for snow with initially large rounded grains under the influence of a high temperature gradient due to the growth of a more complex snow structure composed of depth hoar with many striae on the surfaces. Similarly, Domine et al. [2009] observed an SSA increase during the transformation of a melt-freeze crust consisting of large well-sintered grains into a layer of depth hoar under a large temperature gradient. Similar to the observations of Wang and Baker [2014], a more complex snow microstructure developed, leading to the SSA increase. In our experiments the SSA stayed nearly constant with time, even though we observed a coarsening of the snow structure. The whisker-like structures could have contributed with a large surface area similar to the growth of striated structures as observed by Wang and Baker [2014] to the reduced SSA decay. However, we did not see the development of these whiskers in the snow-structure size distribution (Fig. 2.3). Hence, the whisker-like structures did probably not cause the reduced SSA decay. Rather the changing direction of the mass flux led to the observed SSA evolution, because thus the initial snow structure stayed as a core and only the shell was slightly modified by the alternating sublimation and deposition without large changes in the SSA. Even though an asymmetric alternating temperature gradient eroded the initial snow structure much stronger, the SSA showed also a reduced decay.

The geometrical evolution of the snow structure influences the mass turnover. The temporally decreasing mass turnover both in the experiment with a 72 h period and in the experiment with an asymmetric alternating temperature gradient can be explained by the anisotropy evolution. Coarsening was too small, as indicated by the temporally constant SSA. Due to the increase in anisotropy at almost constant SSA the snow structure only reorientated along the direction of the mass flux, leading to a decreased mass turnover. The mass turnover for a 24 h period was smaller than for a longer period, since there was less time for sublimation and deposition to act on the snow crystals. Comparably large mass turnovers were also observed during other experiments with an alternating temperature gradient [Pinzer and Schneebeli, 2009b] and a unidirectional temperature gradient [Pinzer et al., 2012]. In contrast to the 72 h period, the mass turnover for the 24 h period shows more scatter. We expected a temporal decrease due to the observed anisotropy evolution, but the relationship was statistically insignificant. The VOI was smaller in this experiment than in the experiment with the 72 h period, which might have caused the large scatter. In addition to a larger VOI, a higher resolution

and more micro-CT measurements might improve the results. The large mass-turnover variations in the experiment with the asymmetric alternating temperature gradient were caused by the asymmetry of the temperature gradient. The positive phase of the alternating temperature gradient took longer than the negative phase resulting in a larger mass turnover at the end of the positive phase of the alternating temperature gradient.

In contrast to the mass turnover, the mass flux depends only on the magnitude and sign of the macroscopic temperature gradient [Pinzer et al., 2012] and not on the geometry of the snow structure, because the mass flux describes the mass transport through a plane and not within a volume. Therefore, the mass flux did not change due to coarsening, but changed the direction, following the sinusoidal temperature gradient. Accordingly, the mean mass flux was around zero for both calculations and periods. The amplitude of the mass flux was the same for all periods, since the amplitude of the applied temperature gradient was also the same.

2.5.4 Effect of initial snow properties

The initial snow conditions can have an influence on snow metamorphism. For example, a lower snow density favors the growth of large faceted grains and depth hoar (e.g. Akitaya [1974] and Pinzer et al. [2012]). However, we did not observe an effect of the initial snow density and SSA in our experiments with a symmetric alternating temperature gradient. For example, in Experiment 1 the SSA was higher and in Experiment 6 the density was lower than in all other experiments with a symmetric alternating temperature gradient. However, both experiments showed the same evolution in anisotropy, SSA and flat-area fraction like the other experiments with a symmetric alternating temperature gradient.

The initial snow density was lowest in the experiment with the asymmetric alternating temperature gradient, which might have caused the stronger increase in flat-area fraction, the slightly stronger SSA decrease and the stronger increase both in the horizontal and vertical size of the snow structure. However, the mass turnover evolved like in the comparable symmetric experiment with a 72 h period and in the symmetric experiment with a lower density we did not observe a comparable strong increase in the flat-area fraction. We assume that the increase in flat-area fraction was caused solely by the asymmetry of the alternating temperature gradient.

2.6 Conclusions

The presented laboratory study on the alternating temperature gradient metamorphism in rounded snow showed a microstructural snow evolution that expands the traditional differentiation of isothermal and temperature-gradient snow metamorphism. While an isotropic rounded snow structure evolves under isothermal conditions, symmetric alternating temperature gradients formed an anisotropic rounded snow structure. Under similar mass fluxes according to the amplitude of the temperature gradient the snow structure evolved much faster in the presence of a unidirectional temperature-gradient than during an alternating temperature gradient, as indicated in a stronger faceting and SSA decay [Calonne et al., 2014, 2011; Flin and Brzoska, 2008; Pinzer et al., 2012]. Hence, there is no unique relation between faceting and the magnitude of a temperature gradient such that faceting occurs increasingly with an increasing temperature gradient. The similar faceting under unidirectional and asymmetric alternating temperature gradient conditions shows that the snow-structure morphology alone cannot reveal which temperature conditions prevailed in a snowpack. Additionally, grain growth, i.e. the SSA decay, is not coupled to the occurring mass flux. The residence time, as calculated in this study, is a good indicator of whether unidirectional or symmetric or asymmetric alternating temperature gradients occurred.

Current snowpack models distinguish only between isothermal and unidirectional temperature-gradient conditions [Vionnet et al., 2012; Wever et al., 2015]. The negligence of alternating temperature gradients in models can have large effects, as for example in the SSA evolution. The SSA influences the snow albedo [Flanner and Zender, 2006], which in turn influences the melting of snow and has impacts on the Earth climate. Hence, a correct SSA evolution in models is important to estimate the albedo of a snowpack correctly. In current snow models, the SSA evolution is parameterized as an exponential decay according to a logarithmic relationship between the SSA and the snow density, based on measurements of a decreasing SSA with increasing snow age and density [Domine et al., 2007b]. However, in our laboratory experiments alternating temperature gradients led to a reduced SSA decay. Hence, after some time, the SSA of surface snow might be larger during the alternating temperature gradient metamorphism than during the modeled unidirectional temperature gradient metamorphism, leading to an underestimation of the albedo in the model. Therefore, a correct parameterization for the SSA evolution under alternating temperature gradient metamorphism should be developed for snowpack models. Neither an increasing nor a constant SSA is considered yet [Carmagnola et al., 2014].

The effect of an alternating temperature gradient on snow metamorphism is complex and not fully understood yet. Compared to the simplified conditions in our experiments

the temperature conditions found in natural snowpacks are much more complex. Alternating temperature gradients are almost always asymmetric in contrast to most of our experiments. Additionally, consecutive alternating temperature gradients with random periods can occur in a natural snowpack, leading to faceting or possibly also rounding of the snow structure. The results of this study show that the effect of an alternation of the temperature gradient in snow has to be considered in field observations and snowpack modelling in addition to isothermal and unidirectional temperature-gradient conditions.

Chapter 3

Snowbreeder 5: A Micro-CT device for measuring the snow-microstructure evolution under the simultaneous influence of a temperature gradient and compaction

Abstract

The instrumented sample holder Snowbreeder 5 is used to investigate the simultaneous influence of settlement on temperature-gradient snow metamorphism in time-lapse micro-computed tomography experiments. So far, experiments have only been done on temperature-gradient snow metamorphism without settlement or settlement under isothermal conditions. With the new device we can impose a constant temperature gradient on a snow sample and induce settlement by placing a passive load on top of the snow sample. The weight of the load can be varied, simulating various snow heights on top of the snow sample. Snow-temperature measurements on the passive load are

possible due to wireless data transfer via Bluetooth. The temperature gradient is set by controlling the air temperature inside the computer tomograph and by a Peltier element at the bottom of the snow sample. First experiments under isothermal conditions and a constant temperature gradient of 43 $\mathrm{K\,m^{-1}}$ showed that the settlement was reduced to almost half as soon as a temperature gradient was applied under otherwise almost equal snow conditions. The compactive viscosity in the isothermal experiment was in the range of literature values.

3.1 Introduction

Snow on the ground changes its microstructure continuously due to water vapour transport within the snow. This process, called snow metamorphism, depends on the environmental conditions. In simplified terms isothermal conditions lead to the formation of a rounded snow structure and a temperature gradient causes faceting and depth hoar formation. Simultaneously, snow densifies due to the overburden pressure caused by its own weight. De Quervain [1958] measured the structural snow evolution under the influence of both temperature-gradient metamorphism and simultaneous densification. He found that typical depth hoar formation due to a temperature gradient was less pronounced when the snow was densified. De Quervain [1958] could analyse the snow microstructure only from single snow crystal photographs and thin sections taken at the end of the experiments. Today, micro-computed tomography measures the full evolving 3D structure of snow. The microstructural changes modify the physical properties of snow, such as the thermal conductivity and mechanical strength [Calonne et al., 2014].

The influence of the thermal conditions on the microstructural snow evolution were investigated in time-lapse micro-computed tomography (micro-CT) experiments (e.g. Pinzer et al. [2012], Kaempfer and Schneebeli [2007]). Time-lapse Micro-CT measurements enable a non-destructive 3D and high-resolution observation of the snow microstructure evolution. For such experiments Schneebeli and Sokratov [2004] and Pinzer and Schneebeli [2009a] built an instrumented sample holder, the so-called Snowbreeder. With this sample holder a temperature gradient can be imposed on a snow sample while the sample is scanned periodically in a Micro-CT.

Initially, with Snowbreeder 1 a constant temperature gradient was applied to a snow sample inside the Snowbreeder [Schneebeli and Sokratov, 2004]. The bottom of the snow sample was heated with a film heater. With sensors both at the top and the bottom of the snow sample the heat flux and the snow temperature could be measured. With this

experimental setup temperature-gradient snow metamorphism was observed directly for the first time. Schneebeli and Sokratov [2004] measured the heat conductivity and found that it depends strongly on the snow structure and texture, even when the density stays constant. This showed the importance of a detailed understanding of the microstructural changes in snow. Pinzer et al. [2012] showed in further experiments that individual snow grains do not grow during temperature-gradient metamorphism. A high mass turnover occurs and the ice mass is completely relocated within few days.

Pinzer et al. [2012] refined the Snowbreeder 1. Alternating temperature gradients can be imposed to a snow sample in the Snowbreeder 2 by two Peltier elements at the top and the bottom. With the Snowbreeder 2 temperature variations similar to the diurnal cycle can be simulated. Pinzer and Schneebeli [2009b] found that even under high temperature gradients faceting does not necessarily occur, when the sign of the temperature gradient changes with a diurnal cycle. A rounded structure forms superficially similar to isothermal conditions. Even for higher periods than the diurnal cycle a rounded structure forms [Wiese and Schneebeli, 2017c].

For the experiments of Wiese and Schneebeli [2017c] the data transfer of the Snowbreeder was improved. The Snowbreeder has to rotate during the micro-CT measurements. At the bottom of Snowbreeder 2 cables are connected to slip rings to ensure the data transfer and Peltier-element control during the micro-CT measurements. At the top of Snowbreeder 2 a spiral cable was used. However, due to the low temperatures in the coldroom moving cables undergo rapid fatigue. This problem was solved in Snowbreeder 3 by using another slip ring at the top. Based on the Snowbreeder 3, Scanco Medical built a similar Snowbreeder, the Snowbreeder 4, in which additionally different snow sample heights are possible (Scanco Medical, personal communication, 2015). Ebner et al. [2014] extended the Snowbreeder construction so that temperature-gradient metamorphism can be investigated under the influence of an airflow. The cryogenic cell developed by Calonne et al. [2014] allows temperature controlled time-lapse tomography at room temperature.

With all these Snowbreeders important results on the influence of a temperature gradient on the snow microstructure were found. Settlement of snow is also a fundamentally important process. Experiments of snow settlement under isothermal conditions have been done for example by Schleef and Löwe [2013] and Theile et al. [2011]. Schleef et al. [2014b] developed a microcompression device for time-lapse micro-CT measurements to analyse the structural evolution of snow during compaction under isothermal conditions. So far both temperature-gradient metamorphism and settlement have been investigated separately with micro-computed time-lapse measurements.

In order to investigate the structural snow evolution under the influence of both a temperature gradient and overburden pressure in micro-CT time-lapse measurements another Snowbreeder was constructed based on the Snowbreeder 4, which we present here. A passive load can be placed on top of the snow sample in addition to imposing a constant temperature gradient. The vertical stress due to the passive load leads to snow settlement. In the following sections we describe in detail the construction and experimental setup of this Snowbreeder and show first measurement results.

3.2 Construction

The snow metamorphism experiments with the Snowbreeder 5 are done in a Micro-CT placed in a cold room at -15°C (Fig. 3.1). The Snowbreeder inside the Micro-CT (Fig. 3.2) is controlled with a LabVIEW program from a computer outside the cold room. The same program is used for saving the measured data.

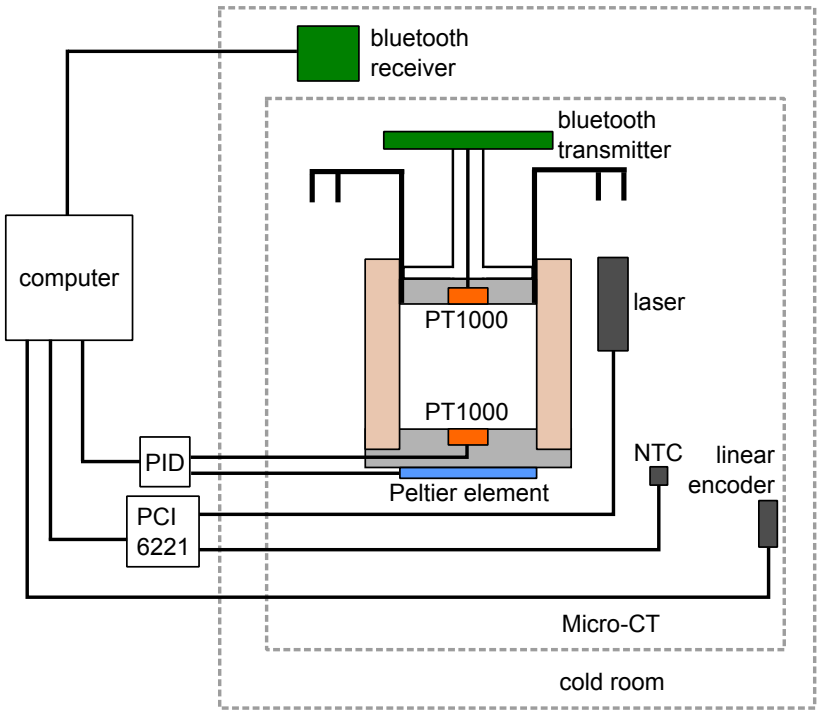

Figure 3.1: *Block diagram with the Snowbreeder 5 sensor locations and data flow.*

Like the previous Snowbreeders this new one is built to fit into the Micro-CT 80 from Scanco Medical. This desktop device provides enough space for cables for the

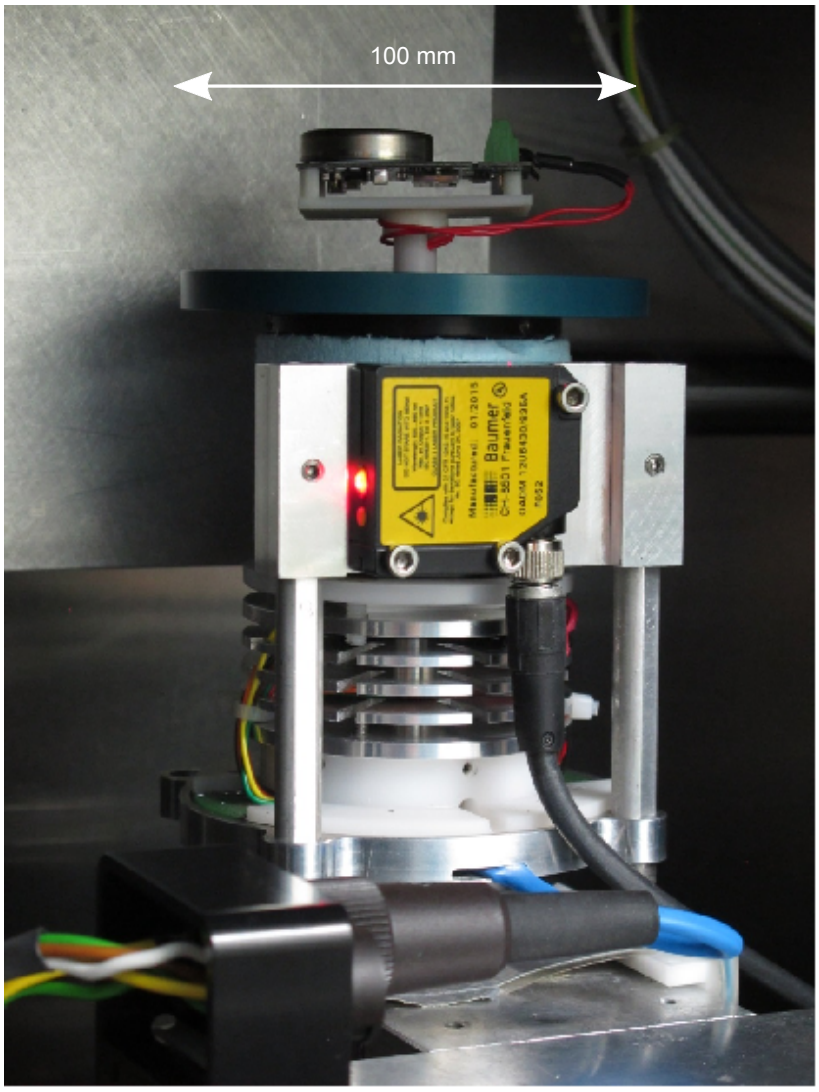

Figure 3.2: *Snowbreeder 5 inside the Micro-CT.*

Snowbreeder and the Snowbreeder itself. Additionally, this Micro-CT can run in the low temperatures inside the cold room. The temperature inside the Micro-CT changes as the X-ray tube heats up. To keep the temperature inside the Micro-CT constant a fan blows cold air from the cold room into the Micro-CT. With the heat from the X-ray tube and the cold air blown by the fan the temperature inside the Micro-CT can be varied.

The Snowbreeder is constructed such that micro-CT measurements are possible while imposing a temperature gradient on the snow sample and letting the snow settle. The

Snowbreeder has a diameter of 100 mm and a height of 126.6 mm to 145 mm (Fig. 3.3). During a micro-CT measurement the snow sample is moved up and down and rotated by 360° by step motors. Light materials were used for the construction such that the load capacity of about 1 kg of the micro-CT motors was not exceeded. No materials with high X-ray absorption coefficient, like iron, were used around the snow sample to avoid image artefacts. Due to the rotation of the Snowbreeder, data are transmitted to the computer via a slip ring or wirelessly via Bluetooth. The bottom of the Snowbreeder contains a pin to mount the Snowbreeder in the Micro-CT.

To measure the absolute position of the Snowbreeder during time-lapse tomography, we installed a linear encoder (accuracy = ± 1 nm) inside the Micro-CT. Thus, we measured the snow microstructure always at the same height in the snow sample and could position subsequent images of the time-lapse measurements absolutely.

The Snowbreeder consists of three parts which can be taken apart to insert a snow sample. The top and bottom part are both used to set the temperature gradient. The top part can additionally induce the snow settlement. The middle part consists of an aluminum cylinder (wall thickness of 0.5 mm) surrounded by a styrofoam cylinder (wall thickness of 7 mm), in which the snow sample is inserted. This part can be fixed with headless screws both to the top and the bottom part. The inner diameter of the aluminum cylinder, and hence the diameter of the snow sample is 34 mm.

The snow temperature is controlled with a Peltier element at the bottom of the Snowbreeder. The Peltier element and the snow sample are in contact via an aluminum heat distribution plate. This plate leads to a homogenous temperature of the snow bottom as the Peltier element is quadratic. On the other side of the Peltier element a passive heat exchanger removes the heat arising from the Peltier element during cooling. The top part of this Snowbreeder consists of aluminum acting both as heat distribution plate and passive heat exchanger. The snow temperature at the top is controlled by heat conduction through the top part and by setting the air temperature inside the Micro-CT. The highly porous styrofoam ring (WDS Ultra from Porextherm) around the snow sample thermally insulates the sample from the temperature inside the Micro-CT. The aluminum cylinder on the inner wall of the styrofoam ring acts as temperature guide. Due to the high thermal conductivity of aluminum (250 $W\,K^{-1}\,m^{-1}$) the cylinder leads to a uniform vertical temperature gradient in the snow sample. The thin aluminum cylinder does not affect the X-ray image quality.

The temperature at the top and bottom of the Snowbreeder is measured with PT1000 thermal resistors (S665PFY40BC from Minco) inserted into the heat distribution plates.

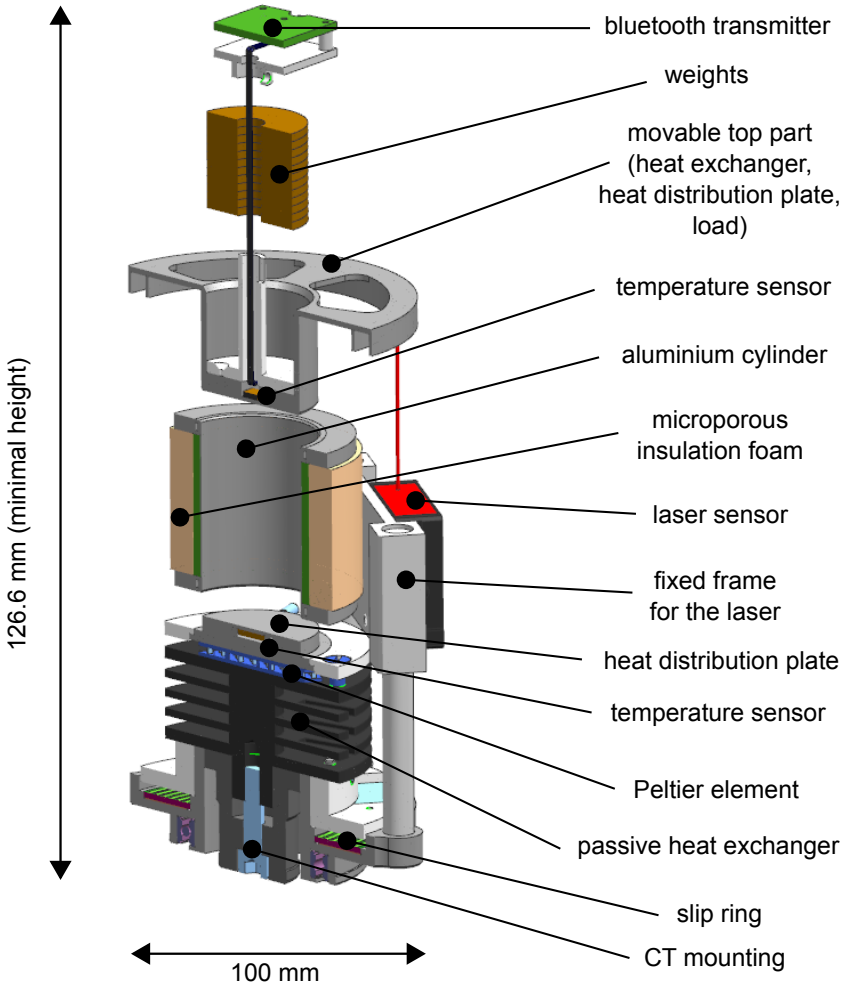

Figure 3.3: *Construction of the Snowbreeder 5.*

The PT1000 at the bottom provides the temperature feedback for the temperature control of the Peltier element at the bottom of the Snowbreeder. The distance between the temperature sensor and the Peltier element is 6 mm. The Peltier element is controlled with a proportional-integral-derivative (PID) controller (TC0806 from Cooltronic) outside the cold room. The PID values of the PID controller are as follows: proportional gain = 30, integral gain = 1 and derivative gain = 50. In contrast to the Snowbreeder constructed by Pinzer and Schneebeli [2009a] and Scanco Medical, the controller is programmed such that only a constant temperature can be set at the Peltier element.

The wiring of the Snowbreeder was constructed such that it allows for a full rotation of the Snowbreeder, which occurs during the time-lapse Micro-CT measurements. Hence, the cables for the PT1000 and the Peltier element at the bottom are connected to

Table 3.1: *Overview of the weights w and vertical stresses σ applied to the snow sample. The weight of the empty top part corresponds to the minimum and the full top part with all weight discs is the maximum. The according snow depths h_s of snow with two different densities ρ_s are calculated as an example with Equation 3.2.*

	w (g)	σ (Pa)	h_s (m)	
			$\rho_s = 100\,\mathrm{kg\,m^{-3}}$	$\rho_s = 300\,\mathrm{kg\,m^{-3}}$
disc	10	108	0.11	0.04
empty top part	61	658	0.67	0.22
top part + all discs	161	1736	1.77	0.59

an axial slip ring below the Snowbreeder. The data of the PT1000 at the top are transmitted wirelessly via Bluetooth. The Bluetooth transmitter is attached to the top part of the Snowbreeder. The Bluetooth receiver lies outside the Micro-CT in the cold room and is directly connected to the computer outside the cold room. The temperature values are read and saved by the LabVIEW program at a rate of 0.2 Hz.

In addition to the snow temperature, the air temperature inside the Micro-CT is measured with a NTC sensor installed close to the Snowbreeder. The data are transmitted via the NI data acquisition card PCI 6221 to the computer outside the cold room. At a rate of 0.2 Hz an average value of 10 values is measured and saved.

The settlement of the snow sample is induced by placing a passive load on top of the snow sample. This top part of the Snowbreeder lies on top of the snow sample and can slide downwards inside the aluminum cylinder as the snow settles due to the weight. Ten additional weight discs can be inserted into this part to increase the vertical stress on the snow sample. These metal discs have a diameter of 30 mm and a weight of 10 g$\pm$0.02 g each. The minimum weight on the snow sample, i.e. the weight of the top part without the extra weights, is 61 g. The maximum weight is 161 g, when all ten discs are inserted. Additionally, the top part can be fixed with headless screws on the aluminum cylinder so that no settlement occurs. The different weights on the snow sample simulate different snow heights on top of the snow sample (Table 3.1). The vertical stress σ and the snow depth h_s of snow lying on the snow sample according to the chosen weight can be calculated as follows:

$$\sigma = \frac{mg}{A_s} \tag{3.1}$$

$$h_s = \frac{\sigma}{\rho_s g} \tag{3.2}$$

m_s, A_s and ρ_s are the mass, area and density of the overlying snow.

The settlement is measured with a laser sensor (OADM 12I6430/S35A from Baumer) measuring the distance to the rim of the top part. The laser is fixed with a metal frame on the side, which does not move during a CT measurement so that the image does not get disturbed by the laser. The data from the laser is also transmitted via the NI data acquisition card PCI 6221 to the computer outside the cold room. Like the measured temperatures, the distance measurement data are saved with a rate of 0.2 Hz by the LabVIEW program. The measurement range of the laser is 10 mm between 16 and 26 mm distance and the resolution is 5 μm.

The temperature gradient across the snow sample leads to water vapour transport, also into the narrow free space between the aluminum cylinder and the top part of the Snowbreeder. To prevent the sliding top part from freezing due to the water vapour transport, it is lubricated with a thin film of silicone grease, so that the movement is not disturbed.

The sample height has to be in the range of 23 to 33 mm due to the measurement range of the laser. To have unconstrained conditions at the walls during settlement, the height of the snow sample should be chosen to be half of the diameter of the snow sample, i.e. a height of 17 mm [ASTM, 2011]. Since this is below the minimum sample height at which the laser can still measure the distance, the snow sample has to be raised by inserting an ice lens at the bottom with a height of up to 16 mm. In any case, an ice lens has to be inserted at the warmer end of the snow sample as a water vapour supply. Without an ice lens, an air gap would form between the heat-distribution plate and the snow sample at the bottom or an apparently increased settlement would be measured at the top due to sublimation.

3.3 Measurements

The goal of measurements with the presented Snowbreeder 5 is the analysis of the microstructural snow evolution under the influence of both a constant temperature gradient and an overburden pressure, similar to natural conditions.

In the first two test experiments we measured the settlement under isothermal conditions and a constant temperature gradient of 43 K m^{-1}. For both experiments we took nature-identical snow, which was stored in a styrofoam box for several months to get rounded (Fig. 3.4a). The initial snow density was around 230 kg m^{-1}. The initial specific surface area SSA, i.e. the ratio of the ice surface area to the ice mass, was 13.25 m^2 kg^{-1} and the initial pore size was 0.5 mm for both experiments. We placed the maximum

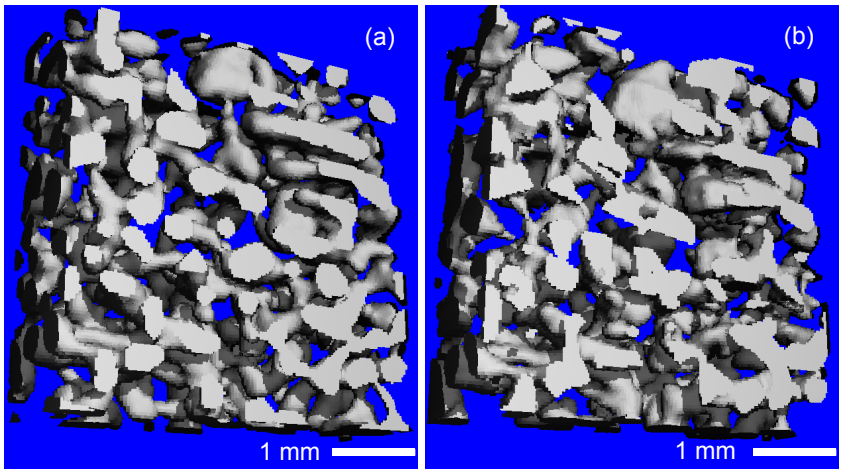

Figure 3.4: *Reconstructed micro-CT images of the temperature-gradient experiment at the beginning (a) and after four days (b). The temperature gradient in the snow sample was 43 K m^{-1}.*

weight of 161 g on top of the snow sample. For the isothermal conditions, we turned off the Peltier element and controlled the snow temperature only with the air temperature inside the Micro-CT, which was set to -10°C in both experiments. The temperatures measured at the top and the bottom of the Snowbreeder were stable (±0.1°C) besides a small increase of maximum 0.3°C during the Micro-CT measurements (Fig. 3.5). In comparison, the temperatures of the Snowbreeder developed by Ebner et al. [2014] showed variations of around ±0.4°C and an increase of up to 0.5°C during Micro-CT measurements. We improved the temperature stability of Snowbreeder 5 primarily with an improved ventilation of the Micro-CT to prevent effects of temperature variations in the cold room that occurred in the measurements of Ebner et al. [2014]. Secondly, we use different PID values for the controller of the Peltier element. Temperature-gradient changes due to a decreasing sample height due to the induced compaction are negligible for a deformation of up to 2%.

For the micro-CT measurements we chose the peak energy and the current of the X-ray tube to be 45 kVp and 88 μA, respectively. The integration time was 300 ms and the voxel size was 36 μm. We measured a height of 5.6 mm in the middle of the snow sample. With these settings one measurement took 50 minutes. The measurement duration of one scan should not be much longer. A small imbalance of the top part of the Snowbreeder disturbs the distance measurements during a Micro-CT measurement. Because the Snowbreeder rotates during the measurement, the imbalance of the top part leads to large variations in the distance measured by the laser. Therefore, the distance data are unusable during a Micro-CT measurement. We took a micro-CT measurement

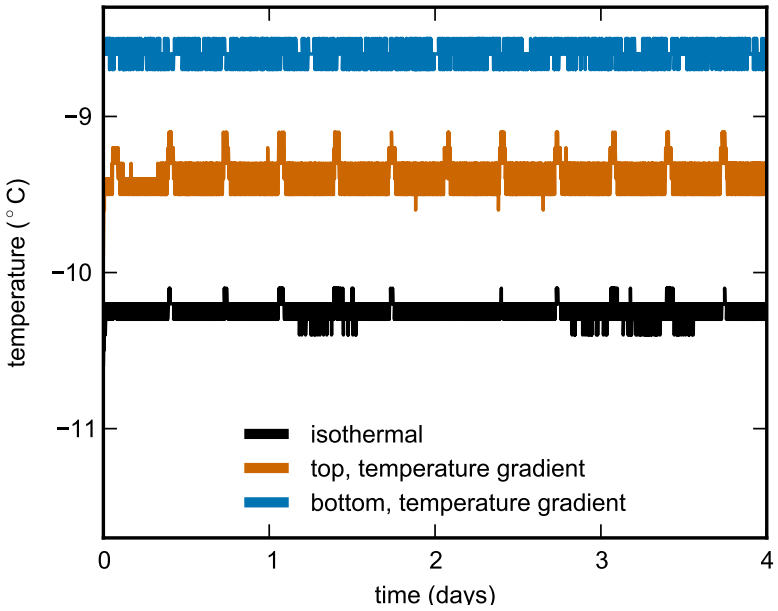

Figure 3.5: *Top and bottom temperature measured at the Snowbreeder during the isothermal and the temperature-gradient experiment. In the isothermal experiment both temperatures were the same, in the temperature-gradient metamorphism experiment the temperature gradient in the snow sample was 43 K m^{-1}.*

every eight hours.

According to Equation 3.2 we calculated the stress of the snow's own weight to be 38 Pa for a sample height of 17 mm and a snow density of 230 kg m^{-3}. Compared to the stress of the passive load, i.e. 1736 Pa, the additional stress of the snow is 2%, which we consider negligible. Hence, the density measurements in the middle of the snow sample are representative for the whole snow sample, because the stress differs only by 38 Pa between the top and the bottom of the sample.

For the analysis of the 3D images we selected a cubic volume of interest (VOI) within the entire image. This VOI had a side length of 5.4 mm, according to the representative volume of snow. We applied a Gauss filter with a sigma of 1 and a support of 2 voxels and segmented the greyscale images into ice and air voxels with a threshold based on the histogram of the greyscale values. The density calculation in the segmented VOI was voxel-based and the SSA was calculated by triangulation of the ice surface. We did the entire image processing with IPL (Image Processing Language, developed by Scanco Medical AG).

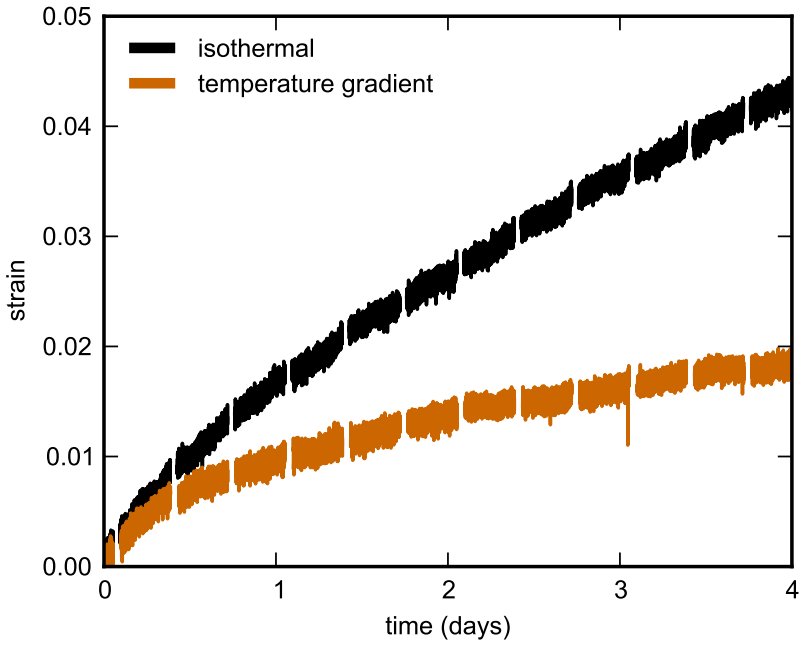

Figure 3.6: *Temporal strain evolution calculated from the laser distance measurement with Equation 3.3. The temperature gradient in the snow in the temperature-gradient experiment was 43 K m^{-1}.*

3.4 First results

In both experiments we measured a monotonous decrease in snow height. We calculated the strain ϵ from the measured laser distance d_l as follows:

$$\epsilon = \frac{d_{l,0} - d_l}{L} \tag{3.3}$$

$d_{l,0}$ is the initial distance measured with the laser and L is the height of the snow sample, which was $L = 17.64$ mm and $L = 17.17$ mm in the isothermal and in the temperature-gradient experiment, respectively. Due to settlement the strain increased temporally in both experiments (Fig. 3.6). This increase slowed with time due to the decreasing settlement. The strain increase was slower under the influence of a constant temperature gradient than under isothermal conditions.

Corresponding to the settlement, we measured the snow densification in the micro-CT images of both experiments (Fig. 3.7). In the isothermal experiment the strain increased by 4.3% and in the temperature-gradient experiment the strain increased by 1.9%. This

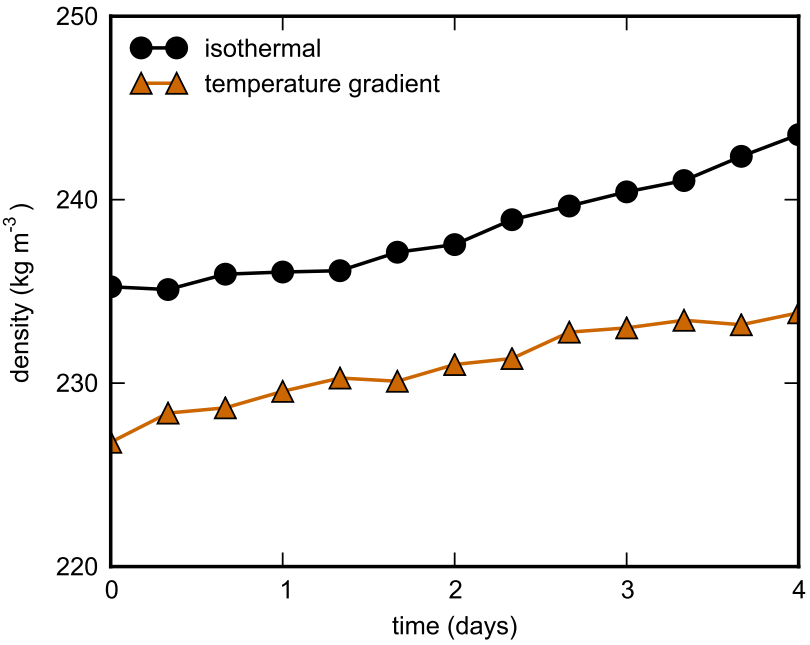

Figure 3.7: *Temporal evolution of the snow density derived from the micro-CT images. The temperature gradient in the snow in the temperature-gradient experiment was 43 K m^{-1}.*

strain increase corresponds to a density increase of 10.2 kg m^{-3} and 4.3 kg m^{-3}, respectively. We measured a density increase of 8.6 kg m^{-3} and 7.1 kg m^{-3} in the isothermal and in the temperature-gradient experiment, respectively. The difference between the density increase calculated from settlement versus the increase observed in the images may have several reasons. We guess that temperature-gradient metamorphism led to an inhomogeneous density distribution, which could not be observed in the imaged volume.

In both experiments the SSA decreased with time due to coarsening of the snow structure. We observed a stronger SSA decrease in the temperature-gradient experiment. In this experiment, additionally faceting occurred parallel to the densification due to the imposed temperature gradient (Fig. 3.4b).

We estimated the compactive viscosity η of the snow from the strain rate $\dot{\varepsilon}$. The strain rate $\dot{\varepsilon}$ is related to the applied vertical stress σ by [Schleef and Löwe, 2013]:

$$\dot{\varepsilon} = \frac{1}{L}\frac{\Delta L}{\Delta t} = \frac{v_s}{L} = \frac{\sigma}{\eta} \tag{3.4}$$

L is the height of the snow sample and v_s is the settlement velocity. Hence, we calculated the compactive viscosity η as follows with the measured settlement:

$$\eta = \frac{\sigma L}{v_s} \tag{3.5}$$

The stress applied by the maximum weight on the snow sample was 1736 Pa (Tab. 3.1). After 12 hours the viscosity was still similar in both experiments with values of 10.6 GPa s and 8.2 GPa s in the temperature-gradient experiment and in the isothermal experiment, respectively. After four days, the compactive viscosity increased stronger in the temperature-gradient experiment than in the isothermal experiment, according to the observed strain rate, resulting in values of 32.4 GPa s and 14.1 GPa s, respectively.

In the temperature-gradient experiment, the snow temperature was maximum 1.7°C higher than in the isothermal experiment. This temperature difference corresponds to a 0.6% difference in homologous temperature of, i.e. the ratio of the snow temperature to the melting point of snow.

3.5 Conclusions

We developed the new Snowbreeder 5, which imposes a constant temperature gradient on a snow sample and induces settlement simultaneously while measuring the snow microstructure with time-lapse micro-CT measurements. The temperature gradient is set with a Peltier element at the bottom and controlling the air temperature at the top. A passive load is placed on top of the snow sample to induce the settlement. By inserting several weight discs the vertical stress can be varied. By this the overburden pressure of snow of various heights, typical for a natural snowpack, can be simulated on top of the snow sample. The settlement is measured with a laser distance sensor. Simultaneous snow temperature measurements are enabled by wireless data transfer via Bluetooth at the top of the Snowbreeder.

We did two test experiments with rounded snow under isothermal conditions and a constant temperature gradient. In both experiments we observed a temporal increase in strain, density and compactive viscosity due to settlement. Especially in the temperature-gradient experiment the density increased less in the 3D images than calculated from settlement, which might have resulted from an inhomogeneous density distribution due to temperature-gradient metamorphism. However, in future we can additionally measure the full snow sample to attain more data on the structural snow evo-

lution, which should show a density increase matching the settlement. Measuring the full snow sample will require more measuring time, which leads to the loss of more distance measurements. But since the snow height decreased monotonously less distance data are required.

The calculated compactive viscosity for the isothermal experiment was in the range of the values for snow of a density around 230 $kg\,m^{-3}$ given in Shapiro et al. [1997]. In the temperature-gradient experiment both the strain and compactive viscosity increased about twice as fast compared to isothermal conditions. We can exclude that the top part of the Snowbreeder was frozen. After both experiments we could lift up the top part of the Snowbreeder. Hence, the weight on top of the snow sample moved freely during the experiments. We can also exclude a strong effect of different snow temperatures in both experiments, because the homologous temperature differed only by 0.6% between both experiments. Additionally, based on the temperature difference, the isothermal sample should have settled slower than the temperature-gradient sample. We hypothesize that temperature-gradient metamorphism influences settlement by increasing the compactive viscosity. Further experiments with the Snowbreeder 5 will shed light on the reasons for the strain-evolution dependence on the temperature gradient in the snow.

Chapter 4

Early-stage interaction between settlement and temperature-gradient metamorphism

Abstract

Snow metamorphism and settlement change the microstructure of a snowpack simultaneously. Past experiments investigated snow deformation under isothermal conditions. In nature, temperature gradient metamorphism and settlement often occur together. We investigated snow settlement in the first days after the onset of temperature-gradient metamorphism in laboratory experiments by means of in-situ time-lapse micro-computed tomography (micro-CT). We imposed temperature gradients of up to 95 K m^{-1} on samples of rounded snow with a density of around 230 kg m^{-3} and induced settlement by applying 1.7 kPa stress with a passive load on the samples simultaneously. We found that snow settled about half as fast when a temperature gradient was present, compared to isothermal conditions. The change in specific surface area after four days caused by temperature-gradient metamorphism was only a few percent. The viscosity evolution correlated with the amount of the temperature gradient. Finite element simulations of the

snow samples revealed that stress-bearing chains had developed in the snow structure, causing the large increase in viscosity. We could show that a small change in microstructure caused a large change in the mechanical properties. This explains the difficulty of predicting snow mechanical properties in applications such as firn compaction or snow avalanche formation.

4.1 Introduction

As soon as snow reaches the ground, its morphology changes quickly by snow metamorphism and deforms due to the overburden stress. Snow metamorphism and deformation is crucial to understand other processes, such as avalanche formation [Schweizer et al., 2003], firn formation on ice sheets [Fujita et al., 2016], and the effect on wildlife [Bokhorst et al., 2016]. Metamorphism can lead to the formation of weak layers due to depth-hoar development [Pinzer et al., 2012], or the formation of a well-sintered rounded structure [Kaempfer and Schneebeli, 2007]. Deformation can lead to densification and stabilization of a snowpack or local stress concentrations [Scapozza and Bartelt, 2003a] in a snowpack.

Snow deforms as a non-linear viscoelastic material [Scapozza and Bartelt, 2003b], for which constitutive laws similar to polycrystalline ice and viscous fluids were formulated based on field and laboratory measurements [Shapiro et al., 1997]. With these experimental laws, snow settlement can be described as a creep process. Creep is differentiated between primary, secondary and tertiary creep. Initially, snow densifies rapidly and non-stationary during primary creep, followed by a slower stationary densification during secondary creep [Sturm and Benson, 1997]. For primary creep in snow, Glen's flow law for polycrystalline ice can be simplified as the following power law, relating the strain rate $\dot{\epsilon}$ of snow and the constant uniaxial stress σ linearly by the viscosity η, similar to a viscous fluid [Schleef and Löwe, 2013]:

$$\dot{\epsilon} = \frac{\sigma}{\eta} \tag{4.1}$$

The viscosity η depends on snow density, temperature and strain rate with higher values for higher densities, lower temperatures and lower strain rates [Scapozza and Bartelt, 2003b]. However, considering only the density to describe the structure of snow and its viscoelastic properties showed to be insufficient. Different grain and bond characteristics can lead to larger differences in snow compaction than different loads and load histories [Sturm and Holmgren, 1998]. Several field observations confirm large differences in viscosity between different snow types at equal density, as rounded well-sintered snow

settles faster than depth hoar (Kojima [1967], Armstrong [1980], Shapiro et al. [1997], Sturm and Benson [1997], Sturm and Holmgren [1998]). There is clear evidence from the field that the snow microstructure affects viscosity, but experimental data under controlled conditions are lacking, making modeling difficult.

In a natural snowpack, snow metamorphism occurs simultaneously with deformation. Dry snow metamorphism results from vapour transport within the snow structure under isothermal conditions or a temperature gradient. While a rounded snow structure evolves under isothermal conditions, a temperature gradient leads to a different evolution of the snow morphology, i.e. faceting and depth hoar (Pinzer et al. [2012], Calonne et al. [2014]).

Although temperature-gradient metamorphism is almost always present in a snowpack, most laboratory experiments on snow deformation were conducted under isothermal conditions at different temperatures and stresses, and mainly with rounded snow (e.g. Scapozza and Bartelt [2003b], Scapozza and Bartelt [2003a], Theile et al. [2011], Schleef and Löwe [2013], Schleef et al. [2014b], Schleef et al. [2014c]). Likewise, experiments on temperature-gradient metamorphism were conducted (Pinzer et al. [2012], Calonne et al. [2014], Wiese and Schneebeli [2017c], Wang and Baker [2016]), but without considering settlement occurring simultaneously as in a natural snowpack. The only exception is the laboratory experiment by De Quervain [1958], where the snow structure was observed at the start and end of the experiment. Recently, Wiese and Schneebeli [2017b] developed the Snowbreeder 5 for time-lapse micro-computed (micro-CT) experiments on the effect of structural snow changes due to snow metamorphism on settlement. With this device a constant temperature gradient can be imposed on a snow sample placed in a micro-CT and simultaneous settlement can be induced. In contrast to the experiments of De Quervain [1958] the micro-CT measurements allow for a continuous observation of the snow structure. First results of Wiese and Schneebeli [2017b] show a decreased settlement under temperature-gradient conditions compared to isothermal conditions. This study extends previous isothermal settlement experiments with settlement experiments under the influence of a constant temperature gradient. The settlement experiments were built up such that the microstructural changes involved could be measured simultaneously by micro-computed time-lapse tomography with the Snowbreeder 5. We aimed to investigate how the viscosity evolves during the first days of transition from rounded snow towards depth hoar and which microstructural properties are relevant to the process.

4.2 Methods

We used the instrumented sample holder Snowbreeder 5 [Wiese and Schneebeli, 2017b] to investigate the interaction of settlement and temperature-gradient metamorphism in the first days after onset of metamorphism.

4.2.1 Experimental design

We considered the following factors as relevant in our experiments: isothermal conditions, temperature gradients, temperature, wall effects by friction and imposed stress. We did not test all interactions between these factors, but the ones where we expected an interaction (Table 4.1). The initial snow properties were kept constant as much as possible.

Table 4.1: *Interactions between the investigated factors: isothermal conditions ISO, effective temperature gradient in the snow sample TG, temperature T, wall effect $wall$, imposed stress σ. X: investigations were done between factors, -: no investigations were done.*

	ISO	TG	T	$wall$	σ
ISO	O	X	-	X	-
TG	X	X	X	X	X
T	-	X	O	-	X
$wall$	X	X	-	O	-
σ	-	X	X	-	O

As a reference, where the effect of metamorphism on settlement is negligible, experiments under isothermal conditions were performed, which can be compared well to other laboratory experiments. The sample being confined or unconfined is the only other factor investigated in these experiments, i.e. confined touching the wall of the sample holder, and unconfined, i.e. the sample was slightly thinner than the sample holder. The low value of the Poisson number of highly porous media [Shapiro et al., 1997] leads to a small effect of confinement in compression experiments. This is certainly true for compression experiments under isothermal conditions, but is less clear if this is also the case during temperature gradient metamorphism. Therefore, we checked the wall effect also for the temperature-gradient experiments.

The main interest was in the effect of a temperature gradient and the hereby initiated

metamorphism and structural change on densification. We applied various temperature gradients at different imposed stresses and three different temperature ranges (around -14, -9, and -4°C). One question was the variation of the ice viscosity vs. the rate of recrystallization determined by the water-vapour flux at different temperatures. To discriminate whether there is an interaction between settlement and temperature-gradient metamorphism, we conducted experiments with and without additionally imposed stress at different temperatures.

In summary, the thirteen successful experiments cover the factors explained above.

4.2.2 Snow properties and instrumentation

As a starting material we used nature-identical snow produced with the Snowmaker [Schleef et al., 2014a], which cannot be distinguished structurally from natural snow. We sieved the snow through a sieve with a mesh size of 5 mm into styrofoam boxes. The snow was then stored in these boxes at constant temperatures between -5°C and -20°C for several months, such that the snow sintered and developed a rounded structure through isothermal metamorphism. Thus, structural change was small between experiments. This snow had a density between 211 and 261 $kg\,m^{-3}$ and a specific surface area SSA between 12.3 and 13.3 m^2kg^{-3}. The calculation of the snow density and SSA from micro-CT images is explained further below in this section. Starting experiments from this rounded snow structure enabled us to observe faceting during the experiments. Cylindrical snow samples were cut out vertically from the snow in the styrofoam boxes for the experiments.

The Snowbreeder 5 [Wiese and Schneebeli, 2017b] imposes a constant temperature gradient on a snow sample and simultaneously induces settlement while measuring the snow microstructure in the Micro-CT (Fig. 4.1). The temperature at the bottom is controlled with a Peltier element; and the top of the snow sample by controlling the temperature inside the Micro-CT. A passive load is placed on top of the snow sample, which induces settlement and serves also as a passive heater or cooler. The temperature at the top of the snow sample is measured at the bottom of the weight. In addition to no external loading (0 Pa) the applied stress can be varied between 658 Pa and 1736 Pa. The settlement is measured by a laser distance sensor mounted at the stable bottom part towards the upper rim of the weight as it moves downwards. The Snowbreeder rotates 360° horizontally during a micro-CT measurement. Due to this rotation the settlement measurements show larger fluctuations during micro-CT measurements. Hence, these data were excluded for the analyses.

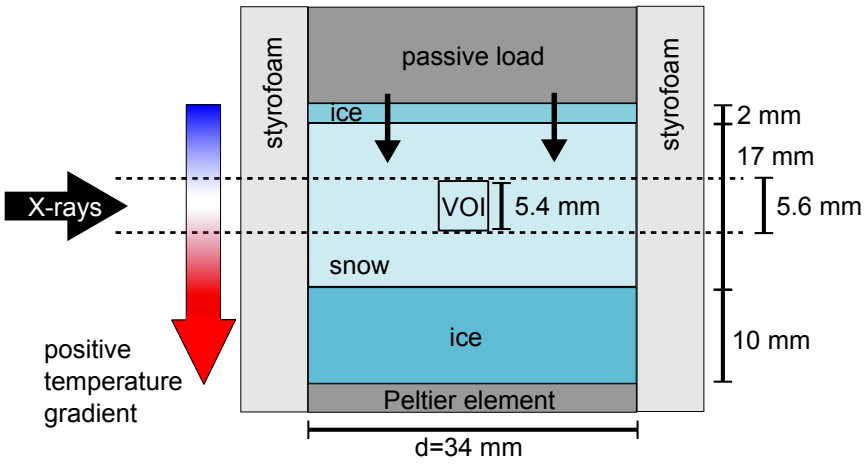

Figure 4.1: *Setup and dimensions of the Snowbreeder 5 experiments. VOI is the volume of interest for the image analysis. A positive temperature gradient is defined by the bottom temperature higher than the top temperature.*

The sample diameter was given by the inner diameter of the Snowbreeder, which is 34 mm. To minimize wall effects during settlement the snow-sample height was 17 mm to reach the recommended diameter-to-height ratio of 2 [ASTM, 2011]. Since the measuring distance of the laser is restricted to 23 to 33 mm, we inserted a 10 mm thick ice layer at the bottom to raise the snow sample within the sample holder. This ice layer also serves as a water-vapour supply in the case of a positive temperature gradient, when the temperature at the bottom was higher than the temperature at the top of the snow sample. In experiments with a negative temperature gradient, we inserted an additional 2 mm thick ice layer between the snow sample and the passive load as water-vapour source. We lubricated the passive load with a thin film of silicone grease so that it did not freeze to the wall due to the depositing water vapour. No ice deposition was observed on the moving elements of the sample holder after the experiment.

In most of the experiments we applied the maximum stress, i.e. 1736 Pa, on the snow sample. This corresponds to 0.7 to 0.8 m snow lying on the sample with a density used in the experiment. To compare the structural snow evolution under stress and without stress, we fixed the load in the Snowbreeder in some experiments so that no external stress was applied to the snow sample. Wiese and Schneebeli [2017b] estimated the stress of the snow's own weight in a sample of the same dimensions and density as in these experiments to be 2% of the imposed maximum stress of 1736 Pa, which they considered to be negligible. We did two experiments with snow samples with a diameter of 28 mm, in order to have certain unconfined conditions, to compare with experiments where the samples had a diameter as large as the inner diameter of the Snowbreeder. For the samples with a smaller diameter we adjusted the weight of the passive load such that

Table 4.2: *Overview of the experiments. Exp.: experiment number, d: sample diameter, m: weight of the passive load, σ: vertical stress, TG: temperature gradient, T_s: mean snow temperature, ρ_s: initial snow-sample density measured in the laboratory, $\rho_{s,i}$: initial snow density calculated from micro-CT images, SSA_i: initial specific surface area.*

Exp.	d (mm)	m (g)	σ (Pa)	TG (K m^{-1})	T_s (°C)	ρ_s (kg m^{-3})	$\rho_{s,i}$ (kg m^{-3})	SSA_i (m^2 kg^{-3})
1	34	161	1736	-59	-12	265	216	13.2
2	34	161	1736	43	-9	225	224	13.3
3	34	161	1736	0	-10.3	187	235	13.3
4	28	110	1752	0	-10.3	293	234	13.2
5	28	110	1752	45	-9	309	211	13.2
6	34	0	0	47	-9.1	249	249	13.1
7	34	161	1736	69	-8.3	282	223	13.2
8	34	161	1736	95	-7.5	329	244	12.7
9	34	161	1736	31	-9.4	249	229	12.9
10	34	161	1736	49	-4.1	243	215	13.2
11	34	161	1736	47	-13.7	289	261	12.3
12	34	161	1736	50	-4.1	267	236	12.7
13	34	0	0	51	-4.1	267	239	12.7

the applied stress was very close to the other experiments. Table 4.2 gives an overview of the applied stresses and sample diameters.

We calculated the strain ϵ from the measured laser distance d_l, the initial laser distance $d_{l,0}$ and the height L of the sample as follows:

$$\epsilon = \frac{d_{l,0} - d_l}{L} \tag{4.2}$$

We imposed various temperature gradients on the snow sample by changing the temperature of the Peltier element and the air temperature inside the Micro-CT. For isothermal experiments we turned off the Peltier element and controlled the snow temperature only via the air temperature inside the Micro-CT. Since we inserted a 10 mm high ice layer at the bottom between the Peltier element and the snow sample, the temperature at the bottom of the snow sample was different compared to the temperature at the Peltier element. We estimated the temperature T_{int} at the interface of the snow sample and the ice layer from the heat conduction through a composite sample. Thus, we could obtain the effective temperature gradient in the snow sample and in the ice layer below. At the interface the heat flux q is continuous:

$$q_s = q_i \tag{4.3}$$

$$-k_s \frac{T_{top} - T_{int}}{z_{top} - z_{int}} = -k_i \frac{T_{int} - T_{bot}}{z_{int} - z_{bot}} \tag{4.4}$$

From Equation 4.4 we calculated the temperature at the interface T_{int} as follows:

$$T_{int} = \frac{\frac{k_i}{z_{int}-z_{bot}} T_{bot} + \frac{k_s}{z_{top}-z_{int}} T_{top}}{\frac{k_s}{z_{top}-z_{int}} + \frac{k_i}{z_{int}-z_{bot}}} \tag{4.5}$$

q_s and q_i are the heat fluxes in the snow and ice, respectively. T_{top} and T_{bot} are the temperatures measured at the top z_{top} and bottom z_{bot} of the Snowbreeder. z_{int} is the height of the interface between the snow sample and the ice layer below. $k_i = 2.2\,\mathrm{W\,m^{-1}\,K^{-1}}$ is the heat conductivity of ice. For the heat conductivity of snow k_s we took the value for the vertical heat conductivity of rounded snow with densities of our experiments, which is approximately $k_s = 0.17\,\mathrm{W\,m^{-1}\,K^{-1}}$ [Riche and Schneebeli, 2013]. The effective constant temperature gradients in the snow sample were between 0 and 95 $\mathrm{K\,m^{-1}}$. The mean snow temperature varied between -4.1°C and -13.7°C.

The snow samples were scanned periodically in the Micro-CT to analyse the microstructural snow evolution. We chose the settings for the micro-CT measurements such that the duration of one measurement was as short as possible to reduce the times when distance measurements were disturbed during the scans. The peak energy and the current of the X-ray tube was set to be 45 kVp and 88 μA, the integration time was 300 ms and the voxel size was 36 μm. We scanned a height of 5.6 mm in the middle of the snow sample. With these settings one measurement took 50 minutes. We took one micro-CT measurement every eight hours. The exact height position of the Snowbreeder in the Micro-CT was measured with a linear encoder ($\pm$1 nm) such that the scans could be precisely aligned between measurements.

At the beginning and end of each experiment we took close-up images of snow grains with a Olympus camera (model: E-510, resolution: 4μm). In contrast to the 3D images obtained with the Micro-CT, the close-up images show only single snow grains and not the full snow structure with bonds between snow grains. However, these pictures allow an easy classification into snow types.

4.2.3 Image processing and numerical simulations

To analyse the 3D images obtained with the Micro-CT, we defined a cubic volume of interest in the images, matching a representative volume of snow. The side length of the volume was 5.4 mm. We applied a Gauss filter with a sigma of 1 and a support of 2 voxels on the greyscale images. Then, we segmented the image into ice and air

voxels, based on the histogram of greyscale values in the volume of interest. We used the same threshold for the segmentation for all images of one experiment. The resulting segmented 3D images were merged to create time-lapse movies, which are included in the online supplementary material.

From the segmented 3D images we calculated structural snow parameters, i.e. density, specific surface area SSA and pore size, by triangulation of the ice surface using IPL (Image Processing Language, developed by Scanco Medical AG). This algorithm was also used by Kerbrat et al. [2008] and Matzl and Schneebeli [2010] to determine structural parameters of snow. The SSA is defined as the ratio of the ice surface area to the ice mass:

$$SSA = \frac{\text{ice surface area}}{\text{ice mass}} \tag{4.6}$$

In addition to the density calculated from the micro-CT images, we calculated the snow density from the weight and the dimensions of the snow sample in the beginning of the experiments.

We calculated additionally the structural anisotropy a of the snow structure from the normalized chord lengths, i.e. the length between intersections of air and ice in the segmented 3D image [Good, 1987]. Details on the calculations are given in Wiese and Schneebeli [2017c]. The structural anisotropy a is defined as the ratio of the vertical chord length l_z to the two mean horizontal chord lengths l_x and l_y:

$$a = \frac{l_z}{(l_x + l_y)/2} \tag{4.7}$$

We simulated the stress distributions in the snow microstructure as a first approximation by a purely elastic simulation in a voxel-based finite-element model in IPL [Van Rietbergen et al., 1995]. The isotropic elastic modulus of ice was taken as 9.6 GPa. By using this model, we were able to identify the change in stress distribution related to a change in the microstructure. The creep process in snow is also affected by the strong mechanical anisotropy of ice, and is not reproduced by this simple constitutive model. Prior to the simulations, all small unconnected parts in the segmented 3D images were deleted, since these parts are not stress-bearing and would cause errors in the simulations. In the finite-element model the microstructure in a 3D image is elastically deformed with a prescribed uniaxial strain in the vertical direction. From the simulations we calculated the Von-Mises equivalent stress in the snow structure and the elastic modulus. To analyse the distribution of the highest stresses in the snow structure we segmented the 3D images of the snow structure once again based on a stress threshold. We kept once 5% and once 30% of the snow structure, in which the highest stresses occurred. For the images with 5% ice mass we calculated the anisotropy (Eq. 4.7), which

we defined as mechanical anisotropy in contrast to the structural anisotropy of the entire snow structure.

4.3 Results

4.3.1 Observations

The strain of the snow samples increased monotonically in all experiments in which we induced settlement. In experiments with a constant temperature gradient the strain increase was slower compared to isothermal conditions, independent of the direction of the temperature gradient (Fig. 4.2 (a)). The strain increase was lower for a higher temperature gradient (Fig.4.2 (b)). This difference in strain increase between isothermal and temperature-gradient experiments occurred both in confined and unconfined experiments (Fig.4.2 (c)). Fig. 4.2 (d) shows that the strain increase was lower at a lower mean snow temperature. The strain increase at -13.7°C was half as strong as the strain increase at -4°C.

The initially rounded snow structure stayed rounded in the isothermal experiments and became faceted in the temperature-gradient experiments, in which small cup crystals formed (Fig. 4.3). The SSA decreased only slighty by around 5% and almost linearly in nearly all experiments (Fig. 4.4). This 5% change in SSA is at the limit of what can be measured with the Micro-CT. In Exp. 10 the SSA increased after a decrease for one day. In Experiment 3 and 4 the SSA increased from the beginning on, with a decrease after 1.5 days in Experiment 3. The highest SSA decrease occurred in the experiment with the highest temperature gradient (Exp. 8). In most of the experiments the snow density increased slightly (Fig. 4.5). In two experiments the density decreased first before a slight increase occurred (Exp. 1 and 4). In one of these experiments the temperature gradient was negative and in the other one settlement occurred under isothermal conditions. The initial snow structure was slightly horizontally anisotropic (Fig. 4.6). The structural anisotropy did hardly change during the experiments discussed in this subsection. In some experiments the anisotropy increased slightly and in other experiments the anisotropy decreased slightly.

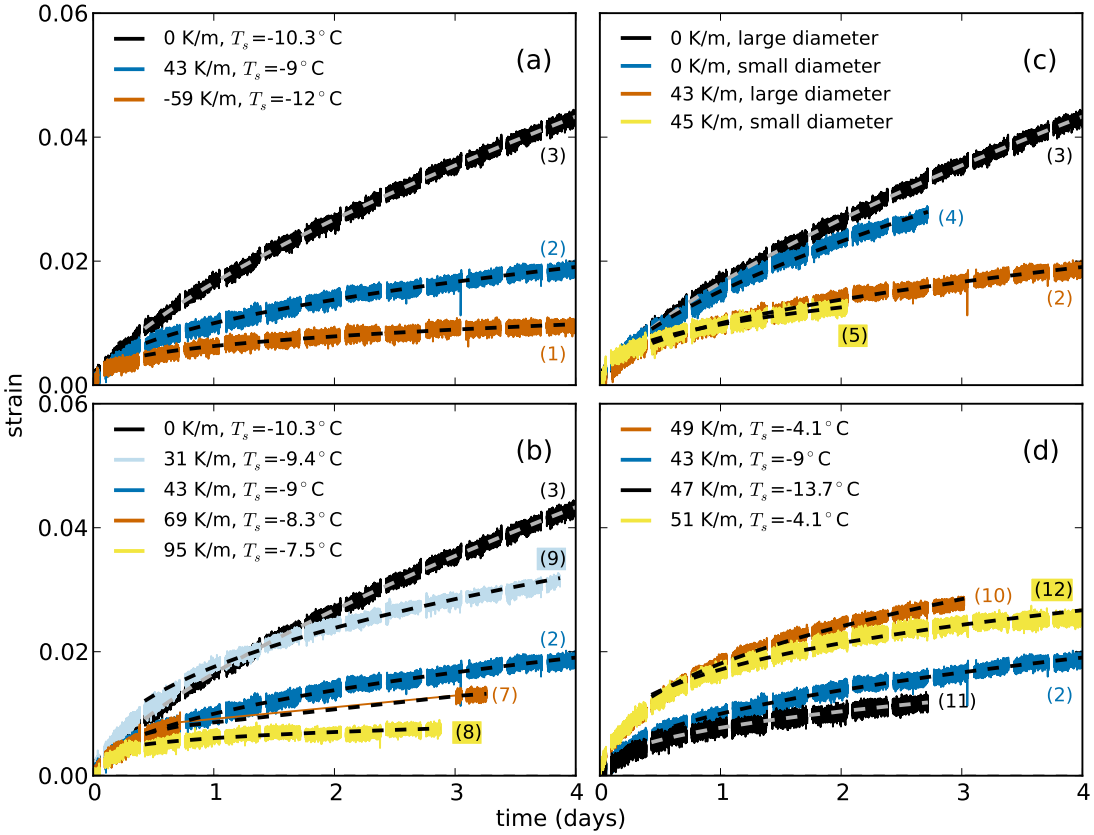

Figure 4.2: *Strain dependence on temperature gradient direction (a) and magnitude (b), sample diameter (c) and mean snow temperature (d). T_s: mean snow temperature. The coloured parenthesized numbers on the lines refer to the experiment numbers in Tab. 4.2. The grey and black dashed lines are fits according to the power law given in Equation 4.8. The exponents and prefactors of the power-law fits are given in Tab. 4.3.*

4.3.2 Viscosity

We divided the primary creep occurring in our experiments into a pre-primary (first ten hours) and primary creep (after ten hours), because the temporal strain evolution showed large variations from a straight line in a logarithmic plot during the first ten hours of the experiments. We fitted the evolution of the strain ϵ with time t during the primary creep to the following power law:

$$\epsilon = At^b \tag{4.8}$$

The values for the exponent b are between 0.28 and 0.7 (Tab. 4.3). The fitted strain evolution is shown as dashed grey and black lines in Figure 4.2.

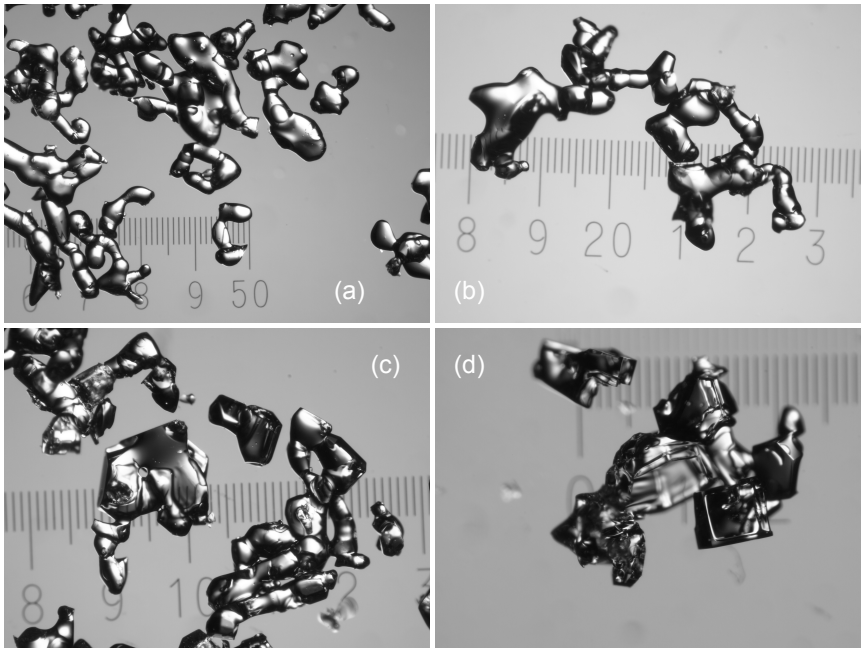

Figure 4.3: *Close-up images of snow grains before the experiments ((a), RGlr) and after three days under isothermal conditions ((b), RGlr and RGxf, Exp. 4), under a temperature gradient of 47 K m^{-1} ((c), FCso and RGxf, Exp. 10, mean snow temperature: -13.7°C) and under a temperature gradient of 49 K m^{-1} ((d), FCso and DHcp, Exp. 11, mean snow temperature: -4.1°C). The scale in the images is labelled in millimetres.*

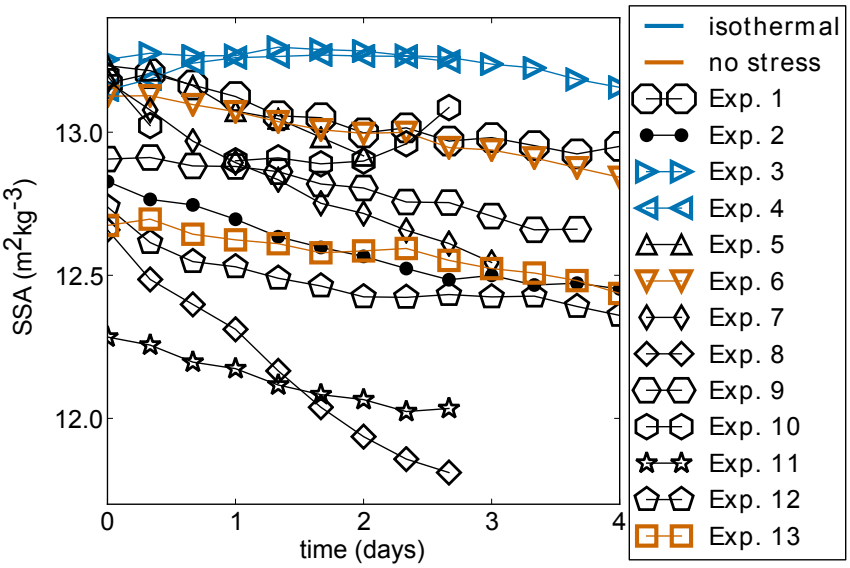

Figure 4.4: *Temporal evolution of the specific surface area SSA. Details about the experiments are summarized in Tab. 4.2.*

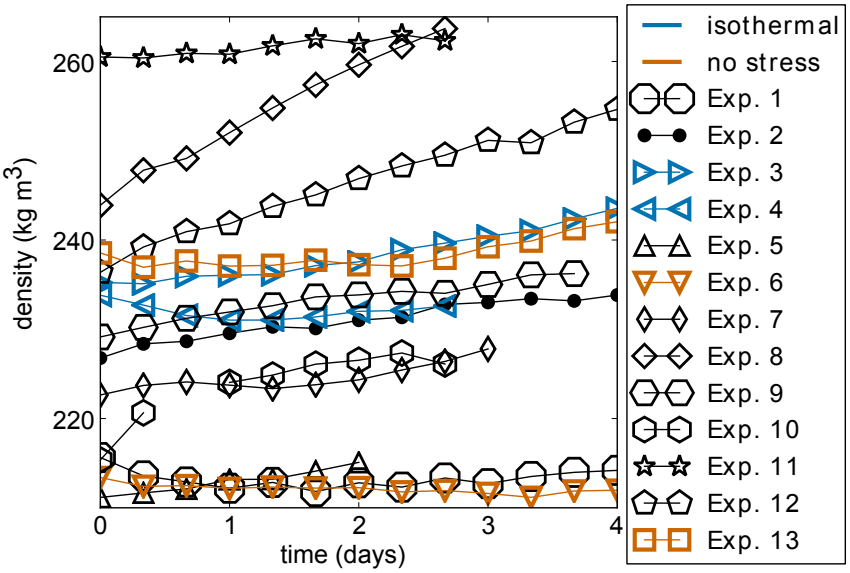

Figure 4.5: *Temporal evolution of the snow density. Details about the experiments are summarized in Tab. 4.2.*

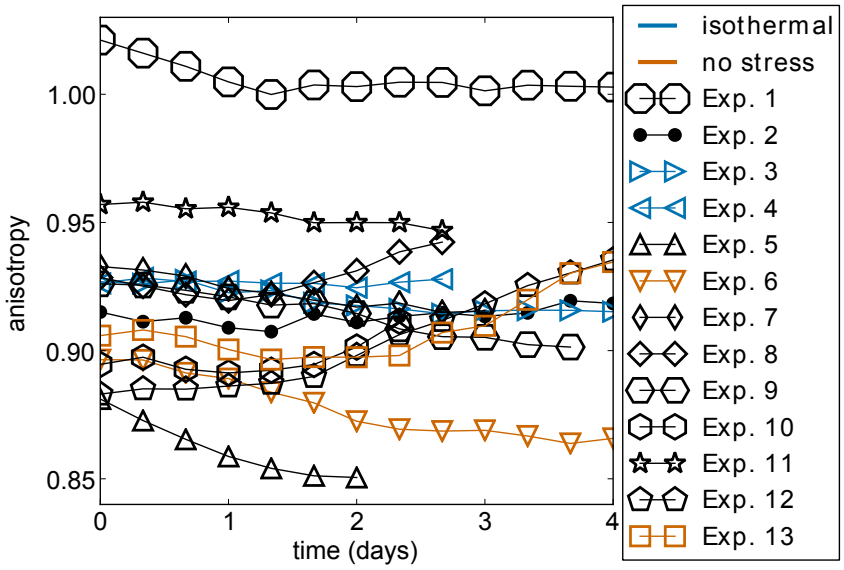

Figure 4.6: *Temporal evolution of the structural anisotropy. Details about the experiments are summarized in Tab. 4.2.*

Table 4.3: *Exponent b and prefactor A of the power-law fits of the temporal strain evolution (Eq. 4.8). Exp.: experiment number.*

Exp.	b	A
1	0.32	0.0063
2	0.47	0.01
3	0.7	0.0165
4	0.61	0.0152
5	0.36	0.0098
7	0.33	0.0089
8	0.22	0.0061
9	0.44	0.0175
10	0.41	0.0181
11	0.42	0.0077
12	0.32	0.0017

With this power-law fit, we summarized the influence of the temperature gradient and mean snow temperature on the measured strain increase (Fig. 4.7). The strain increase is represented as the exponent b of the power law (Eq. 4.8). The exponent b decreased linearly with an increasing temperature gradient TG:

$$b = 0.63 - 4.7 \cdot 10^{-3} TG \tag{4.9}$$

The correlation coefficient is -0.94 and the p-value is $1.2 \cdot 10^{-5}$. A lower b at higher temperature gradients shows again the slower strain increase at higher temperature gradients. There is no clear effect of the mean snow temperature visible. The experiment within the lowest temperature range shows a similar value for b as one of the two experiments within the highest temperature range at almost the same temperature gradient.

We calculated the temporal evolution of the compactive viscosity η from the relationship between the strain rate $\dot{\epsilon}$ and the applied stress σ (Eq. 4.1). For this, we calculated the strain rate from the exponential strain-increase fit (Eq. 4.8):

$$\eta = \frac{\sigma}{\dot{\epsilon}} = \frac{\sigma}{Abt^{b-1}} \tag{4.10}$$

The viscosity increased in the form of a power law in all experiments. In comparison to isothermal experiments the viscosity reached higher values in experiments with a temperature gradient, independent of the direction of the temperature gradient (Fig. 4.8 (a)). The viscosity was higher at higher imposed temperature gradients (Fig. 4.8 (b)). Additionally, the viscosity was slightly higher for lower mean snow temperatures (Fig. 4.8 (d)).

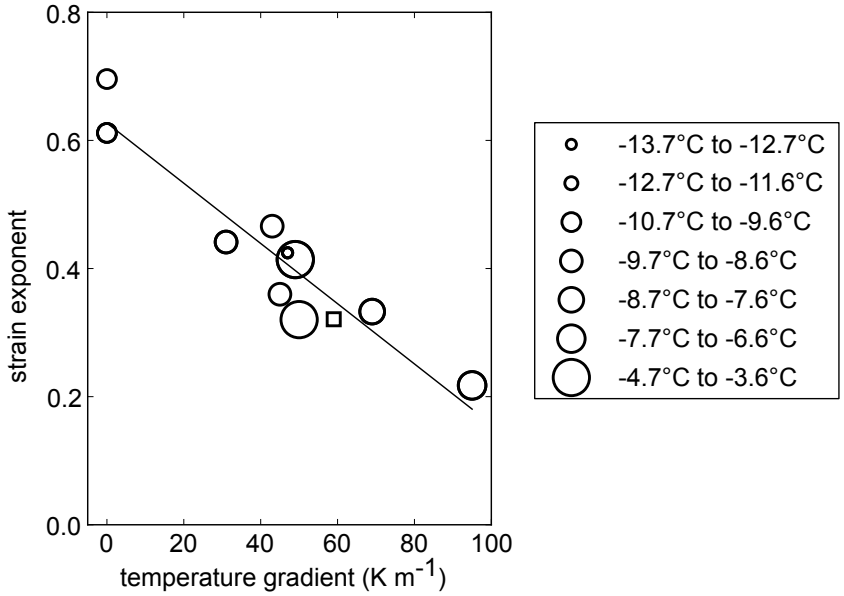

Figure 4.7: *Relationship between temperature gradient, mean snow temperature and temporal strain evolution given as the exponent of the power-law fit (Eq. 4.8, Tab. 4.3). Positive temperature gradients are depicted as circles and negative temperature gradients are depicted as squares. The black line is a linear fit given in Eq. 4.9.*

4.3.3 Simulations

The finite-element simulations show a stiffening of the snow structure. We did simulations for the beginning and end of two experiments as examples for the influence of isothermal conditions and temperature-gradient metamorphism (Exp. 2 and 3 in Tab. 4.2). After four days, the simulated elastic modulus of the snow structure increased by 28% in the temperature-gradient experiment and by 23% in the isothermal experiment. Adding up the stresses in the stress-segmented 3D images showed that in 30% of the ice mass 70.8% of the total stress occurred in the beginning of the temperature-gradient experiment. In the beginning of the isothermal experiment, the added up stresses in 30% of the ice mass comprised 71.9% of the added-up stresses occurring in the whole ice structure. Hence, the main part of the stress was born only by a small part of the ice structure. After four days 30% of the ice mass bore 72.4% and 70.5% of the stresses in the case of a temperature-gradient and isothermal conditions, respectively. The highest stresses were differently distributed in the beginning and at the end of the experiments. In the isothermal experiment the initial structure of 5% of the ice mass, which bore the highest stresses, was still visible and changed only little (Fig. 4.9). In the temperature-gradient experiment, vertical stress-bearing chains developed (Fig. 4.10). After four

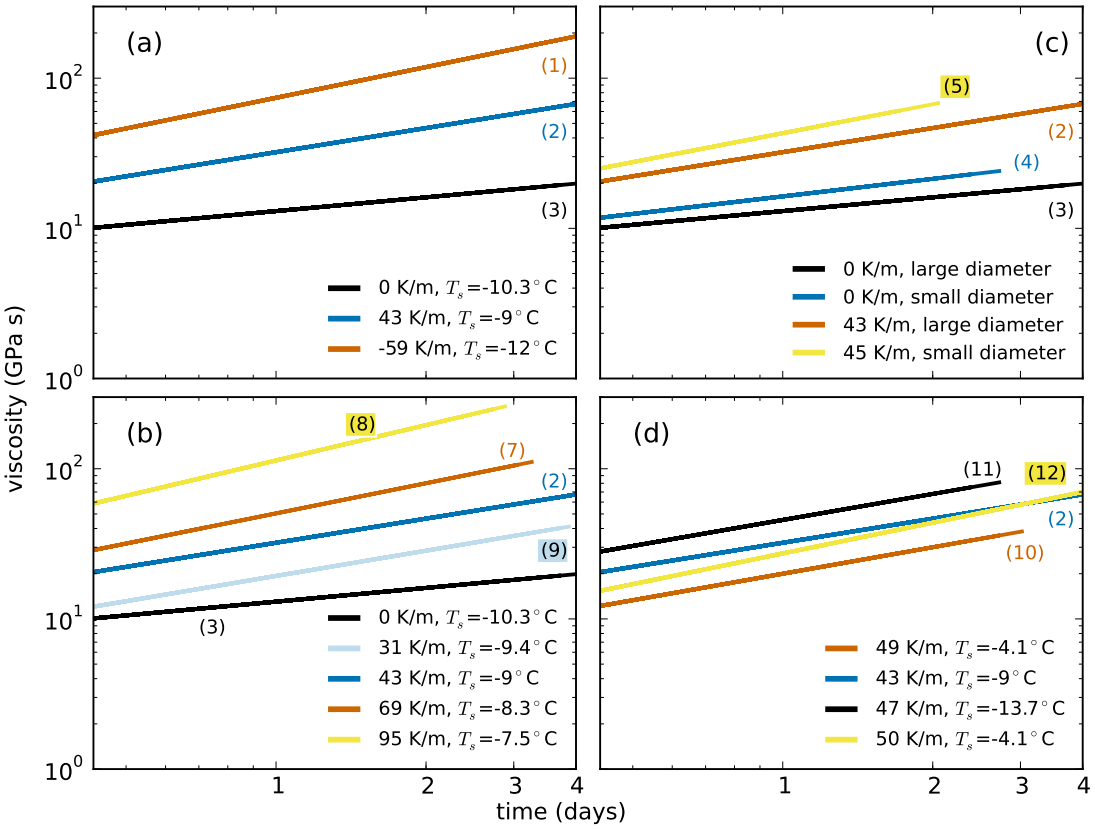

Figure 4.8: *Dependence of the compactive viscosity on temperature-gradient direction (a) and magnitude (b), sample diameter (c) and mean snow temperature (d). T_s: mean snow temperature. The coloured parenthesized numbers on the lines are the experiment numbers in Tab. 4.2.*

days the mechanical anisotropy increased, while the structural anisotropy showed only little evolution in both experiments. The structural anisotropy increased by 0.4% in the temperature-gradient experiment and decreased by 1.3% in the isothermal experiment. The mechanical anisotropy increased by 8.1% and 3.8% in the temperature-gradient experiment and in the isothermal experiment, respectively.

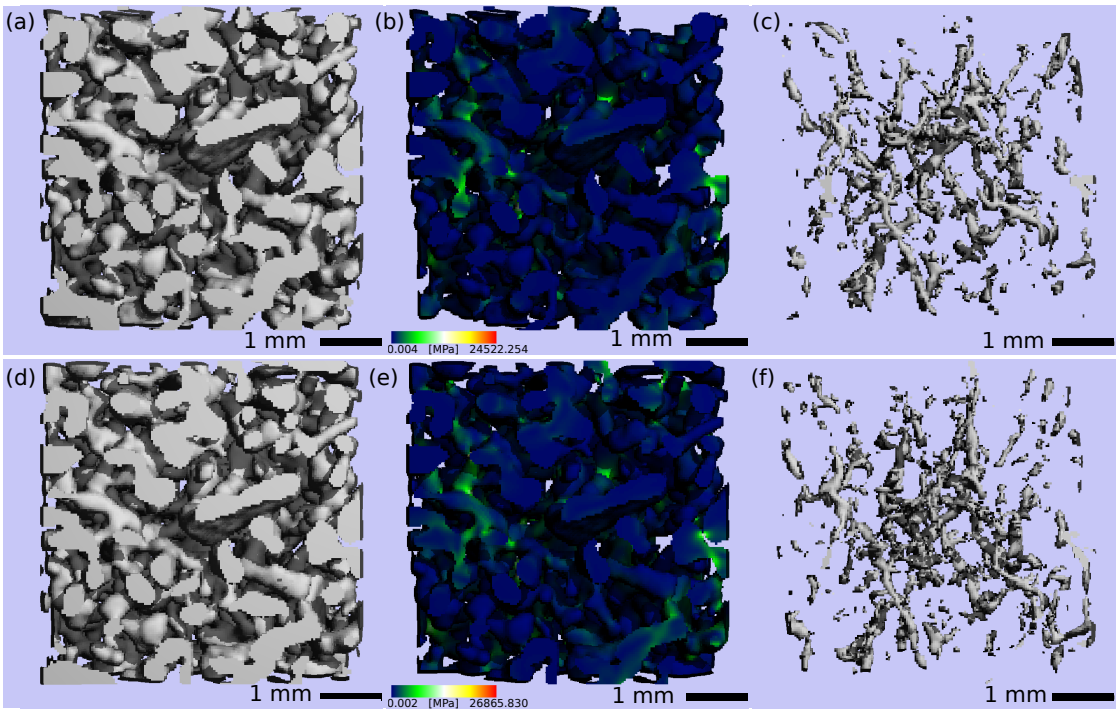

Figure 4.9: *Initial snow structure (a) in the CT images of an isothermal settlement experiment (Exp. 3 in Tab. 4.2) and the snow structure after four days (d). (b) and (e) show stresses in the snow structure caused by elastic deformation in the finite-element simulation described in Section 4.2.3. (c) and (f) show 5% of the structure, in which the highest stresses occurred in the beginning of the experiment and after four days, respectively.*

4.4 Discussion

We measured a distinct reduction in snow settlement caused by temperature-gradient metamorphism in the first days after onset of metamorphism. The settlement induced by the passive load caused a strain increase in the snow samples. Simultaneous temperature-gradient metamorphism led to a slower strain increase than during isothermal conditions. We expected that a vapour flux in the opposite direction of the settlement could counteract the settlement and lead to a decreased strain increase. This would be the case for a positive temperature gradient, i.e. in the direction of the settlement. However, the strain slowed down both when the mass flux was in the direction of the settlement and when the mass flux was in the opposite direction. Hence, the vapour flux within the snow cannot explain the decreased settlement under a temperature gradient compared to isothermal conditions. We can also exclude an effect of the walls of the Snowbreeder

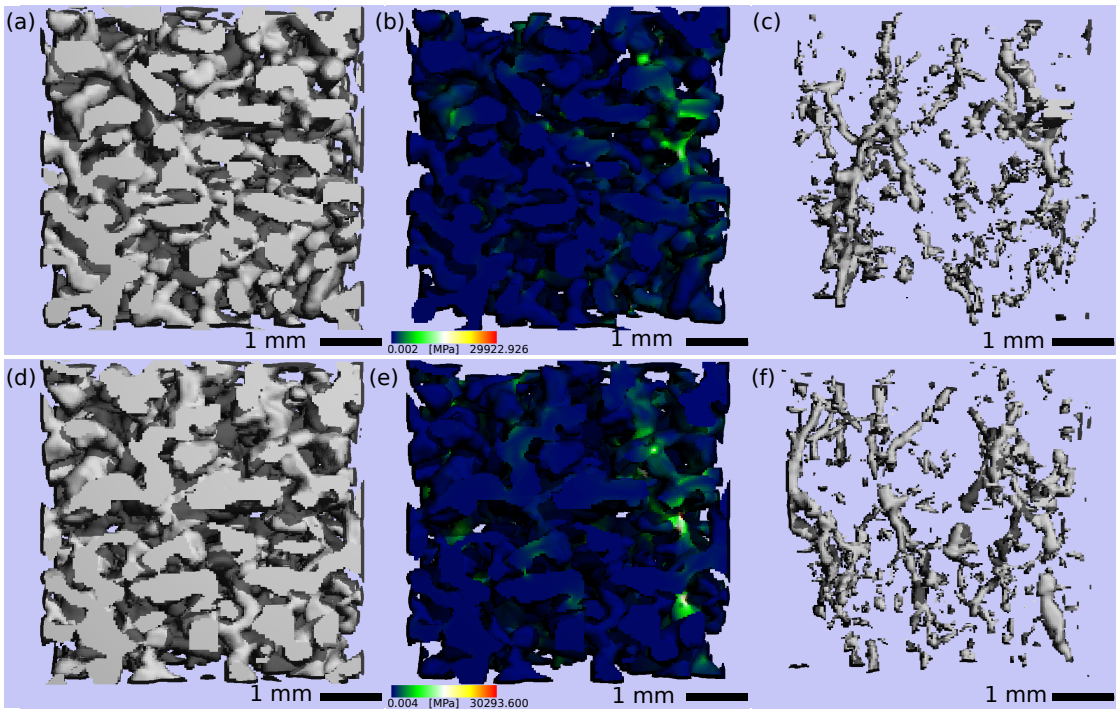

Figure 4.10: *Initial snow structure (a) in the CT images of a settlement experiment with a constant temperature gradient (Exp. 2 in Tab. 4.2) and the snow structure after four days (c). (b) and (e) show stresses in the snow structure caused by elastic deformation in the finite-element simulation described in Section 4.2.3. (c) and (f) show 5% of the structure, in which the highest stresses occurred in the beginning of the experiment and after four days, respectively.*

on the settlement, independent of isothermal and temperature-gradient conditions. The presence of a temperature gradient and a lower mean snow temperature are two factors that decrease settlement. The snow temperature affects both temperature-gradient metamorphism and deformation. Both the recrystallization rate during metamorphism and the plastic flow increase exponentially with temperature (Bucher [1956], Scapozza and Bartelt [2003a]). We can exclude a parallel effect of temperature gradient and snow temperature on settlement in our experiments, because we analysed settlement at different temperature gradients with similar temperatures and vice versa. In addition to the snow temperature, other factors, like the fabric of the snow, i.e. the distribution of the c-axis orientation of the ice crystals in snow, influence both settlement and metamorphism, which we did not measure. However, the fabric evolves only slowly over weeks during temperature-gradient metamorphism [Riche et al., 2013] and did thus most probably not affect settlement during our four day long experiments. In the experiments without external stress we did not observe any compaction.

The experiments showed that temperature-gradient metamorphism affects settlement immediately after the onset of metamorphism and not just after a typical depth-hoar structure developed as suggested by field observations (Kojima [1967], Armstrong [1980], Shapiro et al. [1997], Sturm and Benson [1997], Sturm and Holmgren [1998]). The transition from a rounded to the onset of a faceted structure is indicated by a slight SSA decrease and slight faceting without a fully evolved depth-hoar structure visible in the images. The SSA decrease resulted from a slight coarsening of the snow structure due to metamorphism. However, only Experiment 8 showed a clear SSA decrease larger than the measurement limit of the Micro-CT, because of the strong imposed temperature gradient. We did not observe a clear influence of the settlement on the SSA evolution, similar to measurements of new-snow settlement from Schleef and Löwe [2013]. The SSA increases measured in some experiments were probably caused by the settlement, which led to a movement of different parts of the snow structure into the VOI. However, the SSA variations are at the limit of what can be measured with the Micro-CT. Even though the density increased slightly in most of the experiments, the density increase did not match the compaction caused by the macroscopic strain. In one experiment without stress the density increased slightly and in two experiments with stress the density decreased first before a slight increase occurred (Exp. 1 and 4). The isothermal experiments (Exp. 3 and 4) did not show the highest densification, even though the strain increase was strongest in these experiments. We measured the largest density increase for the experiment with the highest temperature gradient and least strain increase (Exp. 8). A possible reason are local compaction bands propagating through the snow, as observed by Barraclough et al. [2016]. Our volume of interest could probably resolve single compaction bands, but was too small to measure the overall densification of the snow sample. Inhomogeneous recrystallization as well as initial vertical density variations might also play a role in the observed density evolution. The structural anisotropy did barely evolve and was not significantly different between isothermal settlement and settlement under a temperature gradient. Hence, the evolution of the structural anisotropy can also not explain the decreased settlement under a temperature gradient compared to isothermal conditions. Initially, we expected that the snow structure develops faster a vertical anisotropy in the case of a temperature gradient, which stabilizes the snow, in contrast to an isotropic structure under isothermal conditions.

According to the measured non-stationary strain rates the snow samples showed primary creep, which we fitted to a power law. Our experiments show that the exponent b is not constant for a certain density, but depends also on the history of the snow. Only the Experiments 1, 7 and 12 showed Andrade creep with an exponent of or close to 1/3, which occurs usually in polycrystalline ice and dense polycrystalline snow. In the other experiments the exponent was higher, except for one experiment, in which the exponent was lower. Our isothermal experiments can be best compared to literature values. We

found them close to the values of Theile et al. [2011] and Schleef and Löwe [2013], even though the density was lower in the new-snow experiments of Schleef and Löwe [2013]. Our experiments with a temperature gradient showed that the change in the exponent b could be parametrized using the relationship given in Equation 4.9 and shown in Fig. 4.7. However, such a parametrization must be used within the range of snow microstructures investigated.

As the strain increased less in experiments with a temperature gradient in comparison to isothermal experiments, the viscosity reached higher values in those experiments with a temperature gradient. The viscosity values for isothermal conditions are comparable to values given in Shapiro et al. [1997]. However, the values given in Shapiro et al. [1997] are only valid for isothermal conditions. The higher compactive viscosity for snow subjected to a constant temperature gradient is not considered in Shapiro et al. [1997]. The temperature dependence of the viscosity reported by Bucher [1956] is also visible in our experiments, i.e the viscosity was higher at lower temperatures.

While the structural evolution was only small, the mechanical properties of the snow structure evolved much faster with a strong influence on settlement. Both in the isothermal and temperature-gradient experiment the elastic modulus increased, showing a stiffening of the snow structure due to settlement. We expected that the elastic modulus would increase more in the isothermal experiment due to the faster densification caused by the higher strain. However, the elastic modulus increased more in the experiment with constant temperature-gradient metamorphism, indicating a stronger stiffening of the snow structure in the case of a temperature gradient. Hence, the temperature-gradient snow structure could deform less than the isothermal snow structure after four days, which is consistent with our strain measurements. In the temperature-gradient experiment the small part of the snow structure bearing the main part of the stresses increased after four days. Since we used an elastic constitutive model, higher simulated stresses are equivalent to less strain in experiments with a constant applied stress. Hence, less strain could occur in the end of the temperature-gradient experiment, indicating again the stiffening of the snow structure and matching the measured slower strain increase in this experiment compared to isothermal conditions. Additionally, the snow structure developed a larger vertical mechanical anisotropy after onset of temperature-gradient metamorphism compared to isothermal conditions. Stress-bearing chains developed in the snow due to temperature-gradient metamorphism, as also observed similarly by Gubler [1978] and Schneebeli [2004]. These stress-bearing chains stiffen the snow structure much more than an isothermal snow structure, where no such chains developed. This chain formation was apparently independent of the temperature-gradient direction, as the settlement was slower both for a positive and a negative temperature gradient. Similar to the stress-bearing chains, Pinzer [2009] showed in simulations that

only 40% of the ice conducted 80% of the heat through the snow structure and that heat-flow paths developed under the influence of a constant temperature gradient. Our experiments show that the formation of stress bearing chains leads to a slower settlement in the case of a temperature-gradient compared to isothermal conditions. The formation of such chains increases with temperature gradient and the associated increase in vapour flux and metamorphism, as indicated by the linear relationship between the temperature gradient magnitude and the strain exponent.

4.5 Conclusions

With our laboratory experiments we showed that settlement is strongly affected by temperature-gradient metamorphism directly after onset of metamorphism. After four days, a barely measurable structural evolution due to temperature-gradient metamorphism had a large impact on the mechanical properties of snow. Stress-bearing chains developed, which caused a stronger stiffening of the snow structure in contrast to isothermal conditions. This is reflected in the compactive viscosity, which was larger under a temperature gradient than under isothermal conditions. Hence, snow with a similar structure can differ substantially in the mechanical properties. Thus, density and stress are not enough to estimate the settlement of a snowpack. Additionally, a good knowledge about the temperature history is necessary, since the memory of the snow structure evolves fast.

The mechanical properties of snow should be measured in detail under the influence of temperature-gradient metamorphism, to complement the values for isothermal conditions measured before. In current snowpack models, such as Snowpack and Crocus, the influence of the snow structure due to temperature-gradient metamorphism has to be taken into account in the parameterisations and constitutive equations, which relate stress to strain, to represent the mechanical snow properties reasonably. Good constitutive equations are for example necessary to calculate the stability of a snowpack to evaluate the risk of avalanches.

Since alternating temperature gradients occur rather often in a snowpack, the influence of alternating temperature gradient metamorphism on the mechanical properties of snow could be an interesting investigation. Possibly, settlement under such conditions is similar to isothermal settlement, when the alternating temperature gradient is symmetric, which leads to a rounded snow structure. An asymmetric alternating temperature gradient could cause a decreased settlement, since the metamorphism is closer to constant temperature-gradient metamorphism. However, both symmetric and asymmetric

temperature gradients lead to the development of a vertically asymmetric snow structure [Wiese and Schneebeli, 2017c], which could stabilize the snow structure after some time, leading to similar settlement rates in both cases.

Chapter 5

Snow metamorphism at the soil-snow interface

Abstract

The snowpack structure close to the ground influences infiltration and the heat flux into and out of the soil. Additionally, it has a strong impact on wildlife, because some animals rely on low-density snow close to the ground to move within the snow and search for food. Even though the snowpack structure evolves through snow metamorphism, this process is rarely investigated at the ground-snow interface. Few field observations report low-density snow layers close to the ground. In a cold laboratory we conducted some of the first systematic observations on temperature-gradient snow metamorphism at the soil-snow interface based on time-lapse micro-computed tomography experiments. We imposed a temperature gradient of up to $100\,\mathrm{K\,m^{-1}}$ on a sample composed of rounded snow and a soil-analogue made of an ice-saturated layer of glass beads. After four days we measured the formation of a 2 to 3 mm layer of low-density snow above the soil interface. Simultaneously, we observed a drying of the soil due to a constant vapor flux from the soil to the snow. We observed a very similar snow-density decrease at the interface of an ice lens and snow, which showed that the primary reason for the density decrease

was a smaller available surface area for sublimation than for deposition. The drying of the soil had an additional small contribution to the density decrease in the snow above the soil. Temperature simulations show the development of a strong temperature gradient above the ice lens towards the end of the experiment due to the formation of the low-density snow layer.

5.1 Introduction

The snowpack structure at the soil-snow interface affects the infiltration of the soil below and the heat flux into and out of the soil. Besides these snow-soil transport processes, the snow structure close to the ground can have an effect on avalanche formation and has a strong impact on Arctic wildlife. Rodents, their predators and other animals, e.g. reindeers, move in the snow in search of food [Callaghan et al., 2011]. For example lemmings need a layer of low-density snow at the base of the snowpack to move in an energy-saving way within the snow to find food [Domine et al., 2016].

The structure of a snowpack evolves due to snow metamorphism. The recrystallization is caused by water-vapor transport within the snowpack. Snow metamorphism was investigated extensively and is well understood within the snowpack for isothermal, constant temperature-gradient and alternating temperature-gradient conditions (e.g. Kaempfer and Schneebeli [2007], Pinzer et al. [2012], Calonne et al. [2014], Wiese and Schneebeli [2017c]). For example depth-hoar formation is caused by strong temperature gradients. However, snow metamorphism at the soil-snow interface and the interaction between soil and snow was so far barely investigated.

Bader et al. [1939] made some of the first observations on the snow structure at the ground-snow interface. They found a formation of hard snow viaducts within a layer of low-density depth hoar on the ground close to a fracture zone of an avalanche. The hard pillars built up on elevations of rough ground. Bader et al. [1939] hypothesized that these viaducts were formed by snow hardening inside the depth-hoar layer due to the pressure of the snow layers above. Sturm and Benson [1997] also observed the formation of a weak layer in a snowpack close to the ground. Domine et al. [2016] observed gaps within a low-density depth-hoar layer at the base of a snowpack. Some of these gaps were tunnels digged by lemmings moving within the snow. Other gaps resulted from a partly collapse of the weak depth-hoar layer. The low-density depth-hoar layer formed due to a strong upward vapor flux due to strong temperature gradients in the beginning of the winter. Domine et al. [2016] measured a drying of the uppermost

centimeters of the soil underneath the snow and presumed that this drying resulted from a vapor flux from the soil into the snow. Also Sokratov [1998] stated that temperature gradients across the soil-snow interface can lead to a mass flux from the ground to the soil. He assumed that this flux depends on the ice content and heterogeneity of the ground and on the snow morphology, and influences depth-hoar formation close to the ground.

With this study we aim to gain a better insight into the formation of low-density snow layers or even gaps within the snow close to the soil-snow interface. We conducted time-lapse micro-computed tomography experiments, in which we imposed a constant temperature gradient on a soil-snow sample, in which the soil was mimicked by an ice-saturated layer of glass beads. We hypothesize that gaps in the snow above the layer of glass beads might form by three different mechanisms. First, the vapor flux resulting from the temperature gradient across the interface leads to a drying of the glass-beads layer, decreasing or even stopping the vapor flux into the snow, under the assumption of a complete drying of the layer of glass beads. Second, different heat conductivities lead to different temperature gradients in the soil and the snow, resulting in varyingly strong vapor fluxes. A stronger temperature gradient within the snow could lead to a stronger vapor flux compared to within the soil, causing a net mass loss at the soil-snow interface. Third, after the uppermost part of the soil dried, the tortuosity of this part affects the vapor flux j_z from the soil into the snow induced by a vertical vapour-concentration gradient $\Delta c_e/\Delta z$, because the tortuosity τ decreases the diffusivity D_0 due to an increased path length for water molecules:

$$j_z = D_{eff}\frac{\Delta c_e}{\Delta z} = -\frac{\phi}{\tau}D_0\frac{\Delta c_e}{\Delta z} \tag{5.1}$$

ϕ is the porosity of the soil, which determines the cross-sectional area for the vapour flux. We compare the soil-experiments with an experiment in which a snow sample was placed on top of an ice lens instead of an ice-saturated layer of glass beads. In the case of the ice lens the layer below the snow sample is always ice-saturated, in contrast to the soil, and hence a tortuosity effect can be excluded. We discuss an effect of available ice surfaces for sublimation and deposition on the ice lens, in the soil and in the snow.

5.2 Methods

We conducted time-lapse micro-computed tomography (micro-CT) experiments in a cold laboratory to investigate snow metamorphism at the soil-snow interface. In total,

Table 5.1: *Overview of the experiments. Exp.: experiment number, t: experiment duration, TG: imposed temperature gradient, $\rho_{s,i}$: initial snow density above soil/ice-lens surface, SSA_i: initial specific surface area above soil/ice-lens surface, d: glass-beads diameter.*

Exp.	t (days)	TG (K m^{-1})	$\rho_{s,i}$ (kg m^{-3})	SSA_i (m^2 kg^{-3})	d (mm)
1	24	50	230	15.6	0.4-0.6
2	21	100	185	17.5	0.4-0.6
4	21	100	235	13.7	1-1.3
5	21.5	100	264	13.9	0.09-0.15
ice lens	21	100	210	15.4	-

we conducted five experiments with different soil types and different temperature gradients. In one of the experiments we replaced the soil with an ice lens to compare snow metamorphism above frozen soil and ice. The duration of the experiments was three weeks. Table 5.1 provides an overview of the experiments.

5.2.1 Sample properties and instrumentation

For the micro-CT experiments we used the Snowbreeder 4 from Scanco Medical [Wiese and Schneebeli, 2017b], an instrumented sample holder, that imposes a constant temperature gradient on a snow sample while measuring the snow microstructure in the Micro-CT. The temperatures on the top and bottom of the snow sample are controlled with Peltier elements. To reach a homogeneous temperature distribution within the snow sample, the sample holder consists of a thin aluminum cylinder, surrounded by a cylinder of microporous foam. The foam thermally insulates the snow sample from the surrounding air and the aluminum cylinder imposes a uniform vertical temperature gradient. The 34 mm inner diameter of the Snowbreeder determined the sample diameter. We placed a 15 mm high snow sample on top of a 5 mm high frozen soil sample inside the Snowbreeder. We applied a constant temperature gradient of 50 to 100 K m^{-1} to the total sample composed of soil and snow, with a higher temperature at the bottom and a lower temperature at the top. In all experiments the mean temperature of the total sample was about -3°C and the air temperature inside the computer tomograph was between -11 and -16°C.

As soil sample we took monodisperse glass beads (soda-lime glass, density: 2500 kg m^{-3}) of three different diameters between 0.09 and 1.3 mm (Tab. 5.1) frozen in ice mimicking a simple single-grained frozen soil structure. We filled the Snowbreeder

first with glass beads to a height of 5 mm and then filled this layer of glass beads carefully up with water, ensuring the surface of this layer to be as even as possible. Before placing a snow sample on top of this layer, we let the water freeze to obtain an ice-saturated layer of glass beads. These starting conditions of the experiments represented "Arctic conditions", where ice-saturated soils can be found. In the following, we refer to this glass-bead layer when writing 'soil'. We calculated the porosity ϕ of the soil as follows:

$$\phi = \frac{V_w}{V_t} \tag{5.2}$$

V_t corresponds to the total soil volume and V_w is the volume of the added water, which filled the pores and which we calculated from the weight of the added water w_w as $V_w = w_w/\rho_w$. ρ_w is the water density. The porosity does not depend on the diameter of the spherical glass beads, because they were monodisperse. Hence, we obtained a similar porosity for the three different soil types, which was between 0.35 and 0.37, i.e. the porosity of random close packing. Small differences in the porosity occurred probably due to small differences in the packing of the glass beads. We measured the heat conductivity of this artificial soil by imposing a temperature gradient ∇T on a frozen and dry soil sample and measuring the heat flux j through this sample. From these measurements we calculated the heat conductivity as

$$k_{soil} = \frac{j}{\nabla T} \tag{5.3}$$

These measurements resulted in values of $k_{soil,frozen}$ = 1 W m^{-1} K^{-1} and $k_{soil,dry}$ = 0.21 W m^{-1} K^{-1} for frozen and dry soil, respectively.

On top of the soil layer we placed a cylindrical snow sample of 1.5 cm height. We sampled the snow from blocks of nature-identical snow produced with the Snowmaker [Schleef et al., 2014a]. Before sampling, we sieved the snow (mesh size of the sieve: 5 mm) into Styrofoam boxes and stored the snow in these boxes at constant temperatures between -5°C and -20°C for several months. Thus, the snow sintered and developed a rounded structure through isothermal metamorphism. Starting experiments from a rounded snow structure enabled us to observe faceting during the experiments. The initial snow density was between 185 kg m^{-3} and 264 kg m^{-3} and the initial specific surface area SSA was between 13.7 m^{2}kg^{-3} and 17.5 m^{2}kg^{-3}. The calculation of the snow density and SSA from micro-CT images is explained further below in this section

The soil-snow interface was scanned periodically in the Micro-CT to measure the microstructural snow and soil evolution at the interface. We did one micro-CT measurement every four hours in Experiment 2 to 5 and in the ice-lens experiment. In Experiment 1, we did one micro-CT measurement every three hours. The peak energy and the

current of the X-ray tube were set to 70 kVp and 114 μA, respectively, in the Experiments 1 to 5. In the ice-lens experiment the peak energy and the current of the X-ray tube were set to 45 kVp and 88 μA, respectively. The integration time was 300 ms in Experiments 1 and 2 and in the ice-lens experiment, and 500 ms in Experiments 4 and 5. We chose a voxel size of 36 μm in all experiment. A total height of 11.2 mm was scanned in Experiment 1 and a height of 16.8 mm was scanned in all other experiments. Approximately one third of the images contained soil or ice and the other two thirds contained snow. According to these settings the scanning of one image took 1.5 hours in Experiment 1, 2.5 hours in Experiment 2 and in the ice-lens experiment, and 3.5 hours in Experiments 4 and 5. The exact height position of the Snowbreeder in the Micro-CT was measured with a linear encoder ($\pm$1 nm) so that always the same area within the sample was measured.

At the beginning and end of each experiment we took close-up images of snow grains to characterize the snow morphology. In contrast to the 3D images obtained with the Micro-CT, the close-up images show only single snow grains and not the full snow structure with bonds between snow grains.

5.2.2 Image processing and numerical simulation

To analyze the 3D images obtained with the Micro-CT we defined a volume of interest (VOI) in the form of a cuboid in the images. The side length of the cubic base of the cuboid was 5.22 mm. The height of the VOI was determined by the total scanned height. We divided the VOI into a snow part, a soil or ice-lens part and a transition part, in which both snow and soil occurred next to each other. The height of the transition part was between 0.4 mm and 1.1 mm. Within the snow part we defined a cubic sub-volume of interest directly above the transition part or the ice lens to analyze the structural snow evolution above the soil or ice lens. This cubic sub-VOI had a height of 5.22 mm so that the sub-VOI matched the representative volume of snow. We applied a Gauss filter with a sigma of 1.4 and a support of 2 voxels on the grayscale images. Then, we segmented the snow sub-VOI into ice and air voxels, based on the histogram of grayscale values in the sub-VOI. We used the same threshold for the segmentation of all images of one experiment. The soil part consisted of glass, ice and presumably also air. However, only two peaks appeared in the histogram of grayscale values within the soil part, i.e. one peak for glass voxels and one for voxels of the air-ice mixture in between the glass beads. Under these conditions we could segment the soil only into glass and air-ice mixture and not further into air voxels.

From the segmented 3D images we calculated structural snow parameters, i.e. den-

sity, specific surface area SSA, mean ice and pore size, with IPL (Image Processing Language from Scanco Medical AG). The SSA is defined as the ratio of the ice surface area to the ice mass:

$$SSA = \frac{\text{ice surface area}}{\text{ice mass}} \tag{5.4}$$

With an IDL program we calculated the flat-area fraction of the snow in the segmented 3D image. The flat-area fraction is defined as the ratio of flat areas to the total surface area of snow. The program determines flat areas as areas with small curvatures within the snow structure. Details on the calculations are given in Wiese and Schneebeli [2017c]. To compare the results with earlier experiments on snow metamorphism, we chose the same settings of the program as in Wiese and Schneebeli [2017c].

We simulated the temperature and temperature-gradient distribution in the experiment with a snow sample placed on top of an ice lens with a finite element model [Kaempfer et al., 2005]. This model is based on the finite element model of Van Rietbergen et al. [1995] for simulations of elastic deformations in bones, which can also be used for simulations of elastic deformations in snow (e.g. Wiese and Schneebeli [2017a]). We set the temperature to -2.35°C and -4°C at the bottom of the ice lens and at the top of the snow sample, respectively. A simulation of the temperature and temperature-gradient is so far not possible with this model, which is only written for segmented 3D images of snow, which contain only air and ice without any other additional materials such as glass beads. Additionally, we could not properly segment the grayscale images into air, ice and glass, as discussed above.

5.3 Results

5.3.1 Observations

The segmented 3D micro-CT images from the beginning and end of the experiments show that low-density layers and even air gaps formed in the snow above the soil after three weeks (Figures 5.1 (a), 5.1 (b), 5.2 (a) and 5.2 (b)). These low-density layers formed independent of the temperature gradient (both at 50 K m^{-1} and 100 K m^{-1}) and independent of the size of the frozen glass beads. A layer of low-density snow formed also above an ice lens, when subjected to a constant temperature gradient of 100 K m^{-1} (Fig. 5.3). The ice lens moved apparently downwards due to the sublimation on the upper boundary due to the vapor flux caused by the imposed temperature gradient. In the end

of the ice-lens experiment the ice lens seems to have been disappeared, but it just moved out of the scanned height and was still present at lower depth inside the Snowbreeder. Movies created from the 3D micro-CT images showing the structural snow evolution in all experiments are included in the online supplementary material. When we emptied the Snowbreeder at the end of the experiments, we could lift the snow sample easily from the soil layer, which supports the measured air-gap formation in the micro-CT images. Additionally, we noticed a drying of the soil, when we emptied the Snowbreeder. The uppermost part of the soil layer was composed of loose glass beads, while the remaining part was still frozen.

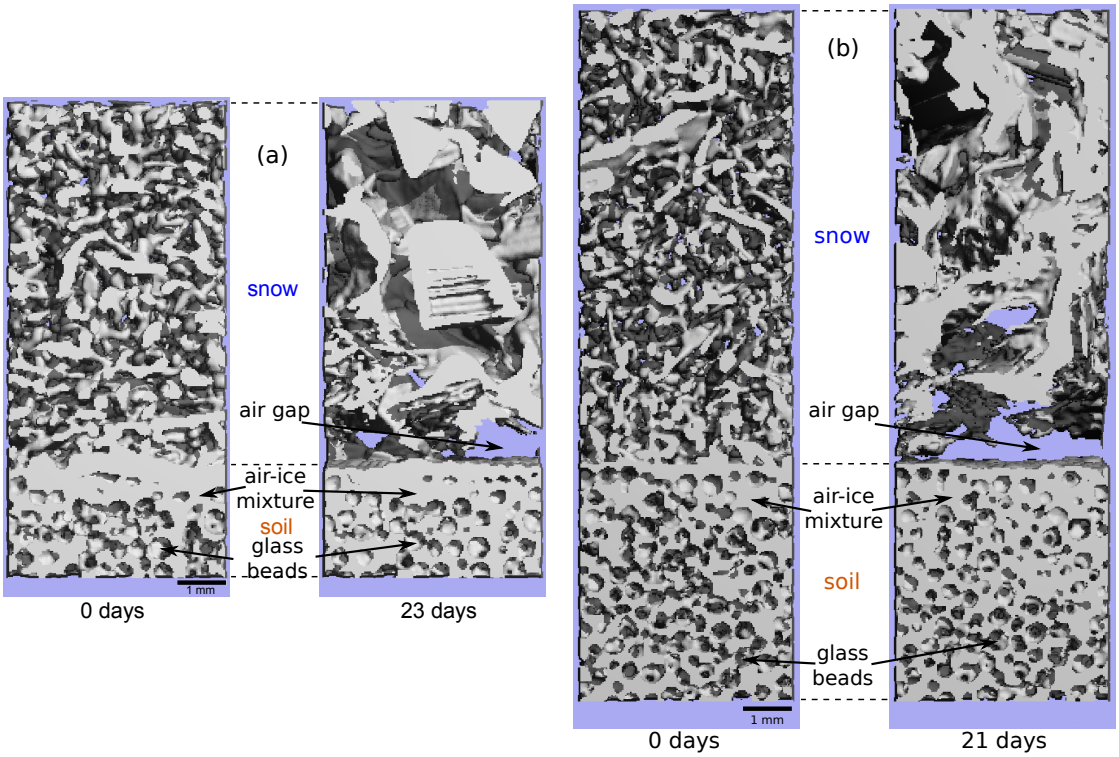

Figure 5.1: *3D micro-CT images of the snow structure above a soil layer composed of frozen glass beads (diameter: 0.5 mm) in the beginning and at the end of Experiment 1 (a, Tab. 5.1) and Experiment 2 (b, Tab. 5.1). The whole sample was subjected to a constant temperature gradient of 50 K m^{-1} (a) and 100 K m^{-1} (b) (higher temperature at the bottom).*

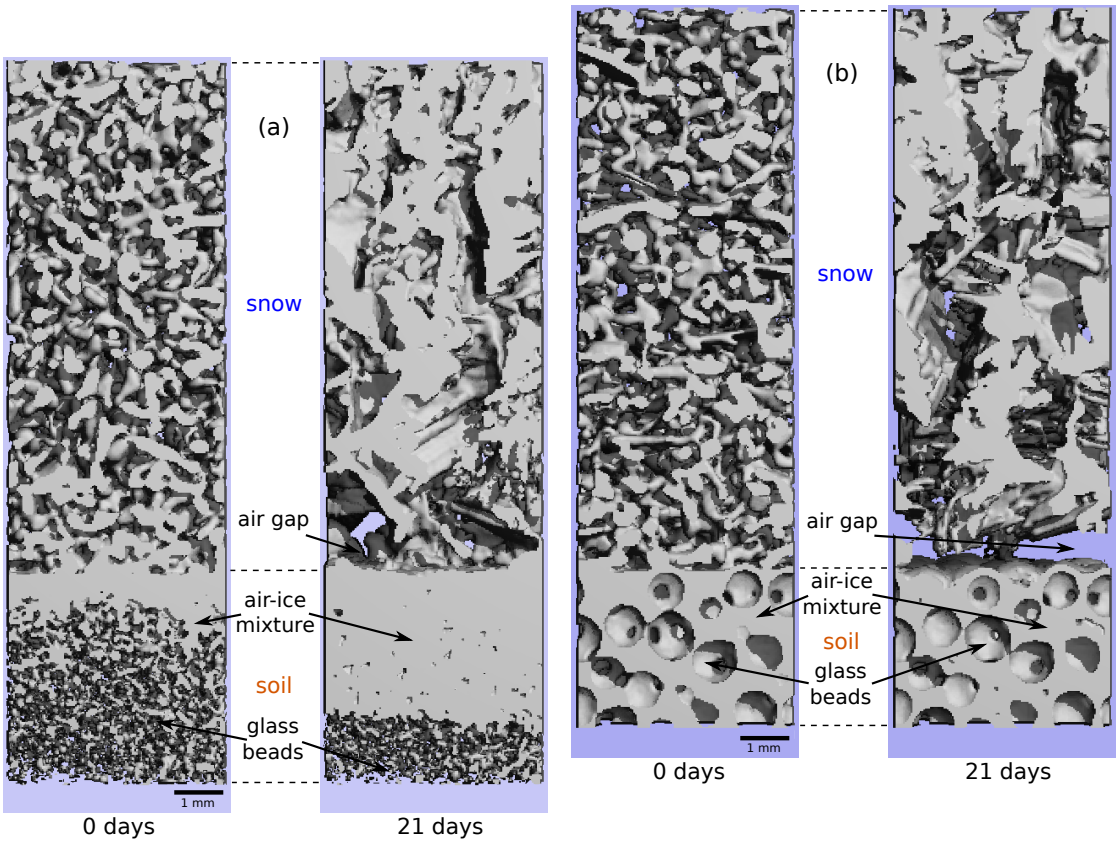

Figure 5.2: *3D micro-CT images of the snow structure above a soil layer composed of frozen glass beads (diameter: 0.1 mm (a) and 1 mm (b)) in the beginning and at the end of Experiment 5 (a, Tab. 5.1) and Experiment 4 (b, Tab. 5.1). In both experiments, the whole sample was subjected to a constant temperature gradient of 100 K m^{-1} (higher temperature at the bottom).*

5.3.2 Ice fraction

We calculated ice-voxel fraction profiles by calculating the ice-voxel fraction in each slice of the segmented 3D images to analyze the low-density snow layer above the soil and the ice lens in detail. Movies of the evolution of all profiles shown in Figures 5.4 and 5.5 are also included in the online supplementary material.

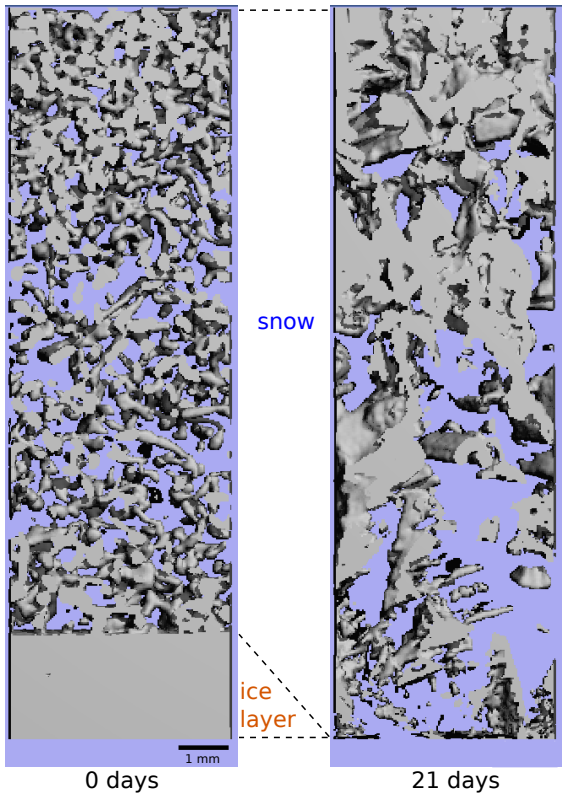

Figure 5.3: *3D micro-CT images of the snow structure above an ice lens in the beginning and at the end of the experiment (Tab. 5.1). The whole sample was subjected to a constant temperature gradient of 100 K m^{-1} (higher temperature at the bottom).*

Low-density snow layer height

In the snow the ice-voxel fraction ϕ_i is proportional to the snow density ρ_s by $\rho_s = \phi_i \cdot \rho_i$. All profiles show a density decrease in the snow above the soil layer and the ice lens with time (Fig. 5.4 and 5.5). In some experiments the snow density increased in the upper part of the snow sample. We calculated the height of the low-density snow layer z_{ld} as the height of a snow layer above the soil or ice-lens surface, in which the density was lower than in the initial profile (Fig. 5.6 and 5.8 (a)). Within this low-density layer we calculated the percentage density decrease with respect to the initial density (Fig. 5.7 and 5.8 (b)). While z_{ld} showed a relatively constant height of 2 to 3 mm in the Experiments 1 and 5 and the ice-lens experiment, z_{ld} increased quickly to higher values after around 4 days and decreased afterwards in the Experiments 2 and 4. The density within this low-density area decreased continuously in all experiments, reaching lowest values at the end of the experiments. We measured the lowest density decrease in Experiment 5

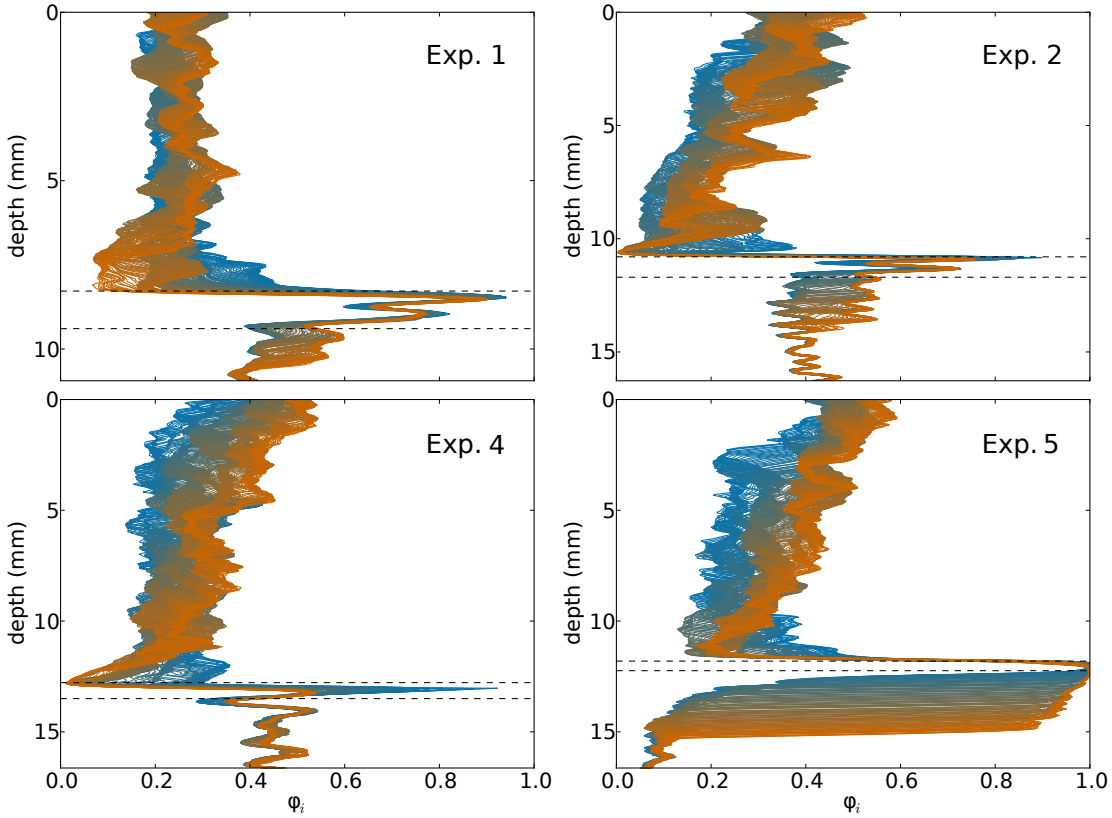

Figure 5.4: *Profiles of the ice-voxel fraction ϕ_i calculated from segmented 3D micro-CT images of the soil experiments. Blue: start of experiment, orange: end of experiment. The dashed lines indicate the transition zone between the snow and soil layer, in which both glass beads and snow were present. Temporal changes in the ice-voxel fraction values in the soil layer indicate only qualitatively a temporally changing composition of the soil, as described in detail in Section 5.3.*

and the ice-lens experiment. The evolution of the ice-voxel fraction profile of the ice-lens experiment shows additionally the lowering of the ice-lens surface ($\phi_i = 1$) with time.

Soil drying front

In the upper part of the soil we measured an increase in ice voxels with time. Since the layer of glass beads was initially ice-saturated, an increase in ice content was not possible. Also a decrease in glass giving place to more ice is physically not possible,

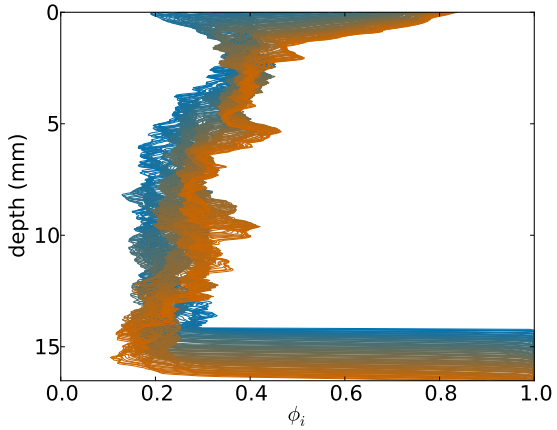

Figure 5.5: *Profile of the ice-voxel fraction ϕ_i calculated from segmented 3D micro-CT images of the ice-lens experiment. Blue: start of experiment, orange: end of experiment after 21 hours. ϕ_i = 1 at the bottom of the profile indicates the ice lens.*

as the glass beads did not move and cannot sublimate. The reason for the apparent ice increase was that the two peaks in the histogram of the grayscale values in the soil part of the VOI shifted towards smaller values when the soil composition changed with time. Hence, using a constant threshold for segmentation, more voxels in the image were assigned to be ice voxels, increasing the ice-voxel fraction. For a change in soil composition only a decrease in ice content, i.e. an increase in air content, was physically possible. Based on the detected drying of the initially ice-saturated glass beads at the end of the experiment, we interpreted an increase in ice-voxel fraction due to a shifting grayscale-value histogram as an increase in air content in the soil. In this way we could analyze the drying of the soil, even though we did not obtain quantitatively meaningful values of the ice-voxel fraction in the soil.

We defined the depth of the drying front as the depth, in which the ice-voxel fraction started to increase compared to the initial ice-voxel fraction at this depth of the soil. With time the drying-front depth z_{df} decreased linearly relative to the soil surface z_s (Fig. 5.9). The linear fits of the temporal evolution of the drying-front depth are as follows:

$$z_{df,Exp.1} - z_{s,Exp.1} = 0.09 \cdot 10^{-3} \cdot t - 1.05 \tag{5.5}$$

$$z_{df,Exp.2} - z_{s,Exp.2} = 0.17 \cdot 10^{-3} \cdot t - 1.11 \tag{5.6}$$

$$z_{df,Exp.4} - z_{s,Exp.4} = 0.17 \cdot 10^{-3} \cdot t - 0.74 \tag{5.7}$$

$$z_{df,Exp.5} - z_{s,Exp.5} = 0.16 \cdot 10^{-3} \cdot t - 0.35 \tag{5.8}$$

t corresponds to the time in days. The correlation coefficients are $r_{df,Exp.1} = 0.99$, $r_{df,Exp.2} = 0.99$, $r_{df,Exp.4} = 0.94$ and $r_{df,Exp.5} = 0.99$. The p-values are $p_{df,Exp.1} =$

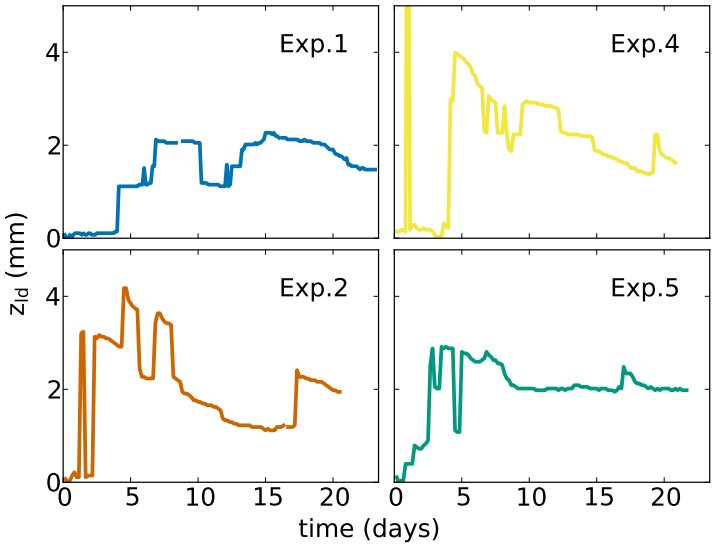

Figure 5.6: *Temporal evolution of the height of the low-density layer z_{ld} in the snow directly above the soil surface.*

$7.45{\cdot}10^{-114}$, $p_{df,Exp.2} = 5.74{\cdot}10^{-104}$, $p_{df,Exp.4} = 6.78{\cdot}10^{-49}$ and $p_{df,Exp.5} = 3.22{\cdot}10^{-120}$. The intercept of the linear fits is not exactly at 0 because of the transition part between the snow and the soil part, in which ice had to sublimate first before a drying of the soil could occur. The transition part had a height of 1.1 mm, 0.9 mm, 0.7 mm and 0.4 mm in the Experiments 1, 2, 4 and 5, respectively. These values fit approximately to the intercept values of the linear fits of the drying-front depth in these experiments. The slope of the linear fits gives the drying-front velocity. The lowest velocity occurred in the experiment with the lowest temperature gradient (Exp. 1). The higher velocities at a higher temperature gradient were similar and did not show an influence of the different soils composed of glass beads with different diameters.

Ice-lens movement

Similar to the evolution of the drying-front depth, we calculated the apparent movement of the ice lens from the ice-voxel fraction profile in the ice-lens experiment. The ice lens is visible as $\phi_i = 1$ in the profile. With time the depth of the ice-lens surface z_{il} decreased linearly relative to the initial depth of the ice-layer surface $z_{il,0}$ (Fig. 5.9). The linear fit of the temporal evolution of the ice-lens surface depth is as follows:

$$z_{il} - z_{il,0} = 0.11 \cdot t + 0.07 \tag{5.9}$$

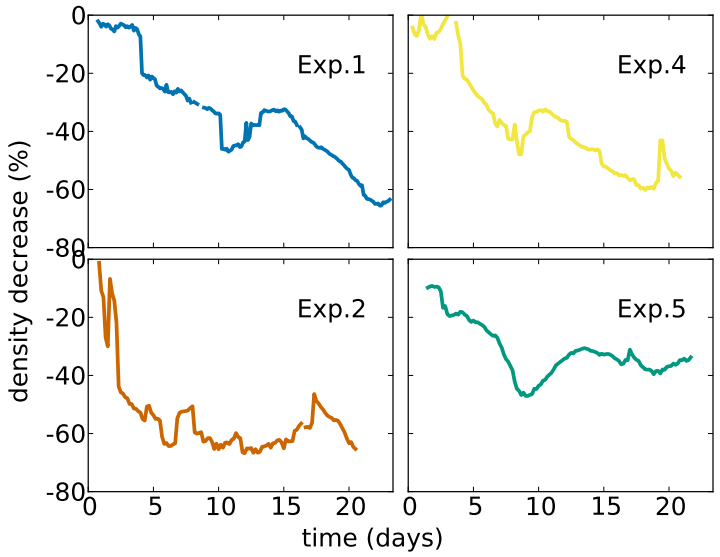

Figure 5.7: *Temporal evolution of the percentage density decrease within the low-density layer in the snow directly above the soil surface.*

t corresponds to the time in days. The correlation coefficient is $r_{il} = 0.92$ and the p-value is $p_{il} = 1.92 \cdot 10^{-47}$. The slope of the linear fit gives the velocity v_i of the ice-lens surface. This velocity was lower in comparison to the velocity of the drying front in the soil experiments with the same imposed temperature gradient of 100 K m^{-1}.

The ice-mass flux from the sublimating ice lens into the snow was $j = v_i \rho_i = 1.2 \cdot 10^{-6}$ kg m^{-2} s^{-1}. Since the vapor flux within the snow caused the sublimation of the ice lens, we compared j with the vertical vapor flux j_z within the snow above the ice lens. We calculated the vapor flux with the continuum model, in which the snow layer is simplified as two ice plates with air in between [Pinzer et al., 2012]. The distance between the two ice plates is the height of the snow layer and the temperatures at the plates are the temperatures at the top and the bottom of the snow layer. We measured the temperature T_{top} at the top z_{top} of the snow sample with the Snowbreeder. The temperature T_{int} at the bottom of the snow sample, i.e. at the snow-ice lens interface z_{int}, was not measured, so that we calculated T_{int} from heat conduction through a composite sample. As the heat flux at the snow-ice lens interface is continuous, i.e. $q_s = q_i$, we calculated T_{int} as follows:

$$T_{int} = \frac{\frac{k_i}{z_{int}-z_{bot}} T_{bot} + \frac{k_s}{z_{top}-z_{int}} T_{top}}{\frac{k_s}{z_{top}-z_{int}} + \frac{k_i}{z_{int}-z_{bot}}} \tag{5.10}$$

T_{bot} is the temperature measured with the Snowbreeder at the bottom of the ice

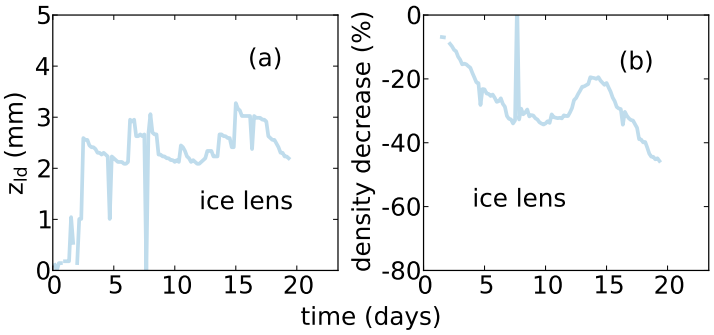

Figure 5.8: *Temporal evolution of the height of the low-density layer z_{ld} in the snow (a) and the percentage density decrease within this low-density layer (b) directly above the ice-lens surface.*

lens z_{bot}. $k_i = 2.2\,\mathrm{W\,m^{-1}\,K^{-1}}$ is the heat conductivity of ice. For the heat conductivity of snow k_s we took the value for the vertical heat conductivity of rounded snow with a density of the snow in the ice-lens experiment, which is approximately $k_s = 0.17\,\mathrm{W\,m^{-1}\,K^{-1}}$ [Riche and Schneebeli, 2013]. We calculated the vertical vapor flux j_z between the two ice plates in the continuum model with Fick's law [Pinzer et al., 2012]:

$$j_z = -m_{H_2O} D_0 \frac{\partial c_e}{\partial z} \tag{5.11}$$

m_{H_2O} is the mass of a water molecule, c_e corresponds to the water-vapor concentration and D_0 is the water-vapor diffusion coefficient in air, which we calculated as follows [Massman, 1998]:

$$D_0 = 2.178 \cdot 10^{-5} \frac{1013\mathrm{hPa}}{p_{mean}} \left(\frac{T_{mean} + 273.15}{273.15} \right)^{1.81} \tag{5.12}$$

With a mean temperature of $T_{mean} = -3.13°\mathrm{C}$ and a mean air pressure at the height of the cold laboratory in Davos of $p_{mean} = 840\,\mathrm{hPa}$ the water-vapor diffusion coefficient had a value of $D_0 = 2.57 \cdot 10^{-5}\,\mathrm{m^2\,s^{-1}}$. We calculated the equilibrium water-vapor concentration c_e above the ice surfaces according to the ideal gas law:

$$c_e = \frac{e_i}{k_b T} \tag{5.13}$$

$k_b = 1.38 \cdot 10^{-23}\,\mathrm{J\,K^{-1}}$ is the Boltzmann constant, T is the snow temperature in K and e_i is the equilibrium water-vapor pressure above ice, which we calculated with the empirical Magnus formula [World Meteorological Organization (WMO), 2008]:

$$e_i = 6.112 \exp\left(\frac{22.46t}{272.62 + t} \right) \tag{5.14}$$

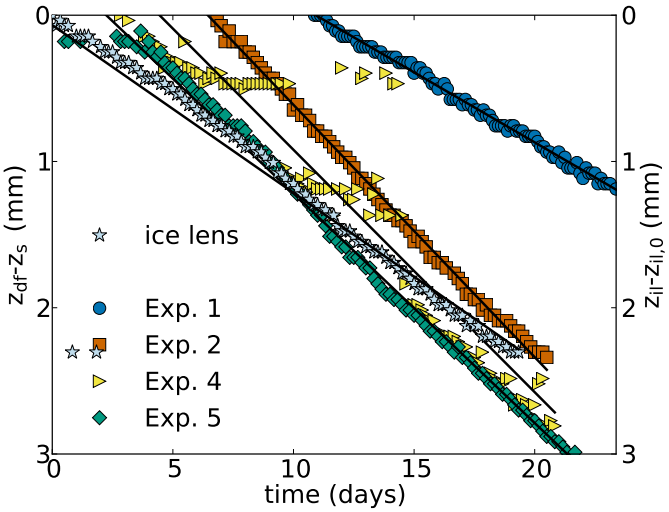

Figure 5.9: *Temporal evolution of the drying-front depth z_{df} below the soil surface z_s and the depth of the ice lens z_{il} relative to the initial ice-lens depth $z_{il,0}$. The black lines are linear fits given in Equations 5.5, 5.6, 5.7, 5.8 and 5.9.*

t corresponds to the snow temperature in °C. For the calculations described above we used only the initial conditions, e.g. snow density and height and ice-lens height, and did not account for temporal changes in the ice-lens height and vertical snow-density profile. The calculations resulted in a vertical mass flux of $j_z = 1.04 \cdot 10^{-6}\,\mathrm{kg\,m^{-2}\,s^{-1}}$. The value for j_z is 14% smaller than the mass flux j calculated from the ice-lens surface velocity.

5.3.3 Surfaces for sublimation and deposition

The ice surfaces available for sublimation and vapor deposition are different on an ice lens, in snow and in soil. Fig. 5.10 shows an example, in which snow is simplified as spheres in a close cubic packing lying on an ice lens and a layer of frozen glass beads. The available ice surface for sublimation A_s is smaller on an ice lens than the available ice surface for deposition A_d in the snow directly above. In the free space between two "snow spheres" A_s is given as

$$A_s = (2r)^2 \tag{5.15}$$

with the radius r of the "snow spheres". A_d on the quarters of "snow spheres" directly above A_s is given as

$$A_d = 4 \cdot \frac{1}{4} A_{sphere} = A_{sphere} = 4\pi r^2 \tag{5.16}$$

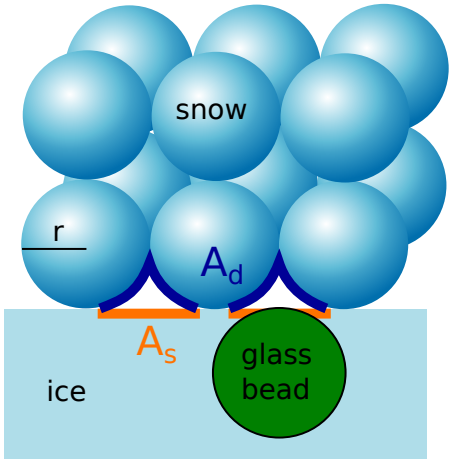

Figure 5.10: *Ice surfaces available for sublimation A_s and deposition A_d at the interface between snow (simplified as spheres with cubic packing) and an ice lens or ice-saturated soil. A_s is smaller on an ice lens than A_d in the snow directly above. Due to the soil particles, represented by glass beads in our experiments, A_s is even smaller in soil. r is the radius of the "snow spheres".*

Hence A_d is larger than A_s: $A_d = \pi A_s$. Due to the soil particles, represented by glass beads in our experiments, A_s is even smaller in soil, because some of the sublimation surface is occupied by the glass bead (Fig. 5.10).

5.3.4 Simulations

The temperature and temperature-gradient simulations of the ice-lens experiment show large variations in the temperature gradient throughout the whole sample (Fig. 5.11, 5.12, 5.13), both in the beginning and at the end of the experiment. Lowest temperature gradients occur in the ice lens and in dens snow. Highest temperature gradients, locally above the imposed temperature gradient of 100 K m^{-1}, occur in snow with a low density. The slight low-density snow layer above the ice lens shows the highest temperature gradients.

5.3.5 Microstructural snow evolution

The snow structure evolved typically for constant temperature-gradient metamorphism. In the initially rounded snow we observed depth-hoar formation (Fig. 5.14), which is

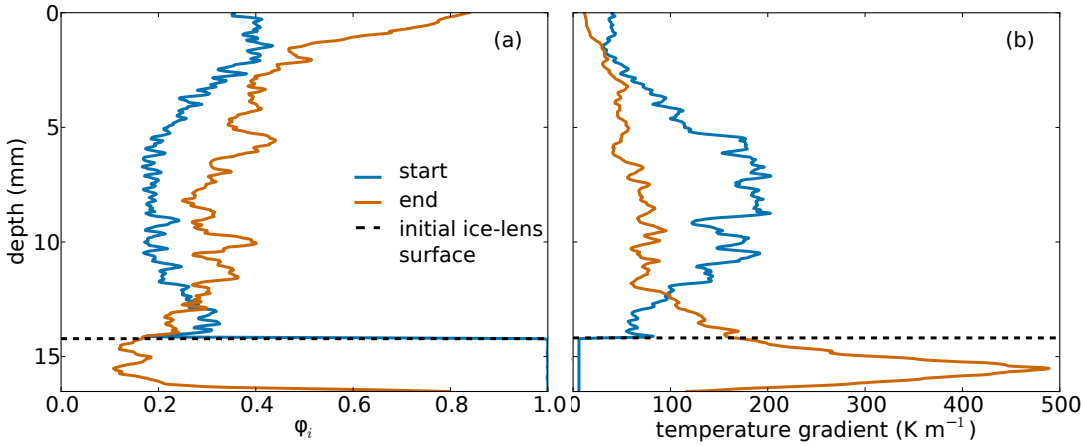

Figure 5.11: *Ice-fraction profiles (a) and the simulated temperature gradient (b) in snow at the beginning and in the end of the ice-lens experiment. The temperature gradient in (b) is the mean over a slice of the 3D image. The black dashed line indicates the initial height of the ice-lens surface. At the end of the experiment the the ice-lens surface is at the bottom of the image.*

reflected in an increase in flat-area fraction (Fig. 5.15). Close to the top of the Snowbreeder clusters of hard dense depth hoar formed (Fig. 5.14 (d)), matching the density increase at the top of the snow profiles.

Also typical for constant temperature-gradient metamorphism the SSA decreased with time (Fig. 5.16 (b)). In contrast to earlier SSA measurements in snow under a constant temperature gradient (e.g. Pinzer et al. [2012], Calonne et al. [2014]), the SSA decreased non-monotonously. In Experiment 4 and in the ice-lens experiment the SSA even increased after ten days. In Experiment 2 the SSA decreased slower than in Experiment 1, even though the temperature gradient was larger than in Experiment 1.

Due to the coarsening during temperature-gradient metamorphism the mean ice thickness and the pore size of the snow structure increased with time (Fig. 5.16 (c) and (d)). This increase was similar for all experiments, except of for Experiment 2. In this experiment the ice thickness increased less strong and the pore size increased stronger than in the other experiments, leading to a stronger density decrease in the beginning of Experiment 2 compared to the density evolution in the other experiments (Fig. 5.16 (a)). The snow density calculated in the VOI directly above the transition layer between snow and soil and above the ice lens does not reflect the density decrease apparent in the density profiles (Fig. 5.16 (a)). Except of in the first days of Experiment 2, the snow density decreased only slightly, stayed almost constant or even increased.

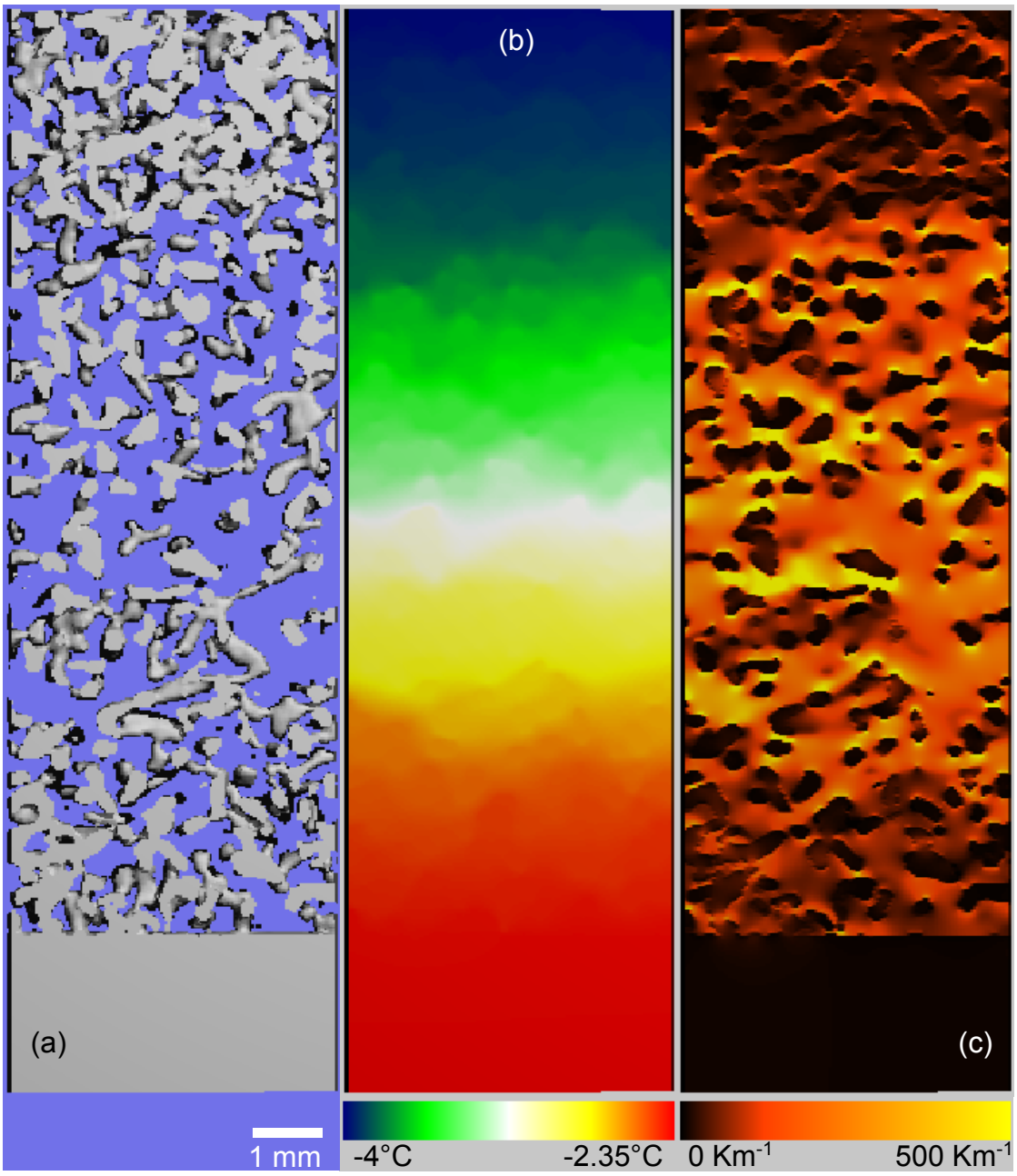

Figure 5.12: *3D micro-CT image of the snow structure above an ice lens (a), the simulated temperature (b) and temperature gradient (c) in the beginning of the ice-lens experiment (Tab. 5.1).*

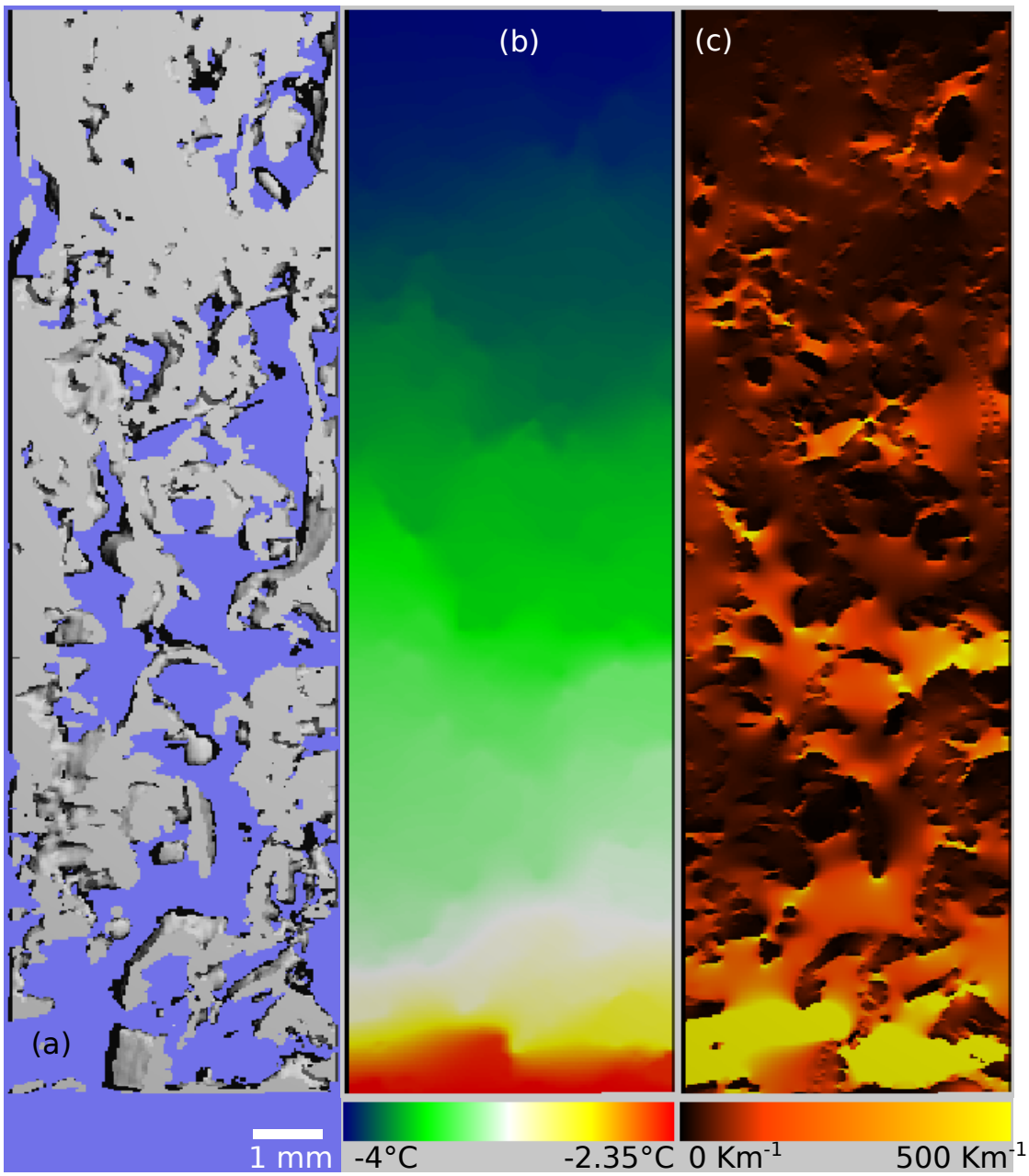

Figure 5.13: *3D micro-CT image of the snow structure above an ice lens (a), the simulated temperature (b) and temperature gradient (c) at the end of the ice-lens experiment after 21 days (Tab. 5.1).*

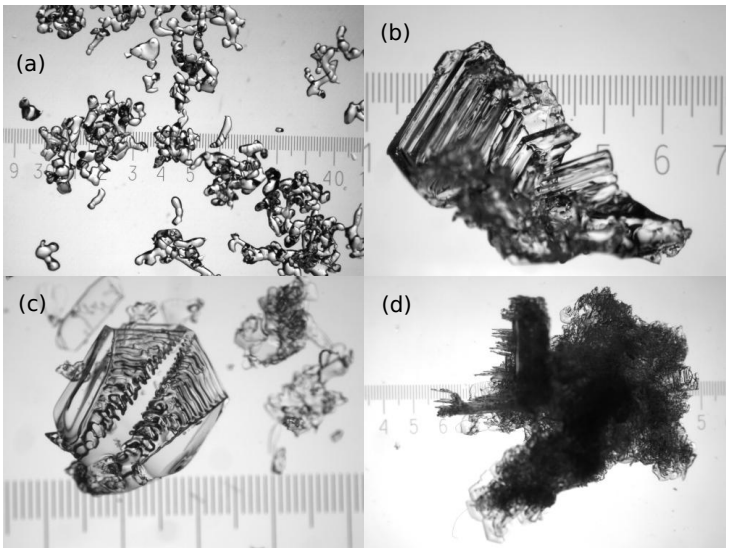

Figure 5.14: *Close-up images of snow grains before the experiments (a), close to the soil surface after Experiments 1 (b) and 2 (c) and close to the top of the Snowbreeder after Experiment 2 (d). The scale in the images is labeled in millimeters.*

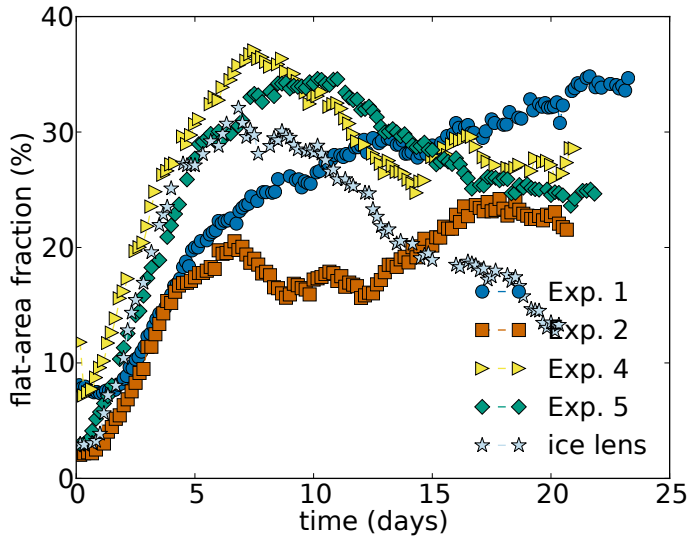

Figure 5.15: *Temporal evolution of the flat-area fraction within a height of 5.22 mm above the soil and the ice lens.*

5.4 Discussion

With time-lapse micro-CT experiments we investigated the effect of different soils on the structural snow evolution at the soil-snow interface under the influence of a constant

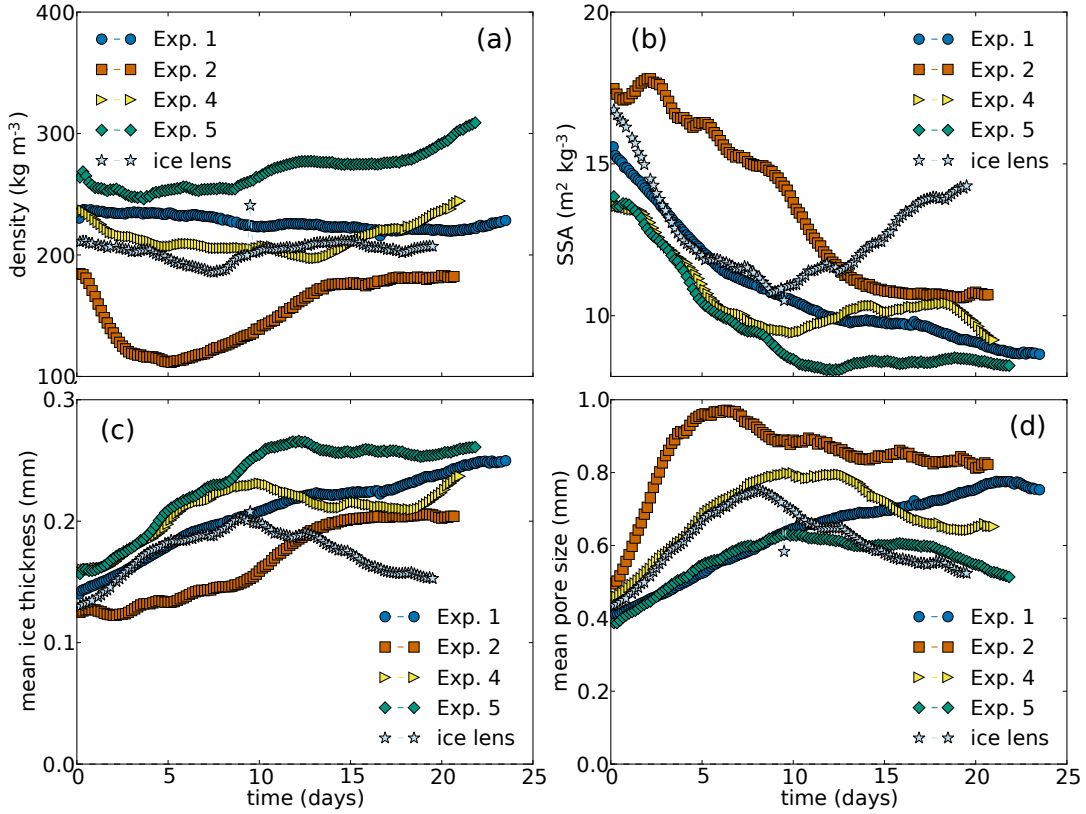

Figure 5.16: *Temporal evolution of the snow density (a), SSA (b), mean ice thickness (c) and mean pore size (d), calculated in the CT images within a height of 5.22 mm above the soil and the ice lens.*

temperature gradient. We found that independent of the diameter of the glass beads in the laboratory soil and independent of the magnitude of the temperature gradient, a 2 to 3 mm layer of low-density snow formed in the snow above the soil. Such a low-density snow layer of a similar height formed also above an ice lens. The temperature simulations showed an increased temperature gradient within this layer of low-density snow. We measured a constant drying of the uppermost part of the soil with time, which depended on the temperature gradient. Based on our findings we discuss our hypotheses on the structural snow evolution above soil in the following.

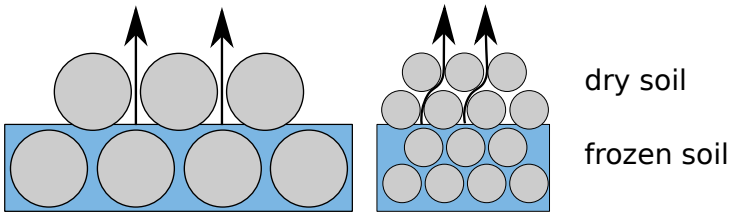

Figure 5.17: *Idealized vapor flux through partly dried snow composed of glass beads with different diameters. Grey spheres: glass beads, blue background: ice, black arrows: water-vapor flux.*

5.4.1 Drying of the soil

We hypothesized that a continuous vapor flux from the soil to the snow due to the constant temperature gradient leads to a drying of the soil, eventually stopping the vapor transport from the soil to the snow. Simultaneously, the vapor flux in the snow will continue, leading to air-gap formation in the snow above the soil. Indeed, we observed and measured a drying of the uppermost millimeters of the soil, similar to field observations of Domine et al. [2016], who measured also a low-density depth-hoar layer above a dried soil. However, only the uppermost part of the soil dried out in our experiments so that the vapor transport did most probably not break down completely and water vapor was transported into the snow during the full duration of the experiments. Hence, a complete drying of the soil causing a break down of the vapor flux within the soil was not necessary and not the reason for the observed density decrease in the snow above the soil. Additionally, we observed also the formation of low-density snow above an ice lens, where vapor supply was always guaranteed by the sublimation of the ice lens. A similar air-gap formation above an ice crust was also observed by Greene [2007]. A complete drying could have only explained the formation of low-density snow in our laboratory and not in a natural snowpack. In natural soil, vapor fluxes can occur over many meters in depth. However, the vapor fluxes get increasingly smaller with an increasing distance Δz between the ice surfaces in the soil and the snow Δc_e, when the vapor-concentration difference remains approximately constant (Equation 5.1).

Differences in heat conductivity

Connected with the drying of the soil, we assumed that different heat conductivities lead to different temperature gradients in the soil and the snow, resulting in varyingly strong vapor fluxes and a net mass loss at the soil-snow interface. Such an effect of varyingly strong temperature gradients can only become apparent after the soil dried at least partly,

since a water-vapor flux cannot occur in ice-saturated soil. However, we measured a heat conductivity of 0.21 $W\,m^{-1}\,K^{-1}$ in dry soil, which is close to the estimated vertical heat conductivity of snow with a density used in our experiments, which lies between 0.1 and 0.25 $W\,m^{-1}\,K^{-1}$ [Riche and Schneebeli, 2013]. Hence, the temperature gradient and the resulting vapor flux within the snow and the dry soil differed probably not much and did probably not cause the snow-density decrease above the soil. Additionally, this effect could not explain the snow-density decrease, which occurred also above the ice lens.

Tortuosity effect

As another effect of the drying of the soil, we hypothesized that after the uppermost part of the soil dried, the tortuosity of this dry part affects the vapor flux from deeper parts of the soil into the snow. The tortuosity of a porous medium decreases the vapor diffusivity of a gas compared to the diffusivity of the same gas in air, because the porous medium is a barrier to vapor diffusion (Equation 5.1). We could not measure or estimate the tortuosity of the soil. However, we expected that the tortuosity effect leads to varyingly strong vapor fluxes in soil compared to snow, leading to a net mass loss at the soil-snow interface. This tortuosity effect can become apparent only after some drying of the soil occurred. Hence, this effect could not explain the rather immediate formation of the observed low-density snow layer and the density decrease above an ice lens. The density decrease above the soil started latest after four days, when the drying of the soil also just started. Even after some drying of the soil occurred, we could not find an effect of varyingly strong vapor fluxes in the snow and in the dried soil, as the drying-front velocity was constant with time in all soil experiments.

The tortuosity depends on the diameter of the glass beads in the soil, as depicted in Fig. 5.17. For example, after 1 mm of drying the tortuosity of a soil with glass-bead diameter of 1 mm should be lower than the tortuosity of soil composed of smaller glass beads with the same porosity, because more complex pathways for water vapor exist in the latter case. This difference in tortuosity will lead to a decreased diffusivity and vapor flux in the soil composed of small glass beads compared to the soil composed of large glass beads. We could not find a dependency of the possible tortuosity effect on the glass-bead diameter, because the drying-front velocity was almost the same in all soil experiments with the same temperature gradient. We could probably not see the effect of different tortuosities, because of the rather small drying of the rather coarse soils. In summary, the drying of the soil depended mainly on the imposed temperature gradient and probably also on the soil porosity determining the ice content exposed to sublimation, but not on the diameter of the glass beads.

5.4.2 Ice-surface area for sublimation and deposition

With the calculation in Section 5.3.3 based on the sketch in Fig. 5.10, we simplified the interface between snow and an ice lens or soil. The calculation shows that the area of the flat ice-lens surface is smaller than the round surfaces of the overlying ice spheres, which represented snow in this calculation. Hence, the area for sublimation is smaller than the area for deposition. Hence, the vapor sublimating at the ice-lens surface, is distributed over a larger surface on the overlying snow structure when deposited again. This leads to a faster apparent downward movement of the ice lens due to sublimation compared to the apparent downward movement of the overlying snow due to vapor deposition. This will lead to an air-gap formation between the ice lens and the snow. This effect gets probably enhanced, when there are additional soil particles in the ice, as indicated by a glass bead in Fig. 5.10. These soil particles decrease the ice surface available for sublimation even more, which could explain the stronger density decrease over the soil than over the ice lens. A temperature gradient in the opposite direction would probably have a similar effect on the interface between snow and soil or an ice lens. In this case, the surface for sublimation in the snow would be larger than the surface for vapor deposition on the ice l

5.4.3 Temperature-gradient evolution

Our temperature simulations show the development of a strong macroscopic, i.e. horizontally averaged, temperature gradient within 4 mm of snow above the ice lens. This high temperature gradient occurred according to the inhomogeneous snow microstructure and the decreased density, i.e. a reduced amount of ice structures, which have a higher heat conductivity than air. Similarly, Hammonds et al. [2015] measured a three times higher temperature gradient in the first millimeter of snow above an ice lens compared to the imposed temperature gradient of $100\,\mathrm{K\,m^{-1}}$. Hammonds and Baker [2016] discussed that the main contribution to this ”enhanced temperature gradient” was a high thermal contact resistance and a low effective thermal conductivity of the snow directly above the ice layer. However, our temperature simulations combined with the density measurements from the CT images show that the temperature gradient above the ice lens was not ”enhanced”, but simply caused by the formation of a layer with different physical properties than the initial snow layer above the ice lens. As the density profiles reveal, we did not have a high thermal contact resistance between the snow and the ice lens in the beginning of the experiment. The strong temperature gradient towards the end of the experiment led to fast recrystallization within the snow above the ice lens, causing a strong depth hoar formation (Fig. 5.14).

5.4.4 Microstructural snow evolution

Besides the evolution of low-density snow layers we analyzed further possible effects of the soil on the structural snow evolution in a representative volume of snow above the soil and ice lens. The snow density calculated in this volume did not reflect the low-density layers visible in the ice-fraction profiles. This is due to the size of the volume, which had a height of 5.22 mm. The height of the low-density layer was only around 2 to 3 mm. Hence, also layers with constant or even increased density were included in the analyzed volume and could possibly compensate the low-density layer. The density increase in the uppermost part of the Snowbreeder would probably not occur in nature. In our experiments the tight top of the Snowbreeder acted as a barrier to the vapor transport in the snow, leading to the formation of clusters of dense depth hoar and a snow-density increase in the upper part of the snow sample.

In contrast to earlier temperature-gradient metamorphism experiments, the SSA decreased non-monotonously. Since we measured the SSA evolution close to the soil-snow interface, an effect of the underlying soil on the SSA evolution might be possible. However, the SSA evolution did not show strong differences between different soil types, especially in the first ten days. Only Experiment 2 shows a less strong SSA decrease than the other experiments. However, in this experiment we used the same soil type as in Experiment 1. The SSA increase in the second half of the ice-lens experiment might have resulted from the continuous decrease of the ice-lens height due to the continuous sublimation. We shifted the VOI according to the ice-lens sublimation so that we analyzed always the snow structure above the ice-lens surface. However, with this method we did not measure the SSA always at exactly the same position within the snow sample.

We assumed that different tortuosities of different soil types could affect the ice and pore-size evolution of the snow above the soil, because the pathways of the water vapor entering the snow from the soil might differ. However, we did not measure a clear difference in the ice and pore-size evolution in experiments with different soils, especially in the first 10 days. After the first 10 days, the ice and pore size evolved, but still there is no clear correlation between the diameter of the glass beads and the ice and pore size visible, e.g. larger pores due to a larger glass-bead diameter. Again, Experiment 2 shows the largest difference compared to the other experiments. The pore-size increase was much stronger, which is reflected in the strong density-decrease in the beginning of this experiment. As already discussed before, we can exclude an effect of the soil type, since we used the same soil in Experiment 1. Possibly the lower initial density played a role in the different structural evolution of the snow in Experiment 2 compared to the other experiments.

5.4.5 Laboratory vs. nature

We conducted our experiments under simplified laboratory conditions with artificial soils and a strong constant temperature gradient. Under natural conditions less strong temperature gradients might occur at the soil-snow interface, depending on the depth of the snowpack. However, we think that in shallow snowpacks, like in the Tundra, strong temperature gradients can occur at the soil-snow interface, possibly leading to the observed snow evolution. Also less strong temperature gradients acting over a longer time might result in a similar formation of low-density snow above soil. Another limitation of our experimental setup is the monodisperse composition of the soil. Natural soil has usually a particle size distribution. The water-vapor diffusivity might vary spatially in rather inhomogeneous soils, depending on the pore space of the soil. Such spatial differences in vapor diffusivity might lead to spatially different effects on the snow above the soil. This might have caused the formation of the hard snow viaducts on asperities of rough ground observed by Bader et al. [1939]. Additionally, we did not consider an additional effect of plants growing in the soil in our experimental setup.

5.5 Conclusions

In the time-lapse micro-CT experiments we measured a snow-density decrease in 2 to 3 mm height above different artificial soil types and an ice lens under the influence of a constant temperature gradient. We discussed four possible reasons for the low-density layer formation: a drying of the soil decreasing or stopping the vapor flux from the soil to the snow, varyingly strong vapor fluxes in snow and soil due to different heat conductivities leading to a net mass loss at the soil-snow interface, different tortuosities in different soils leading to a decreased vapor flux in the soil, and differences in ice-surface area for sublimation and deposition. The first three effects could not explain the low-density layer formation adequately. The experiments were not long enough so that a complete drying of the soil could occur, which would have stopped the vapor flux from the soil to the snow. For an effect of varyingly strong vapor fluxes from the soil to the snow due to varyingly strong temperature gradients or different tortuosities, a partial drying of the soil was required. We measured such a partial drying, but the layer of low-density snow formed already, when the drying of the soil just started. Additionally, the heat conductivity of the dry artificial soil was similar to the heat conductivity of the snow above, leading to similar conditions for a resulting vapor flux. Hence, the primary reason for the formation of the layer of low-density snow was a smaller sublimating surface compared to the ice surface available for vapor deposition. This surface-area

effect can also explain the formation of the layer of low-density snow above the ice lens. In the soil experiments the snow-density decrease might have been stronger due to an additional small effect of the drying of the soil, i.e. through a tortuosity effect on the vapor flux and an increased distance between the snow and the ice-surface in the soil. The high temperature gradient above the ice lens was not the reason for the snow-density decrease, but vice versa the density decrease led to the high temperature gradient.

The formation of a layer of low-density snow or even air gaps within the snow above ground can have strong impacts on wildlife and avalanche formation. As observed, several animals living in cold regions rely on low-density snow on the ground to move easily within the snow and search for food on the snow-covered ground. Hence, the formation of low-density snow or even air gaps in the snow close to the ground can favor wildlife. In the case of avalanche formation it was often observed that burried ice crusts can lead to avalanches [Hammonds et al., 2015]. The reason for this might be an air-gap formation in the snow at the top of an ice crust. A layer of low-density snow above the ground can have a similar effect. Possibly late-winter and early-spring avalanches can be triggered by such a layer, after a temperature gradient acted on the snow cover over the course of a winter and led to a well-developed low-density layer close to the ground, which can easily collapse. The low-density snow formation both on the ground and above an ice lens will be difficult to measure in the field, since with a height of a few millimeters this snow layer is too thin to be measured with field instrumentation. Similar to a freshwater-ice lens, a layer of low-density snow can also form on sea ice, which has an important impact on the sea ice below and interactions between the ocean, atmosphere, sea ice and snow.

Chapter 6

Summary and outlook

In this thesis different mass fluxes within the snow structure were investigated at the microscale. The most obvious microscale mass flux within the snow structure is the vapour flux induced by curvature and temperature differences in the snow structure. Additionally, the densification of snow caused by settlement is another mass flux occurring internally in snow. We conducted three series of experiments investigating the single and combined effects of these fluxes, and we summarise the results as follows:

- Alternating temperature gradients, both symmetric and asymmetric, led to an anisotropic snow microstructure and a reduced SSA decay compared to unidirectional temperature gradients, while faceting depended on the asymmetry of the alternating temperature gradient.

- Temperature-gradient metamorphism reduced the settlement compared to isothermal conditions due to the stiffening of the snow structure through the formation of stress-bearing chains.

- Strong temperature gradients across a snow-soil or snow-ice interface led to a density decrease in the snow directly above the interface due to the difference in

the available surface area between sublimation and deposition of water vapour.

These results show that snow is a very dynamic material, in which complex non-linear processes occur (Fig. 6.1). Both the water-vapour flux in snow and snow settlement affect the snow microstructure by changing for example the SSA, density and anisotropy of the snow microstructure. Through the resulting snow metamorphism the two mass fluxes interact with each other. This interaction becomes especially apparent in the decreased settlement through the formation of stress-bearing chains in the snow structure due to temperature-gradient metamorphism. In addition to the internal mass fluxes, also mass fluxes across the interfaces of a snowpack affect the snow microstructure. For example, at the ground a gradient in material, i.e. soil and ice, and density, i.e. ice lens and snow, appears, which affects the water-vapour flux across this interface.

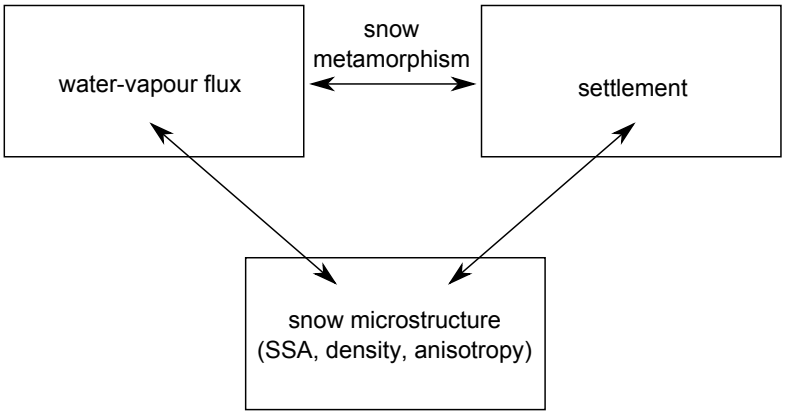

Figure 6.1: *Sketch of the complex interactions between the water-vapour flux within the snow structure, settlement of snow and the snow microstructure.*

The complex non-linear processes at the microscale cause macroscopic phenomena observed in the field. For example stress-bearing chains in the snow microstructure explain the observed reduced settlement of depth-hoar layers. However, processes at the microscale are difficult to measure in the field. Hence, laboratory experiments under defined controlled and simplified conditions bridge the gap in observation techniques and allow a quantitative interpretation of the observations at the macroscale. In this context time-lapse micro-computed tomography measurements are the perfect tool. With these measurements the changing snow microstructure can be observed under controlled conditions. The resulting 3D images and movies do not only show the morphological snow evolution, but they also reveal the temporal evolution of the interior of the snow microstructure. Simulations of temperature and stress distributions with these images further help to understand the macroscopic effect of the microstructural snow evolution.

Even though relatively simple experimental setups are only an approximation of conditions occurring in a natural snowpack, single processes can be well investigated to compare with theory. Experiments under simplified experimental conditions showed for example that a simple distinction of isothermal and temperature-gradient metamorphism based on snow morphology and a critical temperature gradient is insufficient. As shown in the presented experiments, high temperature gradients can lead to both faceting and a rounded snow structure.

The insights from controlled laboratory experiments provide explanations for empirical field observations as well as data for the quantification and parameterisation of snowpack processes in snowpack models. However, open questions remain. The conducted experiments cover only a small range of the parameters influencing the snow microstructure. To understand the evolution of the snow microstructure and the effect on macroscopic snowpack properties and processes better, further detailed metamorphism experiments under the influence of various temperature-gradient amplitudes and directions, temperatures, strain rates and snow types are required. With the following experiments and setup improvements the presented experiments could be complemented:

- Alternating temperature gradients: the effect of further asymmetries should be investigated. For example in experiments with a certain cycle various differences in the duration, amplitude and mean snow temperature of the positive and negative part of the alternating temperature gradient could be investigated. Additionally, the effect of alternating temperature gradients on faceted snow was not yet analysed. Such experiments are necessary to get a better understanding of the morphological and geometrical snow evolution. In this context the traditional snow-metamorphism definitions based on morphology and a critical temperature gradient should be reviewed.

- Settlement: The presented experiments were only conducted with rounded snow of a certain density. Therefore, experiments on the effect of a constant temperature gradient on the settlement of different snow types, with typically different density, like new snow and faceted snow, should be conducted. Also the effect of the snow density and alternating temperature gradients on the formation of stress-bearing chains should be investigated. Such detailed measurements of the mechanical snow properties under the influence of a temperature gradient under various conditions are necessary to formulate general parameterisations for snow settlement in snowpack models.

- Ground-snow interface: A density gradient occurs not only across an interface

between an ice lens and snow, but also between snow layers of different density. Further experiments could show whether the latter conditions lead to a similar snow-density decrease above the interface as in snow above an ice lens. To quantify the effect of the difference in the available surface for sublimation and deposition, an experiment with ice beads on an ice lens under the influence of a constant temperature gradient should be conducted. As the stress of the overlying snow is highest at the ground-snow interface, the effect of settlement should also be added in the ground-snow interface experiments to analyse a possible settlement effect on the snow-density decrease above the interface.

- Changes of the experimental setup: The Snowbreeder 5 might be extended to impose also alternating temperature gradients in addition to a unidirectional temperature gradient, while the snow sample settles. With such a Snowbreeder all possible temperature, pressure and ground-snow interface conditions could be simulated in time-lapse micro-CT experiments. Additionally, with a different Micro-CT the resolution could be increased, which is necessary for experiments with new snow.

The work presented here allows now a parameterisation for sign-changing temperature gradient metamorphism, which should improve the snow-albedo feedback parameterisation in climate models. The physical understanding for the increasing viscosity during temperature gradient metamorphism could be substantiated. The formation of a low-density snow layer over ice and soil could be quantified and physically explained. In sum, several practically relevant processes in snow physics could be elucidated.

Acknowledgements

This thesis was only possible with the great support of many people.

First of all I would like to thank Martin Schneebeli for the supervision of this thesis. Thanks for coming up with many interesting ideas, discussions and thanks for the encouragement. I would also like to thank Prof. Dani Or for accepting me as a PhD student and for the discussions. Moreover, thanks to Florent Dominé who agreed to be co-examiner.

This thesis was funded by the Swiss National Science Foundation (project number 200021_143839).

The laboratory experiments would not have worked without the great help of Matthias Jaggi, Margret Matzl, Sascha Grimm, Luca Frank, Patrick Angehrn, Amy Macfarlane, the SLF workshop, electronics team and IT team. Also thanks to Scanco Medical for the support for the Micro-CT measurements.

Thiemo Theile and Quirine Krol provided codes for the calculation of the flat-area fraction and chord length of the snow microstructure. Thanks for this and also thanks for great discussions!

I would also like to thank Henning Löwe, Maurine Montagnat and Pirmin Ebner for helpful discussions.

Thanks to Ruschle and Hew for their great help during the IGS conference in Wellington.

For always having a good mood in the office I would like to thank my office colleagues Sabine, Amy, Neige and Carolin. Thanks to Lisa and Fränzi for nice coffee and lunch breaks.

Last, but not least special thanks to my father Jürgen Wiese and my boyfriend Eike, who always supported me and cheered me up, when I was frustrated about failing experiments or a rejected paper.

Publications used for the thesis

Chapter 2
Wiese, M. and Schneebeli, M. (2017). Structural evolution of snow under controlled alternating temperature gradients with a periodicity between one and three days.
Resubmitted to Journal of Geophysical Research: Earth Surface, 2017.

Chapter 3
Wiese, M. and Schneebeli, M. (2017). Snowbreeder 5: A Micro-CT device for measuring the snow-microstructure evolution under the simultaneous influence of a temperature gradient and compaction.
Published in Journal of Glaciology, Vol. 63, No. 238, pages 355–360, doi: 10.1017/jog.2016.143.

Chapter 4
Wiese, M. and Schneebeli, M. (2017). Early-stage interaction between temperature-gradient metamorphism and settlement.
Published in Journal of Glaciology, Vol. 63, No. 240, pages 652–662, doi: 10.1017/jog.2017.31.

Chapter 5
Wiese, M., Schneebeli, M. and Or, D.. Snow metamorphism at the soil-snow interface.
In preparation for submission in The Cryosphere.

Bibliography

Adams, E. E., Jepsen, S. M., and Close, B. (2008). A bonding process between grains in mechanically disaggregated snow. *Ann. Glaciol.*, 48(1):6–12. doi: 10.3189/172756408784700770.

Adams, E. E. and Miller, D. A. (2003). Ice crystals grown from vapor onto an orientated substrate: application to snow depth-hoar development and gas inclusions in lake ice. *J. Glaciol.*, 49(164):8–12. doi: 10.3189/172756503781830953.

Akitaya, E. (1974). Studies on depth hoar. *Contributions from the Institute of Low Temperature Science*, A26:1–67.

Armstrong, R. L. (1980). An analysis of compressive strain in adjacent temperature-gradient and equi-temperature layers in a natural snow cover. *J. Glaciol.*, 26(94):283–289.

ASTM (2011). D2435/D2435M-11 Standard Test Methods for One-Dimensional Consolidation Properties of Soils Using Incremental Loading. *ASTM International, West Conshohocken, PA*. doi: 10.1520/D2435_D2435M-11.

Bader, H., Haefeli, R., Bucher, E., Neher, J., Eckel, O., Thams, C., and Niggli, P. (1939). Der Schnee und seine Metamorphose. *Beiträge zur Geologie der Schweiz, Geotechnische Serie, Hydrologie*, 3:264–266.

Barraclough, T. W., Blackford, J. R., Liebenstein, S., Sandfeld, S., Stratford, T. J., Weinländer, G., and Zaiser, M. (2016). Propagating compaction bands in confined compression of snow. *Nature Physics*. doi: 10.1038/NPHYS3966.

Berteaux, D., Gauthier, G., Domine, F., Ims, R. A., Lamoureux, S. F., Lévesque, E., and Yoccoz, N. (2016). Effects of changing permafrost and snow conditions on tundra

wildlife: critical places and times. *Arctic Science*, (1):1–26. doi: 10.1139/as-2016-0023.

Birkeland, K. W. (1998). Terminology and predominant processes associated with the formation of weak layers of near-surface faceted crystals in the mountain snowpack. *Arctic Alpine Res.*, 30(2):193–199. doi: 10.2307/1552134.

Birkeland, K. W., Johnson, R. F., and Schmidt, D. S. (1998). Near-surface faceted crystals formed by diurnal recrystallization: A case study of weak layer formation in the mountain snowpack and its contribution to snow avalanches. *Arctic Alpine Res.*, 30(2):200–204. doi: 10.2307/1552135.

Birnbaum, G., Freitag, J., Brauner, R., König-Langlo, G., Schulz, E., Kipfstuhl, S., Oerter, H., Reijmer, C. H., Schlosser, E., Faria, S. H., Ries, H., Loose, B., Herber, A., Duda, M. G., Powers, J. G., Manning, K. W., and van den Broeke, M. R. (1998). Near-surface faceted crystals formed by diurnal recrystallization: A case study of weak layer formation in the mountain snowpack and its contribution to snow avalanches. *Arctic Alpine Res.*, 30(2):200–204. doi: 10.2307/1552135.

Bokhorst, S., Pedersen, S. H., Brucker, L., Anisimov, O., Bjerke, J. W., Brown, R. D., Ehrich, D., Essery, R. L. H., Heilig, A., Ingvander, S., Johansson, C., Johansson, M., Jónsdóttir, I. S., Inga, N., Luojus, K., Macelloni, G., Mariash, H., McLennan, D., Rosqvist, G. N., Sato, A., Savela, H., Schneebeli, M., Sokolov, A., Sokratov, S. A., Terzago, S., Vikhamar-Schuler, D., Williamson, S., Qiu, Y., and Callaghan, T. V. (2016). Changing Arctic snow cover: A review of recent developments and assessment of future needs for observations, modelling, and impacts. *Ambio*, 5(45):516–537. doi: 10.1007/s13280-016-0770-0.

Brzoska, J.-B., Coléou, C., Lesaffre, B., Borel, S., Brissaud, O., Ludwig, W., Boller, E., and Baruchel, J. (1999). 3D visualization of snow samples by microtomography at low temperature. *ESRF Newsletter*, 32:22–23.

Brzoska, J.-B., Flin, F., Lesaffre, B., Coleou, C., Lamboley, P., Delesse, J.-F., Saëc, B. L., and Vignoles, G. (2001). Computation of the surface area of natural snow 3D images from X-ray tomography: two approaches. *Image Anal. Stereol.*, 20(Suppl. 1):306–312.

Bucher, E. (1956). Contribution to the theoretical foundations of avalanche defense construction. *SIPRE Transl.*, 18:1–109.

Callaghan, T. V., Johansson, M., Brown, R. D., Groisman, P. Y., Labba, N., Radionov, V., Bradley, R. S., Blangy, S., Bulygina, O. N., Christensen, T. R., Colman, J. E., Essery, R. L. H., Forbes, B. C., Forchhammer, M. C., Golubev, V. N., Honrath, R. E.,

Juday, G. P., Meshcherskaya, A. V., Phoenix, G. K., Pomeroy, J., Rautio, A., Robinson, D. A., Schmidt, N. M., Serreze, M. C., Shevchenko, V. P., Shiklomanov, A. I., Shmakin, A. B., Sköld, P., Sturm, M., Woo, M., and Wood, E. F. (2011). Multiple effects of changes in Arctic snow cover. *Ambio*, 40(1):32–45. doi: 10.1007/s13280-011-0213-x.

Calonne, N., Flin, F., Geindreau, C., Lesaffre, B., and du Roscoat, S. R. (2014). Study of a temperature gradient metamorphism of snow from 3-D images: time evolution of microstructures, physical properties and their associated anisotropy. *The Cryosphere*, 8(6):2255–2274. doi: 10.5194/tc-8-2255-2014.

Calonne, N., Flin, F., Morin, S., Lesaffre, B., Rolland du Roscoat, S., and Geindreau, C. (2011). Numerical and experimental investigations of the effective thermal conductivity of snow. *Geophys. Res. Lett.*, 38(23). doi: 10.1029/2011GL049234.

Carmagnola, C. M., Morin, S., Lafaysse, M., Domine, F., Lesaffre, B., Lejeune, Y., Picard, G., and Arnaud, L. (2014). Implementation and evaluation of prognostic representations of the optical diameter of snow in the SURFEX/ISBA-Crocus detailed snowpack model. *The Cryosphere*, 2(8):417–437. doi: 10.5194/tc-8-417-2014.

Carslaw, H. S. and Jaeger, J. C. (1959). Conduction of heat in solids. *Oxford University Press*, 64.

Chen, S. and Baker, I. (2010). Structural evolution during ice-sphere sintering. *Hydrol. Process.*, 24(14):2034–2040. doi: 10.1002/hyp.7787.

Chen, S., Baker, I., and Frost, H. J. (2013). Surface instability and mass transfer during the bonding of ice spheres. *Philos. Mag.*, 93(23):3177–3193. doi: 10.1080/14786435.2013.805274.

Colbeck, S. C. (1989a). Air movement in snow due to windpumping. *J. Glaciol.*, 35(120):209–213. doi: 10.3189/002214389793701536.

Colbeck, S. C. (1989b). Snow-crystal growth with varying surface temperatures and radiation penetration. *J. Glaciol.*, 35(119):23–29. doi: 10.3189/002214389793701536.

Coléou, C., Lesaffre, B., Brzoska, J.-B., Ludwig, W., and Boller, E. (2001). Three-dimensional snow images by X-ray microtomography. *Ann. Glaciol.*, 32(1):75–81. doi: 10.3189/172756401781819418.

Dadic, R., Schneebeli, M., Lehning, M., Hutterli, M. A., and Ohmura, A. (2008). Impact of the microstructure of snow on its temperature: A model validation with measurements from Summit, Greenland. *J. Geophys. Res.: Atmos.*, 113(D14). doi: 10.1029/2007JD009562.

De Quervain, M. R. (1958). On metamorphism and hardening of snow under constant pressure and temperature gradient. *Int. Assoc. Sci. Hydrol. Publ.*, 46:225–239.

Domine, F., Barrere, M., and Sarrazin, D. (2016). Seasonal evolution of the effective thermal conductivity of the snow and the soil in high Arctic herb tundra at Bylot Island, Canada. *The Cryosphere Discuss.* doi: 10.5194/tc-2016-107.

Domine, F., Taillandier, A.-S., Cabanes, A., Douglas, T. A., and Sturm, M. (2009). Three examples where the specific surface area of snow increased over time. *The Cryosphere*, 3(1):31–39. doi: 10.5194/tc-3-31-2009.

Domine, F., Taillandier, A.-S., Houdier, S., Parrenin, F., Simpson, W. R., and Douglas, T. A. (2007a). Interactions between snow metamorphism and climate: Physical and chemical aspects. *Physics and Chemistry of Ice, R. Soc. of Chem.*, 311:27–46. doi: 10.1029/2006JF000512.

Domine, F., Taillandier, A.-S., and Simpson, W. R. (2007b). A parameterization of the specific surface area of seasonal snow for field use and for models of snowpack evolution. *J. Geophys. Res.: Earth Surf.*, 112(F2). doi: 10.1029/2006JF000512.

Ebner, P. P., Grimm, S. A., Schneebeli, M., and Steinfeld, A. (2014). An instrumented sample holder for time-lapse microtomography measurements of snow under advective airflow. *Geosci. Instrum. Methods Data Sys.*, 3(2):179–185. doi: 10.5194/gi-3-179-2014.

Fierz, C. (1998). Field observation and modelling of weak-layer evolution. *Ann. Glaciol.*, 26:7–13. doi: 10.3198/1998AoG26-1-7-13.

Fierz, C. (2011). Temperature profile of snowpack. *Encyclopedia of Snow, Ice and Glaciers*, pages 1151–1154. doi: 10.1007/978-90-481-2642-2_569.

Fierz, C., Armstrong, R. L., Durand, Y., Etchevers, P., Greene, E., McClung, D. M., Nishimura, K., Satyawali, P. K., and Sokratov, S. (2009). The international classification for seasonal snow on the ground. *UNESCO/IHP Paris*.

Flanner, M. G. and Zender, C. S. (2006). Linking snowpack microphysics and albedo evolution. *J. Geophys. Res.: Atmos.*, 111(D12). doi: 10.1029/2005JD006834.

Flin, F. and Brzoska, J. B. (2008). The temperature-gradient metamorphism of snow: vapour diffusion model and application to tomographic images. *Ann. Glaciol.*, 49(1):17–21. doi: 10.3189/172756408787814834.

Fujita, S., Goto-Azuma, K., Hirabayashi, M., Hori, A., Iizuka, Y., Motizuki, Y., Motoyama, H., and Takahashi, K. (2016). Densification of layered firn in the ice sheet at Dome Fuji, Antarctica. *J. Glaciol.*, 231(62):103–123. doi: 10.1017/jog.2016.16.

Good, W. (1987). Thin sections, serial cuts and 3-D analysis of snow. *IAHS Publ.*, 162(Symposium at Davos 1986 – *Avalanche Formation, Movement and Effects*):35–48.

Grannas, A. M., Jones, A. E., Dibb, J., Ammann, M., Anastasio, C., Beine, H. J., Bergin, M., Bottenheim, J., Boxe, C. S., Carver, G., Chen, G., Crawford, J. H., Domine, F., Frey, M. M., Guzman, M. I., Heard, D. E., Helmig, D., Hoffmann, M. R., Honrath, R. E., Huey, L. G., Hutterli, M., Jacobi, H. W., Klan, P., Lefer, B., McConnell, J., Plane, J., Sander, R., Savarino, J., Shepson, P. B., Simpson, W. R., Sodeau, J. R., von Glasow, R., Weller, R., Wolff, E. W., and Zhu, T. (2007). An overview of snow photochemistry: evidence, mechanisms and impacts. *Atmos. Chem. Phys.*, 7(16):4329–4373. doi: 10.5194/acp-7-4329-2007.

Greene, E. M. (2007). The thermophysical and microstructural effects of an artificial ice layer in natural snow under kinetic growth metamorphism, dissertation.

Gubler, H. (1978). Determination of the mean number of bonds per snow grain and of the dependence of the tensile strength of snow on stereological parameters. *J. Glaciol.*, 20(83):329–341. doi: 10.3198/1978JoG20-83-329-341.

Hammonds, K. and Baker, I. (2016). Investigating the thermophysical properties of the ice–snow interface under a controlled temperature gradient: Part II: Analysis. *Cold Reg. Sci. Technol.*, 125:12–20. doi: 10.1016/j.coldregions.2016.01.006.

Hammonds, K., Lieb-Lappen, R., Baker, I., and Wang, X. (2015). Investigating the thermophysical properties of the ice–snow interface under a controlled temperature gradient: Part I: Experiments & Observations. *Cold Reg. Sci. Technol.*, 120:157–167. doi: 10.1016/j.coldregions.2015.09.006.

Kaempfer, T. U. and Schneebeli, M. (2007). Observation of isothermal metamorphism of new snow and interpretation as a sintering process. *J. Geophys. Res.*, 112. doi: 10.1029/2007JD009047.

Kaempfer, T. U., Schneebeli, M., and Sokratov, S. A. (2005). A microstructural approach to model heat transfer in snow. *Geophys. Res. Lett.*, 32(21). doi: 10.1029/2005GL023873.

Kerbrat, M., Pinzer, B., Huthwelker, T., Gäggeler, H. W., Ammann, M., and Schneebeli, M. (2008). Measuring the specific surface area of snow with X-ray tomography and gas adsorption: comparison and implications for surface smoothness. *Atmos. Chem. and Phys.*, 8(5):1261–1275. doi: 10.5194/acp-8-1261-2008.

Kojima, K. (1967). Densification of seasonal snow cover. *Physics of Snow and Ice: proceedings*, 1(2):929–952.

Kuipers Munneke, P., van den Broeke, M. R., Reijmar, C. H., Helsen, M. M., Boot, W., Schneebeli, M., and Steffen, K. (2009). The role of radiation penetration in the energy budget of the snowpack at Summit, Greenland. *The Cryosphere*, 3(2):155–165. doi: 10.5194/tc-3-155-2009.

Kurz, W. and Fisher, D. J. (1992). Fundamentals of solidification. *Trans. Tech. Publications*.

Löwe, H., Spiegel, J. K., and Schneebeli, M. (2011). Interfacial and structural relaxations of snow under isothermal conditions. *J. Glaciol.*, 57(203):499–510. doi: 10.3189/002214311796905569.

Massman, W. J. (1998). A review of the molecular diffusivities of H_2O, CO_2, CH_4, CO, O_3, SO_2, NH_3, N_2O, NO, and NO_2 in air, O_2 and N_2 near STP. *Atmos. Environ.*, 32(6):1111–1127. doi: 10.1016/S1352-2310(97)00391-9.

Matzl, M. and Schneebeli, M. (2010). Stereological measurement of the specific surface area of seasonal snow types: Comparison to other methods, and implications for mm-scale vertical profiling. *Cold. Reg. Sci. Technol.*, 64(1):1–8. doi: 10.1016/j.coldregions.2010.06.006.

Mills, R. D., Ratner, J. J., and Glazner, A. F. (2011). Experimental evidence for crystal coarsening and fabric development during temperature cycling. *Geology*, 39(12):1139–1142. doi: 10.1130/G32394.1.

National Snow and Ice Data Center (2017). https://nsidc.org/cryosphere/snow/climate.html.

Nemoto, M. and Nishimura, K. (2004). Numerical simulation of snow saltation and suspension in a turbulent boundary layer. *J. Geophys. Res.: Atmos.*, 109. doi: 10.1029/2004JD004657.

Pinzer, B. (2009). Dynamics of temperature gradient snow metamorphism, dissertation, DISS. ETH NO. 18456. doi: 10.3929/ethz-a-00597589.

Pinzer, B. and Schneebeli, M. (2009a). Breeding snow: an instrumented sample holder for simultaneous tomographic and thermal studies. *Meas. Sci. Technol.*, 20(9). doi: 10.1088/0957-0233/20/9/095705.

Pinzer, B. and Schneebeli, M. (2009b). Snow metamorphism under alternating temperature gradients: Morphology and recrystallization in surface snow. *Geophys. Res. Lett.*, 36(23). doi: 10.1029/2009GL039618.

Pinzer, B. R., Schneebeli, M., and Kaempfer, T. U. (2012). Vapor flux and recrystallization during dry snow metamorphism under a steady temperature gradient as observed

by timelapse micro-tomography. *The Cryosphere*, 6(5):1141–1155. doi: 10.5194/tc-6-1141-2012.

Riche, F., Montagnat, M., and Schneebeli, M. (2013). Evolution of crystal orientation in snow during temperature gradient metamorphism. *J. Glaciol.*, 59(213):47–55. doi: 10.3189/2013JoG12J116.

Riche, F. and Schneebeli, M. (2013). Thermal conductivity of snow measured by three independent methods and anisotropy considerations. *The Cryosphere*, 7(1):217–227. doi: 10.5194/tc-7-217-2013.

Scapozza, C. and Bartelt, P. (2003a). The influence of temperature on the small-strain viscous deformation mechanics of snow: a comparison with polycrystalline ice. *Ann. Glaciol.*, 37(1):90–96. doi: 10.3189/172756403781815410.

Scapozza, C. and Bartelt, P. (2003b). Triaxial tests on snow at low strain rate. Part II. Constitutive behaviour. *J. Glaciol.*, 49(164):91–101. doi: 10.3189/172756503781830890.

Schleef, S., Jaggi, M., Löwe, H., and Schneebeli, M. (2014a). An improved machine to produce nature-identical snow in the laboratory. *J. Glaciol.*, 60(219):94–102. doi: 10.3189/2014JoG13J118.

Schleef, S. and Löwe, H. (2013). X-ray microtomography analysis of isothermal densification of new snow under external mechanical stress. *J. Glaciol.*, 59(214):233–243. doi: 10.3189/2013JoG12J076.

Schleef, S., Löwe, H., and Schneebeli, M. (2014b). Hot-pressure sintering of low-density snow analyzed by X-ray microtomography and in situ microcompression. *Acta Mater.*, 71:185–194. doi: 10.1016/j.actamat.2014.03.004.

Schleef, S., Löwe, H., and Schneebeli, M. (2014c). Influence of stress, temperature and crystal morphology on isothermal densification and specific surface area decrease of new snow. *The Cryosphere*, 8(5):1825–1838. doi: 10.5194/tc-8-1825-2014.

Schneebeli, M. (2000). Three-dimensional snow: How snow really looks like. *Proceedings of International Snow Science Workshop*, pages 407–408.

Schneebeli, M. (2004). Numerical simulation of elastic stress in the microstructure of snow. *Ann. Glaciol.*, 38(1):339–342. doi: 10.3189/172756404781815284.

Schneebeli, M. and Sokratov, S. A. (2004). Tomography of temperature gradient metamorphism of snow and associated changes in heat conductivity. *Hydrol. Process.*, 18(18):3655–3665. doi: 10.1002/hyp.5800.

Schweizer, J., Jamieson, J. B., and Schneebeli, M. (2003). Snow avalanche formation. *Rev. Geophys.*, 4(41):1–14. doi: 10.1029/2002RG000123.

Shapiro, L. H., Johnson, J. B., Sturm, M., and Blaisdell, G. L. (1997). Snow mechanics: review of the state of knowledge and applications. *CRREL Report 97-3*.

Sokratov, S. A. (1998). Mass flux on the snow–soil interface. *Tohoku no yuki to seikatsu (Snow and Life in Tohoku Region)*, 13:23–26.

Sturm, M. and Benson, C. S. (1997). Vapor transport, grain growth and depth-hoar development in the subarctic snow. *J. Glaciol.*, 43(143):42–59. doi: 10.3198/1997JoG43-143-42-59.

Sturm, M. and Holmgren, J. (1998). Differences in compaction behavior of three climate classes of snow. *Ann. Glaciol.*, 26:125–130.

Sturm, M. and Johnson, J. B. (1991). Natural convection in the subarctic snow cover. *J. Geophys. Res.: Sol. Ea.*, 96:11657–11671.

Sturm, M. and Massom, R. A. (2009). *Snow and sea ice*. Oxford, Wiley-Blackwell.

Taillandier, A.-S., Domine, F., Simpson, W. R., Sturm, M., and Douglas, A. T. (2007). Rate of decrease of the specific surface area of dry snow: Isothermal and temperature gradient conditions. *J. Geophys. Res.: Earth Surf.*, 112(F3). doi: 10.1029/2006JF000514.

Theile, T., Löwe, H., Theile, T. C., and Schneebeli, M. (2011). Simulating creep of snow based on microstructure and the anisotropic deformation of ice. *Acta Mater.*, 59(18):7104–7113. doi: 10.1016/j.actamat.2011.07.065.

Van Rietbergen, B., Weinans, H., Huiskes, R., and Odgaard, A. (1995). A new method to determine trabecular bone elastic properties and loading using micromechanical finite-element models. *J. Biomech.*, 28(1):69–81. doi: 10.1016/0021-9290(95)80008-5.

Vionnet, V., Brun, E., Morin, S., Boone, A., Faroux, S., Le Moigne, P., Martin, E., and Willemet, J. M. (2012). The detailed snowpack scheme Crocus and its implementation in SURFEX v7. 2. *Geosci. Model Dev.*, 5:773–791. doi: 10.5194/gmd-5-773-2012.

Wang, X. and Baker, I. (2014). Evolution of the specific surface area of snow during high-temperature gradient metamorphism. *J. Geophys. Res.: Atmos.*, 119(24). doi: 10.1002/2014JD022131.

Wang, X. and Baker, I. (2016). Comparison of the Effects of Unidirectional and Sign-Alternating Temperature Gradients on the Sintering of Ice Spheres. *Hydrol. Process.* doi: 10.1002/hyp.11067.

Weller, G. and Schwerdtfeger, P. (1977). Thermal properties and heat transfer processes of low-temperature snow. *Antarctic Research Series, Meteorological Studies at Plateau Station, Antarctica*, 25. doi: 10.1002/9781118664872.ch3.

Wever, N., Schmid, L., Heilig, A., Eisen, O., Fierz, C., and Lehning, M. (2015). Verification of the multi-layer SNOWPACK model with different water transport schemes. *The Cryosphere Discussions*, 9(2):2655–2707. doi: 10.5194/tcd-9-2655-2015.

Wiese, M. and Schneebeli, M. (2017a). Early-stage interaction between temperature-gradient metamorphism and settlement. *J. Glaciol.*, 63(240):652–662. doi: 10.1017/jog.2017.31.

Wiese, M. and Schneebeli, M. (2017b). Snowbreeder 5: A Micro-CT device for measuring the snow-microstructure evolution under the simultaneous influence of a temperature gradient and compaction. *J. Glaciol.*, 63(238):355–360. doi: 10.1017/jog.2016.143.

Wiese, M. and Schneebeli, M. (2017c). Structural evolution of snow under controlled alternating temperature gradients with a periodicity between one and three days. *J. Geophys. Res.: Earth Surf.* in revision.

World Meteorological Organization (WMO) (2008). Guide to meteorological instruments and methods of observation, 7th edn. (WMO-No 8) World Meteorological Organization, Geneva.

Yosida, Z. (1955). Physical Studies on Deposited Snow. I. Thermal properties. *Contrib. Inst. Low Temp. Sci.*, 7:19–47. doi: 10.1002/2014JD022131.

List of publications

Wiese, M., Griewank, P. and Notz, D. (2015). On the thermodynamics of melting sea ice versus melting freshwater ice. *Ann. Glaciol.*, 56(69):191–199. doi: 10.3189/2015AoG69A874.

Wiese, M. and Schneebeli, M. (2017). Snowbreeder 5: A Micro-CT device for measuring the snow-microstructure evolution under the simultaneous influence of a temperature gradient and compaction. *J. Glaciol.*, 63(238):355–360. doi: 10.1017/jog.2016.143.

Wiese, M. and Schneebeli, M. (2017). Early-stage interaction between temperature-gradient metamorphism and settlement. *J. Glaciol.*, 63(240):652–662. doi: 10.1017/jog.2017.31.